Miniature High-frequency Ultrasound Transducers for Magnetic Soft Continuum Robot Applications

Yifei Wang

Submitted in fulfilment of the requirements for the

Degree of Doctor of Philosophy

Centre for Medical and Industrial Ultrasonics

James Watt School of Engineering

University of Glasgow

August 2026

Declaration of authorship

I hereby declare that this thesis entitled, “Miniature high-frequency ultrasound transducers for Magnetic Soft Continuum Robot Applications”, submitted to University of Glasgow for the degree of Doctor of Philosophy represents my own original research. It has been composed by me, and it has not been previously submitted for any other degree in this university or any other university.

I declare that artificial intelligence was utilised solely for the purpose of refining the language in this thesis. It was not employed for the origination of any research content, or data analysis, all of which are my original work.

Signed: Yifei Wang

Date: 15/05/2026

Abstract

Intracorporeal high-frequency ultrasound (US) is a potentially important modality in modern medical diagnostics, offering superior resolution for internal anatomical structures. However, conventional delivery platforms, such as needles, catheters and capsules, are often constrained by their mechanical rigidity, which limits access to complex or tortuous anatomical regions. To address these limitations, magnetic soft continuum robots (MSCRs), composed of magnetic nanoparticles embedded within a silicone matrix, are emerging as a potential solution. These soft, compliant mechanisms can be remotely manipulated and actively steered via external magnetic fields, enabling non-invasive actuation for minimally invasive medical intervention.

This thesis establishes a proof-of-concept for this novel imaging platform, detailing the development and integration of miniature high-frequency US transducers with MSCR platforms. A 15 MHz single-element transducer was fabricated utilising PIN-PMN-PT single crystals and a 1-3 composite structure. The research investigates the integration methodology, specifically quantifying the mechanical influence of the transducer payload on the MSCR's deflection capabilities. The functional performance of the integrated system was validated through a progressive series of experiments: preliminary lateral proximity sensing via A-scan, axial imaging via sweep scanning in silicone phantoms, and the development of a dual-element configuration capable of lateral sensing and axial imaging. The clinical feasibility of the platform was demonstrated through rotational scanning in *ex vivo* porcine tissue and, finally, explored via *in vivo* trials in a porcine model.

Concurrently, to further enhance acoustic performance, the thesis explores the application of novel piezoelectric materials. With the emergence of rare-earth doping as a strategy to optimise electromechanical properties, the efficacy of Samarium-doped PIN-PMN-PT (Sm:PIN-PMN-PT) single crystals is explored. The influence of this advanced material was evaluated by fabricating and characterising both 1-3 composite single-element transducers and 1D linear arrays. Comprehensive testing included impedance magnitude and phase analysis, pulse-echo response and sensitivity and resolution measurements. This demonstrated that Sm:PIN-PMN-PT single crystals possess superior characteristics, identifying them as an excellent candidate for MSCR integration and the next generation of medical US imaging devices.

Acknowledgements

First and foremost, I would like to express my deepest gratitude to my supervisors, Prof. Sandy Cochran and Dr. Kwok-Ho Lam. Thank you for your support and guidance during my PhD. I am grateful for the countless discussions, meetings, and talks where I gained valuable knowledge and advice. Thank you for your patience, your enthusiasm for my projects, and the inspiration you have given me throughout my work.

I would also like to extend my appreciation to Dr. Jiaming Zhang, who provided valuable advice and support remotely during my PhD and my training at The Hong Kong Polytechnic University. I could not have finished my projects without his help.

I thank Mr. Alistair Bacchetti for all the collaboration and exploration we have done together at the University of Leeds. I am happy to have a collaborator and friend like you during my PhD. Meanwhile, thanks to Dr. James Chandler, Prof. Pietro Valdastri, and the members of the STORM Lab at University of Leeds for their selfless sharing of expertise and assistance.

I would like to express my gratitude to all my friends, including but not limited to colleagues at Centre for Medical and Industrial Ultrasonics and to all the friends who went hiking and bouldering with me. Thank you for the fun we had together and for companionship throughout my years in Glasgow.

Last but not least, I thank my parents for their constant, sincere love and support. I always feel a sense of warmth whenever I think of them. Whatever I have achieved and whatever I may achieve in the future belong to them.

Table of contents

List of figures

List of tables

List of terms

Abbreviations

1-3 composite	1-3 connectivity piezoelectric ceramic - polymer composite
2D	Two-dimensional
3D	Three-dimensional
AR	Aspect ratio
ASICs	Application-specific integrated circuits
Au	Gold
B-Mode	Brightness mode
BW	Bandwidth
CMUT	Capacitive micromachined ultrasonic transducers
CT	Computed tomography
DAQ	Data acquisition
DI	Deionised water
DoF	Degrees of freedom
DRIE	Deep reactive-ion etching
DWI	Diffusion-weighted imaging
EPM	External permanent magnet
EUS	Endoscopic ultrasound
FBG	Fibre bragg grating
FEA	Finite element analysis
FFT	Fast Fourier Transform
FID	Free induction decay
fPCB	Flexible printed circuit board
ICE	Intracardiac echocardiography
IL	Insertion loss

IPA	Isopropyl alcohol
IVUS	Intravascular ultrasound
LS	Linear straight
LSA	Linear straight with aneurysm
MEMS	Microelectromechanical systems
M-Mode	Motion mode
MPB	Morphotropic phase boundary
MRI	Magnetic resonance imaging
MSCRs	Magnetic soft continuum robots
NdFeB	Neodymium-iron-boron
OCT	Optical coherence tomography
PAI	Photoacoustic imaging
PAMAP	photoacoustic maximum amplitude projection
PET	Positron emission tomography
PMUTs	Piezoelectric micromachined ultrasonic transducers
PTFE	Polytetrafluoroethylene
PVC	Polyvinyl chloride
PVDF	Polyvinylidene difluoride
P(VDF-TrFE)	Polyvinylidene difluoride copolymer
PZT	Lead zirconate titanate
R2	Coefficient of determination
RF	Radiofrequency
RMS	Root mean square
rpm	Revolutions per minute
SEM	Scanning electron microscopy
Sm	Samarium
SWE	Shear wave elastography

Ti	Titanium
ToF	Time-of-flight
US	Ultrasound
USMIP	US maximum intensity projection
VF	Volume fraction

Symbols

A	Area of the element
B	Magnetic field
c	Sound velocity in water
c_l	Longitudinal acoustic velocity
C_p-D	Parallel capacitance and dissipation factor
d	Distance between transducers
d_{33}	Piezoelectric constant
dB	Decibels
D	Distance between two transducers
ε_0	Vacuum permittivity
$\varepsilon_{33}{}^{T}$	Clamped relative dielectric constant
f_a	Anti-resonance frequency
f_c	Centre frequency
f_r	Resonance frequency
F	Focal length
k_t	Electromechanical coupling coefficient
k_{eff}	Effective electromechanical coupling coefficient
λ	Wavelength of the ultrasound
L	Inductance

m	Magnetic moment
N	Near-field distance
R_{axial}	Axial resolution
$R_{lateral}$	Lateral resolution
ρ	Density
t	Thickness of the material
t_1	Start time with sample in ToF
t_1	Start time without sample in ToF
τ	Aligning torque
V	Voltage
w	Element width
Z-θ	Impedance-theta
Z	Acoustic impedance

Chapter 1 Introduction

1.1 Objectives

The primary aim of this thesis is to establish a proof-of-concept for integrating miniature high-frequency US transducers into MSCRs. This integration seeks to create a novel carrier platform capable of performing both medical diagnostics using US and potential therapeutic interventions by delivering drugs in the future. Furthermore, the thesis describes an investigation into the performance capabilities of US transducers based on novel piezoelectric materials. The specific objectives of the research are as follows:

- Fabrication process and characterisation of high-frequency transducers specifically for integration into MSCRs: To establish the detailed fabrication protocols, including the generation of process diagrams, for both high-frequency single-element and US array transducers, and to explain their subsequent development and characterisation.
- Co-design, integration, and *in vivo* validation of the US-MSCR system: To execute the co-design and micro-fabrication of a single-element US transducer integrated within the MSCR. This includes the physical characterisation of the integrated system, followed by performance validation in *ex vivo* tissue models and *in vivo* preclinical trials.
- Investigation of Sm:PIN-PMN-PT single crystals in a single-element transducer configuration: To fabricate single-element transducers utilising Sm:PIN-PMN-PT single crystals and to demonstrate their performance, thereby exploring the potential of this material to enhance sensitivity and bandwidth in miniature devices.
- Feasibility study of Sm:PIN-PMN-PT single crystals in array configuration: To assess the feasibility and performance characteristics of Sm:PIN-PMN-PT single crystals when engineered into an US array transducer, focusing on the practical conversion of material properties into high performance imaging capabilities.

1.2 Thesis structure

Chapter 2 provides the theoretical foundation for the research presented in this thesis. The literature review is organised into three primary sections. The first section surveys the landscape of modern medical imaging, briefly discussing modalities such as magnetic resonance imaging (MRI), computed tomography (CT), and positron emission tomography (PET). It then offers a detailed examination of US imaging, covering its common operational modes and emerging multimodality imaging techniques that combine US with other diagnostic tools.

The second section starts with categories of US transducers and subsequently focuses on the core component of the imaging system: the piezoelectric US transducer. It details the fundamental composition of these devices, including the role of active materials, backing layers, and matching layers. Particular attention is given to the introduction of piezoelectric materials and the specific 1-3 connectivity piezoelectric ceramic - polymer composite (1-3 composite) structure utilised in this project.

The final section reviews existing delivery platforms for miniature high-frequency US transducers. It traces the methods of intracorporeal carriers from traditional catheters, endoscopes, and needles to novel MSCRs that form the basis of this study. The chapter concludes by articulating the significance of this research, highlighting how integrating advanced transducers with soft robotics addresses current clinical limitations.

Chapter 3 establishes the technical foundation for the research by detailing the methodology used to develop both single-element and array transducers. The discussion begins with the overall development process, encompassing simulations and the characterisation of the acoustic layers. The fabrication workflow for the single-element transducer is described in detail, including the specific equipment, techniques, and materials employed. Subsequently, the chapter addresses the development of the 1D linear array. It outlines the critical design considerations and analyses specific technical issues encountered during the fabrication process.

To validate the performance of the fabricated devices, the final section presents the characterisation protocols. These include electrical impedance spectroscopy, pulse-echo response, sensitivity, and spatial resolution measurement. For the array

transducers, additional performance metrics such as signal-to-noise ratio (SNR) and inter-element crosstalk are evaluated. Collectively, the methodologies and data presented in this chapter provide the essential technical basis for the applications discussed in subsequent chapters.

Chapter 4 presents the development and validation of an integrated imaging platform combining high-frequency US with MSCRs. The research begins with the exploration of the MSCR as a carrier for US transducers, detailing the design, fabrication, and optimisation of the configuration. To address specific clinical requirements, a second version of the device was developed, incorporating enhanced functionality and improved structural features.

The experimental validation is divided into two phases. In the first phase, the study focuses on the mechanical characterisation of deflection capabilities, along with functional tests for proximity measurement and axial imaging. In the second phase, the investigation expands to rotational performance and imaging resolution during dynamic motion. The chapter introduces the assessment of the platform in realistic biological environments, including *ex vivo* tissue imaging and *in vivo* trials in a porcine model. The findings from these experiments are analysed to identify the distinct advantages of this hybrid system and the technical areas requiring further improvement.

Chapter 5 presents single-element transducer and array fabrication, characterisations and incorporating Sm:PIN-PMN-PT single crystal through two distinct research phases. The first phase investigates the application of the novel piezoelectric material for high-frequency US single-element transducers. The section begins with a brief review of conventional single-element materials and recent advances in rare-earth doping strategies aimed at enhancing material properties. This literature survey identifies a significant research gap: despite the theoretical promise of Sm:PIN-PMN-PT, there are currently no reports of its successful implementation in a functional US device.

To address this, a 15 MHz single-element transducer with a 1-3 composite structure was fabricated. The first phase details the characterisation of the device, covering both electrical parameters and mechanically scanned imaging performance. This rigorous assessment benchmarks the performance of the Sm:PIN-PMN-PT transducer against devices fabricated from two conventional PIN-PMN-PT and PMN-PT single crystals.

The results demonstrate the superior performance of the Sm-doped crystal, providing a basis for other researchers to utilise this material in future US imaging applications and for MSCR devices.

The second phase builds upon the material characterisation presented in phase one. It explores the application of Sm:PIN-PMN-PT single crystal in the development of a high-frequency 1D linear array transducer. The study details the complete engineering process, including the specific design and fabrication techniques required to construct a 15 MHz, 64-element array. The performance of the device was evaluated according to the characterisation protocols established in Chapter 3 and subsequently validated through imaging tests on *ex vivo* tissue specimens.

The results indicate that the fabricated array exhibits good acoustic performance, thereby identifying Sm:PIN-PMN-PT single crystal as a viable material candidate for future US array design. Furthermore, the fabrication of this standard-size array serves as a critical preliminary step towards integration with MSCR. By first validating the manufacturing process and signal quality at scale, this work lays the foundation for subsequent designs, in which the array area will be optimised and miniaturised to meet the dimensional constraints of the MSCR platform.

Chapter 6 presents the conclusions for this work and discusses further steps in the development of this project.

1.3 Contribution to knowledge

This thesis makes the following original contributions to the field of US transducer fabrication and medical robotics:

- A refined fabrication protocol was developed for 15 MHz PIN-PMN-PT single crystal 1-3 composite transducers suitable for integration with MSCRs. A novel technique utilising an epoxy frame was introduced to stabilise the piezoelectric element during the dice-and-fill process. This method significantly mitigated structural damage during the fabrication of 1-3 composite structures. It enabled the reliable processing of single crystals with a fine pitch of approximately 50 μm, thereby improving manufacturing yield and reducing processing time. This fabrication method is verified and published in [1].

- This research presents an exploration of Sm:PIN-PMN-PT single crystals for transducer applications. Both high-frequency single-element transducers and 1D linear array transducers were fabricated. Through comparative analysis with standard single crystal devices of identical dimensions and frequency, this study demonstrated the superior performance of the Sm-doped material, establishing it as a high-performance candidate for future biomedical imaging.

- This work established a proof of concept for using an MSCR as a steerable carrier for intracorporeal US. The core advancements include the design and integration of various transducer configurations, as well as a detailed analysis of the payload's impact on robotic mechanics. The system was validated through axial imaging tests and the characterisation of rotational scanning capabilities. Finally, the clinical viability of the platform was empirically demonstrated through *ex vivo* tissue experiments and *in vivo* trials in a porcine model. The findings from this investigation have been compiled into a manuscript currently in preparation for journal publication. A. Bacchetti[#], Y. Wang[#], N. Murasovs, V. Francescon, R. Mathew, K.H. Lam, R.A. Harris, P. Valdastri, S. Cochran and J.H. Chandler are preparing this work under the title '*Embedded miniature ultrasound transducers on magnetic soft continuum robots*' for submission to *Science Advances* journal.

1.4 Publications

Journals related to the work in this thesis

[1] **Y. Wang**, K.H. Lam, and S. Cochran, 'High-sensitivity Sm:PIN-PMN-PT ultrasound transducer for biomedical imaging applications', Appl. Phys. Lett, doi: 10.1063/5.0284003.

[2] A. Bacchetti[#], **Y. Wang**[#], N. Murasovs, V. Francescon, R. Mathew, K.H. Lam, R.A. Harris, P. Valdastri, S. Cochran and J.H. Chandler 'Embedded miniature ultrasound transducers on magnetic soft continuum robots', in preparation

[#] The two authors contributed equally to this work.

Journals related to the work not in this thesis

[3] X. Li, **Y. Wang**, Y. Zeng, D. Shi, Z. Huang, and K.H. Lam, 'Optimisation of adhesive-free high-frequency miniature class IV transducers incorporating single-element piezoelectric plates', *Sens. Actuators Phys.*, doi: 10.1016/j.sna.2026.117489.

[4] J. Zhang, R. Lin, X. Wang, G. Bao, F. Yang, S. Hou, G. Li, **Y. Wang**, X. Gong, J. Dai and K.H. Lam, 'Broadband transparent ultrasound transducer design via matching-free composite approach', *Mater. Design*, doi: 10.1016/j.matdes.2025.115369.

[5] **Y. Wang**, E. Germano, Z. Wang, A. Alexandrou, A. Feeney, K.H. Lam, S. Cochran, 'High-performance 15 MHz ultrasound imaging: synergising novel textured piezoceramics with coded excitation for deep-tissue imaging applications', in preparation.

Conference presentations related to the work in this thesis

[1] **Y. Wang**, M. D. Lecce, J.H. Chandler, P. Valdastri, K.H. Lam, S. Cochran, 'Miniature intracorporeal ultrasound transducers as a payload for soft tentacle robotics', poster presented at 2023 IEEE International Ultrasonics Symposium, Montreal, Canada, September 2023.

[2] **Y. Wang**, A. Bacchetti, J.H. Cahndler, P. Valdastri, K.H. Lam and S. Cochran, 'Customised miniature diagnostic ultrasound transducers for soft tentacle robotics', poster presented at 2024 Ultrasonics, Ferroelectrics, and Frequency Control Joint Symposium, Taipei, China, September 2024.

[3] **Y. Wang,** K.H. Lam and S. Cochran, 'High-frequency ultrasound transducer fabrication incorporating Sm-PIN-PMN-PT single crystal / epoxy composite', poster presented at 2025 International Workshop on Acoustic Transduction Materials & Devices (IWATMD), PA, United States, May 2025.

[4] **Y. Wang,** K.H. Lam and S. Cochran, 'Sm-doped PIN-PMN-PT piezocomposite fabrication for high-frequency ultrasound transducers', poster presented at Ferroelectrics UK and Ireland 2025 conference, Bath, UK, May 2025.

Conference presentation related to the work not in this thesis

[5] **Y.Wang**, A.Alexandrou, R.L. O'Leary, K.H. Lam and S.Cochran, '15 MHz High-Frequency Medical Ultrasound Array made with Textured Piezoceramics', poster presented at Anglo-French Physical Acoustics Conference (*AFPAC 2025*), Bristol, UK, January 2026.

Chapter 2 Research background

The primary engineering development of this project involves the design and characterisation of intracorporeal high-frequency US transducers integrated onto a novel robotic platform. This technical focus encompasses the systematic implementation of miniaturised US hardware specifically for biomedical applications. Accordingly, this chapter begins by reviewing modern medical imaging modalities within clinical practice. The subsequent sections present the structure of US transducers and a classification of piezoelectric materials. Finally, the chapter evaluates conventional platforms for high-frequency miniature US transducers, identifying their inherent mechanical limitations. This analysis highlights a critical need for innovation for certain applications, thereby establishing the specific objectives of this research.

2.2 Medical imaging modalities

Modern medicine is closely linked to advances in medical imaging. This field has changed diagnostics from an era of exploratory surgery to one of non-invasive visualisation. Since the discovery of X-rays in 1895 [2], the field has expanded from simple radiographs to include complex 3D functional and molecular imaging techniques. Today, medical imaging does not just map anatomy, it has become a quantitative science capable of measuring physiological processes, metabolic activity, and tissue properties down to the cellular level and below.

Clinical evaluations of internal human structures rely on diverse imaging modalities governed by distinct physical principles. Modality selection depends on the clinical questions and requires balancing factors such as image resolution, acquisition speed, tissue contrast, and patient safety. This section provides a review of primary anatomical imaging modalities including MRI, CT and US while concurrently including PET as a functional imaging modality, analysing their respective underlying physical mechanisms, clinical applications and inherent operational limitations.

2.2.1 Magnetic resonance imaging

MRI uses the natural magnetic properties of hydrogen protons, which are abundant in water and fat within the human body. Figure 2.1 illustrates the 4 main stages of the MRI process.

Proton alignment occurs under a strong static magnetic field B_0 to establish a net longitudinal magnetisation (Figure 2.1A). A radiofrequency (RF) excitation pulse at a specific Larmor frequency subsequently transitions the protons into a high-energy state (Figure 2.1B). This excited state persists for the duration of the pulse until the RF source is removed (Figure 2.1C). The protons then return to their aligned resting state and emit detectable free induction decay (FID) signals through the relaxation process (Figure 2.1D). The resulting image contrast directly reflects the specific relaxation parameters of the protons within diverse anatomical substrates [3], [4].

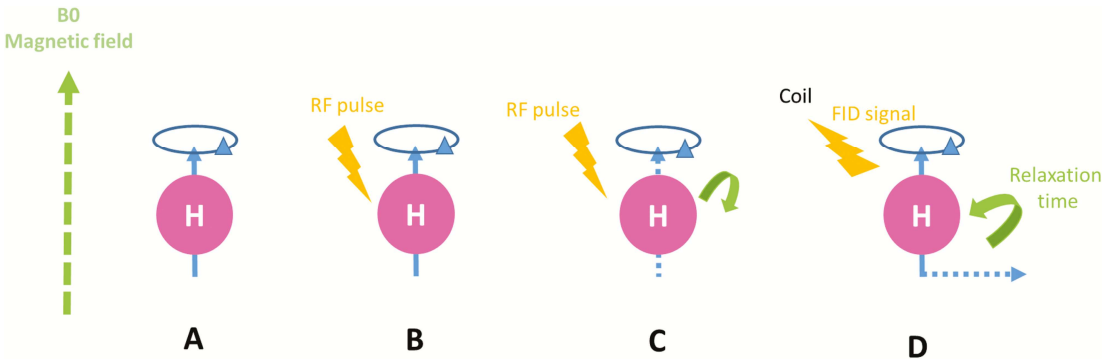

Figure 2.1 Schematic of functional stages in MRI principles [5]. (Modified with permission)

MRI provides diagnostic capabilities beyond basic structural visualisation through the implementation of advanced functional sequences. Diffusion-weighted imaging (DWI) measures the random movement of water molecules to assess tissue health and remains the primary method for detecting acute stroke within hours of the event [6]. Figure 2.2 illustrates the diagnostic precision and brain change of DWI following an acute ischemic stroke. Furthermore, functional MRI detects blood flow changes linked to neural activity to allow non-invasive mapping of brain functions [7], [8].

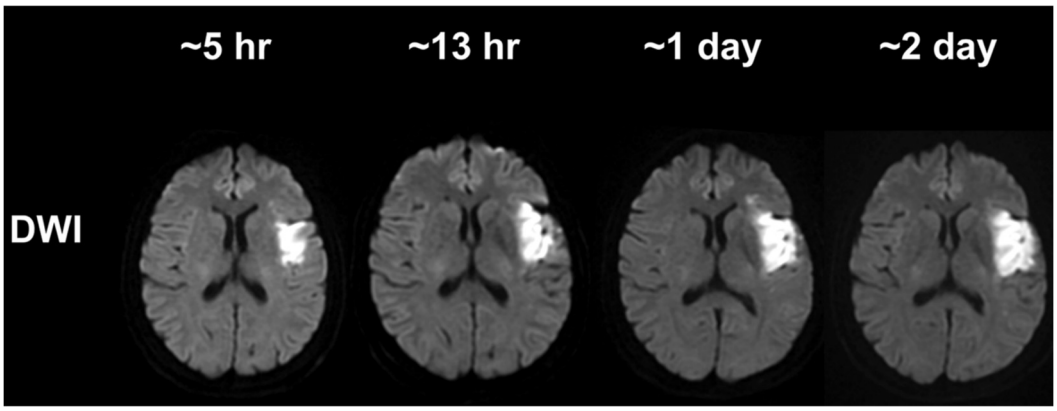

Figure 2.2 Brain changes after a stroke imaged with MRI [9]. (Modified with permission)

Despite its advantages, MRI has significant drawbacks. The scanning process is slower than other technologies. Furthermore, the strong magnetic field is dangerous for patients with metal implants, and the machine is too large and expensive to be truly portable [3].

2.2.2 Computed tomography

CT imaging works by measuring the attenuation of X-rays as they pass through tissues of varying density. Modern scanners rotate around the patient to collect data from many angles. This data is reconstructed to create cross-sectional images where brightness corresponds to tissue density [10]. Figure 2.3 illustrates the prevalent third-generation architecture. This design is often referred to as a rotate-rotate geometry because both the X-ray tube and the detector array rotate simultaneously around the patient.

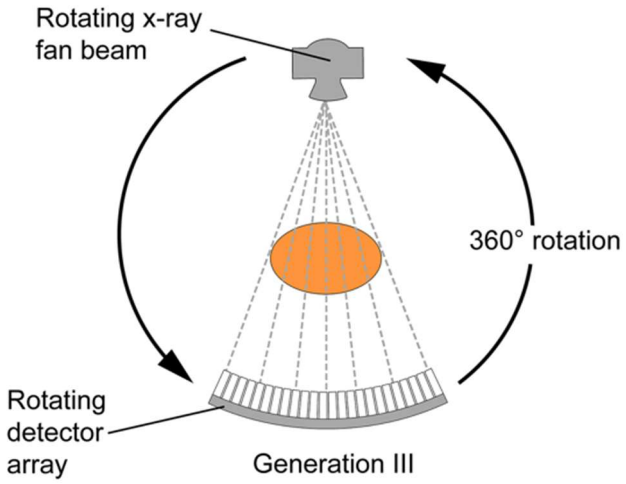

Figure 2.3 Illustration of the third-generation CT [11]. (Modified with permission)

CT is an excellent modality for imaging the brain [12] and the lungs. For neurological applications, Figure 2.4 shows a typical brain CT scan of a patient undergoing treatment, with intracranial pressure being measured using a ventricular catheter. As shown in the image, the catheter appears as a bright feature (arrowed) and is highly visible, which provides excellent visualisation for the precise guidance of medical procedures.

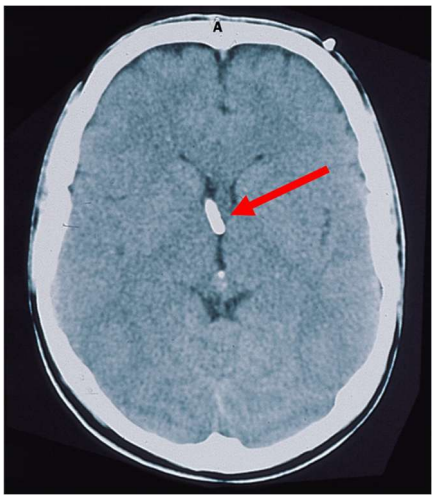

Figure 2.4 CT image of a brain from the top [12]. (Reuse with permission)

In respiratory care, CT is routinely used to screen for lung cancer because it can detect small lung nodules in early stage [13], [14]. Furthermore, CT serves as the standard imaging tool for the assessment of trauma patients [15], [16]. It offers significant diagnostic advantages over structured radiography when evaluating acute trauma-related injuries [17].

CT systems possess exceptional spatial resolution. This established modality remains faster and more cost-effective than conventional MRI systems. The primary limitation involves the requisite use of ionising radiation bearing an inherent oncogenic risk. Furthermore, this modality exhibits soft tissue contrast resolution inferior to that of MRI [18].

2.2.3 Positron emission tomography

The imaging modalities introduce above visualise anatomical structures. These morphological techniques frequently fail to detect early molecular variations preceding physical tissue alterations. Nuclear medicine establishes a fundamentally distinct diagnostic paradigm by tracking the chemical activity of living tissues. PET

represents a critical clinical modality within this specialised field [19]. PET visualises metabolic activity through a precise mechanism involving two primary stages. In stage one (Figure 2.5A), a positron from an administered radioactive tracer travels a short distance in the tissue before annihilating with an electron. This specific collision emits two 511 keV photons travelling in opposite directions. In stage two (Figure 2.5B), an external ring of radio detectors comprising scintillation crystals and photomultiplier tubes captures these photons. The imaging system reconstructs the final image by exclusively processing photons detected simultaneously in coincidence.

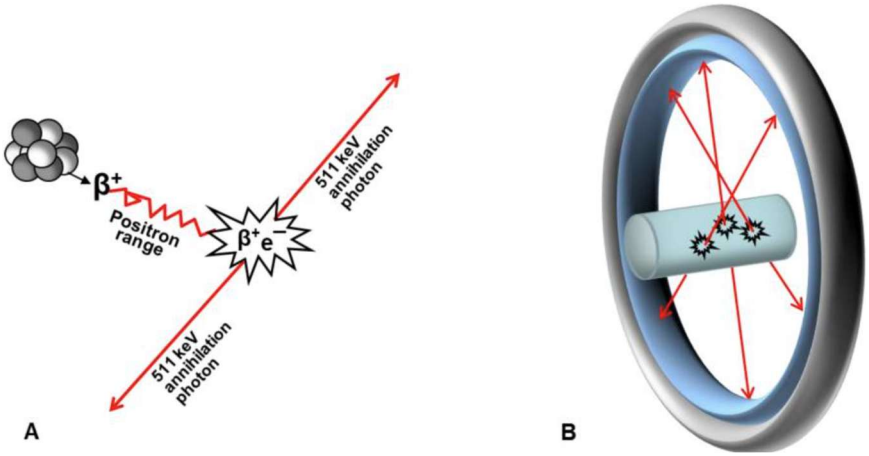

Figure 2.5 Schematic of the PET principle. (A) A positron annihilates with an electron to emit two oppositely directed 511 keV photons. (B) A detector ring registers these coincident photons for image reconstruction [20]. (Reuse with permission)

As malignant cells metabolise sugar much faster than healthy tissues, they accumulate more tracer and present prominently as bright hot spots [21]. This distinct metabolic tracking dictates the predominant use of PET in clinical oncology. The unique functional capability makes the molecular modality clinically indispensable for accurate cancer staging despite lower overall utilisation rates [22].

The spatial resolution of PET is inherently lower than that of CT or MRI, which limits its ability to provide precise anatomical localisation. Therefore, PET is almost universally integrated with CT to provide the necessary anatomical context [23], [24]. Figure 2.6 demonstrates bone and supraclavicular lymph node metastases detected by PET/CT in a patient treated for breast cancer. The standalone CT image (top left) clearly delineates the anatomical bone structure. In contrast, the standalone PET image (top right) lacks detailed anatomical boundaries but effectively highlights regions of

metastatic lesions. The fused PET/CT image (bottom left) integrates both modalities to precisely localise these highly active metastases within the anatomical framework.

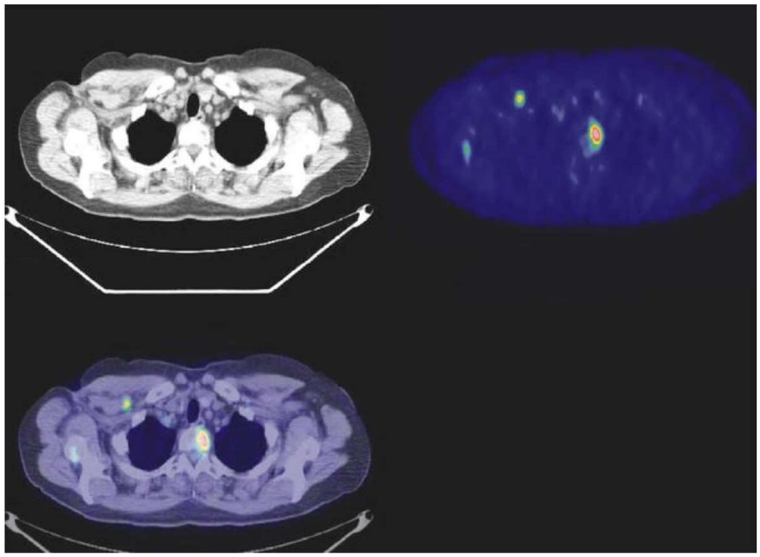

Figure 2.6 Patient treated for breast cancer. Bone and supraclavicular lymph node metastases were detected by PET/CT: CT (top left), PET (top right) and fused PET/CT (bottom left) [23]. (Reuse with permission)

2.2.4 Ultrasound

US comprises mechanical waves exceeding the 20 kHz human hearing threshold to achieve biological tissue penetration. This modality evolved from the repurposing of non-destructive testing and sonar instrumentation approximately seven decades ago [25], [26].

US imaging relies on the pulse-echo principle illustrated in Figure 2.7. A transducer transmits an acoustic pulse into the target. As this wave encounters interfaces between the medium and the target with varying acoustic impedance, a fraction of the energy is reflected back to the transducer. The imaging system subsequently processes these returning echoes to construct the final diagnostic image. This non-ionising mechanism provides unique advantages regarding safety, real-time capability, cost and portability in modern healthcare [27], [28], [29].

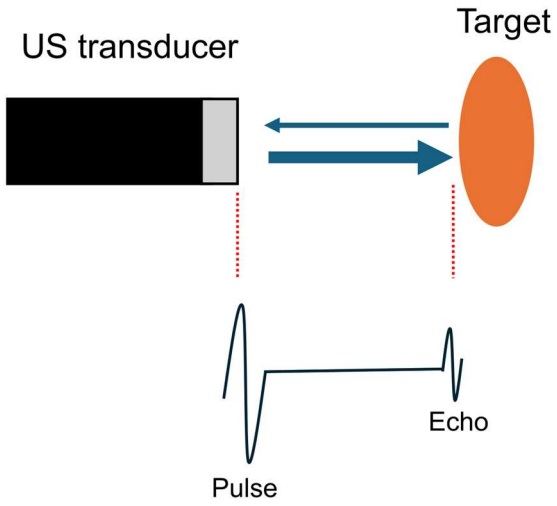

Figure 2.7 Schematic of pulse-echo principle.

Clinical imaging applications typically use frequency ranges between 2 MHz and 20 MHz. High-resolution imaging requires acoustic frequencies exceeding 20 MHz to ensure precise anatomical visualisation [30]. However, the mechanical nature of US imposes critical limitations. High-frequency acoustic waves suffer from attenuation, which restricts the imaging depth in biological tissues. This severe energy loss dictates a physical trade-off between spatial resolution and acoustic penetration [3], [31].

US systems visualise different body structures using specific acoustic principles. Combining these US tools with MSCRs offers potential to enhance diagnostic imaging deep inside the human body. The following sections explain the basic working principles of US modalities, detailing their specific imaging capabilities.

B-Mode (Brightness Mode)

B-mode represents the standard format for viewing anatomical structures. The imaging system converts the amplitude of a returning echo into a specific pixel on a greyscale display where the brightness corresponds directly to the reflection strength. The resulting two-dimensional (2D) images enable the direct visualisation of internal anatomy to provide diagnostic and navigational information. The clinical application of three-dimensional (3D) US has also expanded significantly in recent years [32]. This advanced technique involves acquiring serial 2D slices that undergo computational reconstruction to form a complete volumetric image. Figure 2.8 displays a standard 2D US image of a baby on the left and the corresponding rendered 3D reconstruction on the right. Such volumetric visualisation displays the entire target within a single comprehensive view to significantly enhance the understanding of

complex spatial relationships [33]. In this thesis the US transducers integrated into the MSCR utilise this standard imaging mode to achieve sweep scan and rotational scan capabilities.

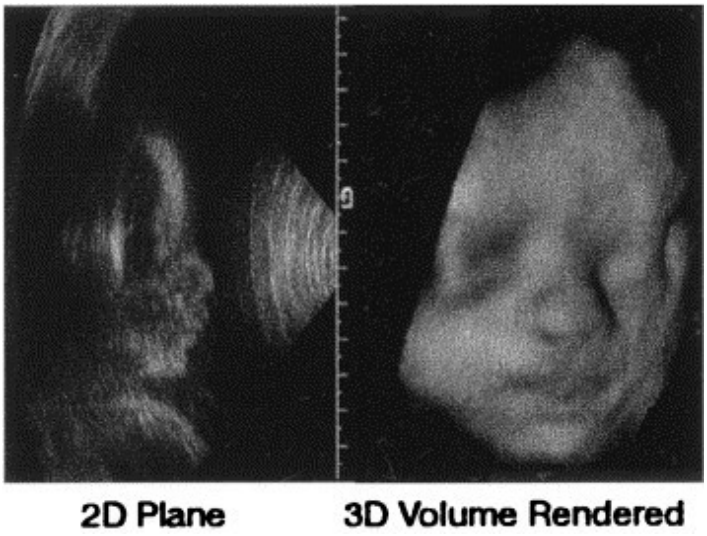

Figure 2.8 2D US image slice (left) and 3D volumetric imaging (right) of a baby [33]. (Reuse with permission)

M-Mode (Motion Mode)

Rather than generating a two-dimensional image, M-mode (motion mode) records ultrasound echoes along a single scan line over time. This modality displays signals from anatomical structures intersected by the beam, visualising their motion either towards or away from the transducer face. By plotting this movement as a function of time, M-mode provides exceptional temporal resolution, enabling the precise measurement of rapidly moving structures [34], [35]. As illustrated in Figure 2.9, this technique is particularly effective for assessing diaphragmatic kinetics. During inspiration, the diaphragm moves caudally towards the probe (A), resulting in an upward deflection on the M-mode trace. Conversely, during expiration, the trace moves downwards as the diaphragm recedes from the transducer (B).

Potentially, this mode can enable the precise tracking of rapid structural displacements within narrow physiological environments, providing crucial dynamic data during MSCR navigation.

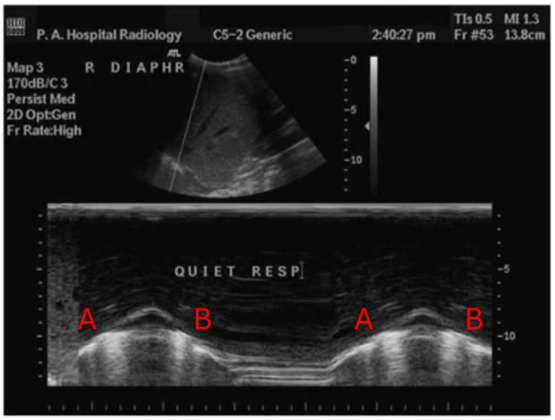

Figure 2.9 M-mode trace of diaphragmatic excursion [35]. (Modified with permission)

Colour Doppler

Doppler US utilises the Doppler effect to quantify blood flow. As acoustic waves interact with moving erythrocytes, the frequency of the returned echo shifts relative to the source. In colour Doppler mode, these frequency shifts are superposed as colour maps onto the anatomical B-mode image. By convention, red indicates flow towards the transducer while blue indicates flow away from the transducer, providing a rapid assessment of vascular patency [36], [37].

To differentiate accurately between venous and arterial structures, clinicians can apply Doppler flow measurements to derive specific blood flow profiles. As illustrated in Figure 2.10, a transverse view of the right internal jugular vein and carotid artery demonstrates how colour coding and spectral profiles enable precise vessel identification. Specifically, the measurements allow for the derivation of characteristic venous and arterial blood flow profiles required for definitive physiological assessment.

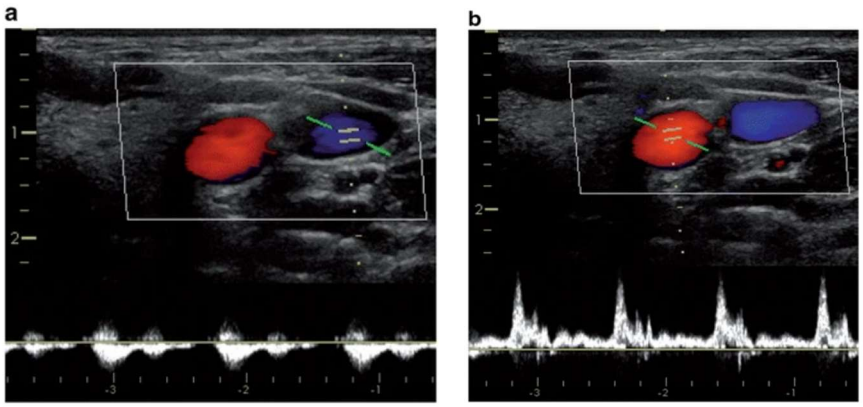

Figure 2.10 Colour Doppler imaging and flow measurements of the (a) veins and (b) arteries [36]. (Modified with permission)

Previous investigations by Qiu et al. successfully integrated a 20 MHz forward looking US transducer into a conventional catheter to execute precise pulse wave Doppler flow measurements. This established engineering baseline suggests that MSCRs offer potential serving as novel flexible and controllable carriers to achieve intravascular acoustic functions within complex physiological environments [38].

Ultrasound Elastography

Ultrasound elastography provides an imaging modality specifically sensitive to variations in tissue stiffness. The system calculates the relative or absolute mechanical stiffness of the underlying structure by measuring tissue motion or the propagation velocity of shear waves. These acoustic methods exploit the distinct alterations in soft tissue elasticity arising from specific pathological or physiological processes [39].

Solid tumours typically exhibit different mechanical properties relative to the surrounding healthy tissue. Medical professionals consequently utilise elastography to effectively differentiate diseased anatomy for precise diagnostic applications [40]. Figure 2.11 shows a combined shear wave elastography (SWE) image on the top and B-mode image on the bottom of a malignant lymph node. The elastography map highlights the metastases in red to indicate regions of significantly increased mechanical stiffness. The diagnostic system calculated a mean stiffness of 189.2 kPa for this specific lesion which is much larger than the established diagnostic threshold for metastases which is defined as 50 kPa [41].

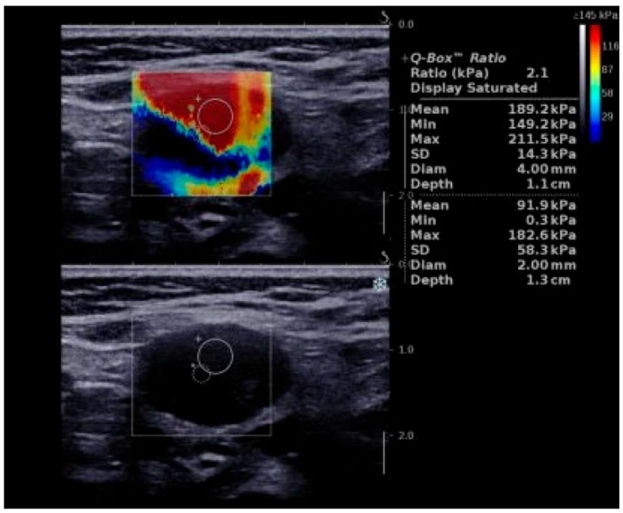

Figure 2.11 SWE (top) and B-mode (bottom) image of metastases [41]. (Modified with permission)

A miniature US transducer integrated within the MSCRs can potentially extract precise microstructural strain calculations, enabling the accurate mechanical characterisation of local arterial walls and plaques.

2.2.5 Multimodality Imaging

No single imaging technique provides a complete diagnostic picture despite the advanced capabilities of individual methods. Modern medicine increasingly utilises multimodality imaging to combine these technologies and offset their inherent limitations. Medical professionals frequently apply this synergistic strategy to integrate specific modalities highly complementary to US imaging. This section introduces two advanced hybrid technologies integrating optical mechanisms with US to maximise diagnostic precision.

Optical coherence tomography (OCT) and US

OCT provides high-resolution cross-sectional imaging of microstructures by measuring the backscattered signal of light [42]. This technique delivers sharp images with 1 - 15 μm resolution but suffers from shallow penetration depth due to significant optical attenuation. US complements this optical modality by offering better tissue penetration whilst possessing a spatial resolution one to two orders of magnitude lower than OCT [43]. Biomedical engineers have developed hybrid OCT-US catheters to bridge this diagnostic gap. Figure 2.12 is a schematic of a representative hybrid catheter which combines an US transducer and an optical lens within a single catheter tip.

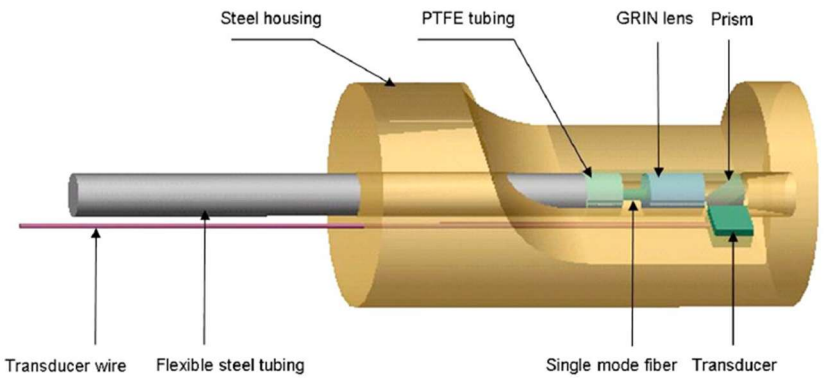

Figure 2.12 The structure of an OCT-US system [44]. (Modified with permission)

This advanced configuration allows clinicians to obtain a comprehensive structural view. In Figure 2.13, the optical system measures a rabbit aortic surface on the left,

while the integrated US transducer visualises deep-tissue information on the right. Clinical studies demonstrate that this dual approach significantly improves the diagnostic accuracy for lesions when compared to using either individual modality [44], [45].

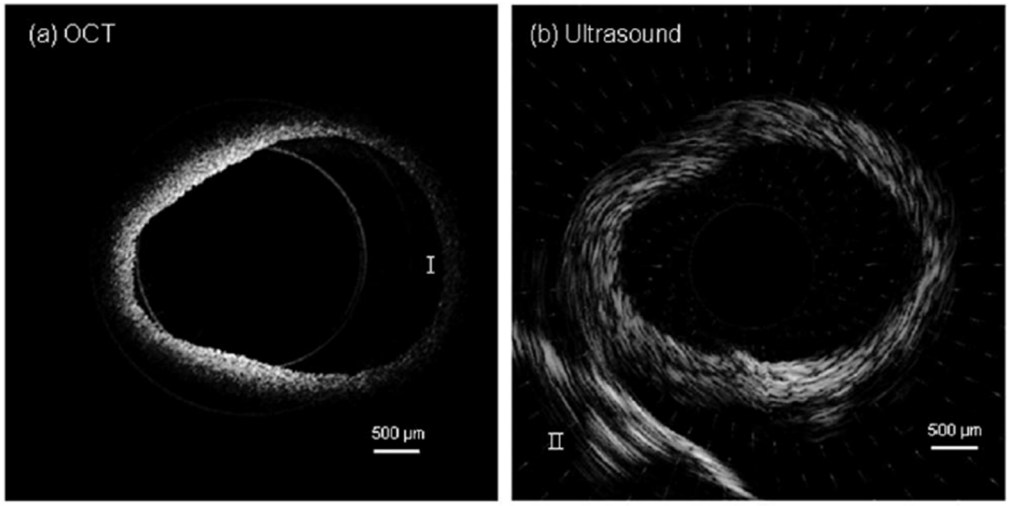

Figure 2.13 (a) OCT and (b) US images of the rabbit aorta [44]. (Modified with permission)

Photoacoustic imaging (PAI)

Another emerging hybrid modality is PAI. The underlying photoacoustic effect occurs when biological tissues absorb short laser pulses to undergo transient thermoelastic expansion. This rapid volumetric change generates US waves detectable by US transducers. This fundamental acoustic compatibility consequently allows integration with existing clinical US devices [46].

Figure 2.14A illustrates a complete PAI system. The system employs a multimode fibre and a lens to operate in a quasi-optical resolution mode yielding an extended working distance and enhanced optical energy transmission compared to conventional single-mode designs. A coaxial structure within a housing with a diameter of 1.8 mm aligns the optical components and the acoustic transducer on a single axis to enable simultaneous high-performance PAI without interference. Figure 2.14B presents the photoacoustic maximum amplitude projection (PAMAP) on the left and US maximum intensity projection (USMIP) images on the right transformed into a Cartesian coordinate system. The PAMAP clearly visualises the intricate vascular network of the rectal wall. The complementary USMIP displays highly echoic materials including

bone at an elevated intensity where a red dashed elliptical circle indicates the pubic bone as two separate hyperechoic lines.

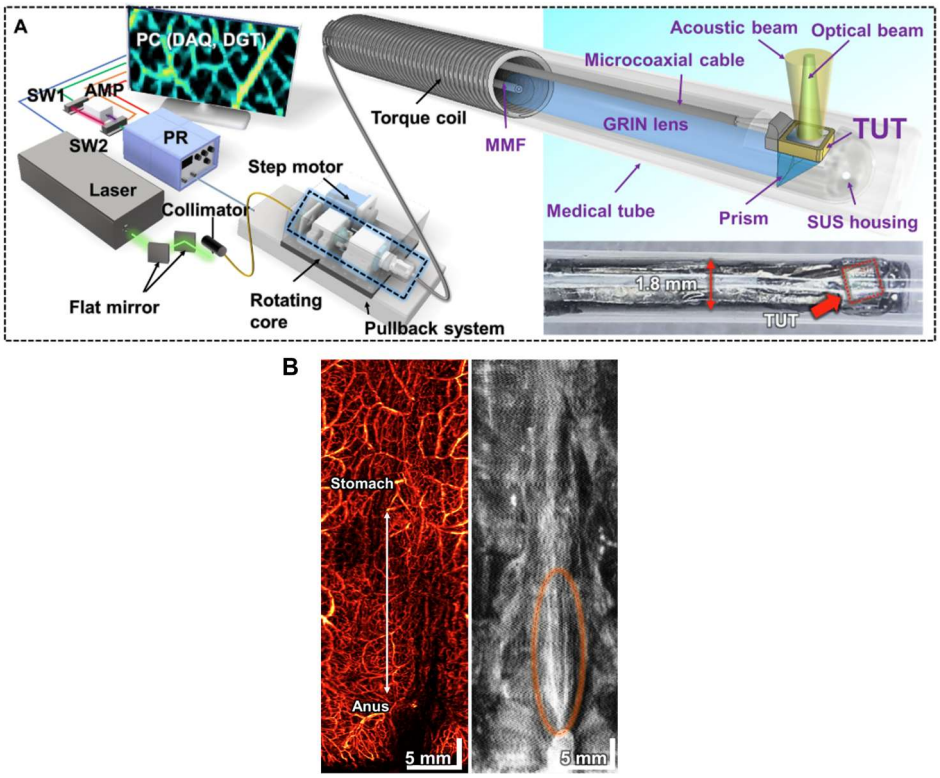

Figure 2.14 (A) Schematic of the PAI-US system and a photograph of the endoscopy. TUT: transparent US transducer; SW: switch; PR: pulser/receiver; AMP: amplifier; MMF: multimode fibre; SUS: steel use stainless (The Japanese industrial standard designation for stainless steel alloys); AISI classification system.; DAQ: data acquisition device; DGT: digitiser and (B) PAMAP and USMIP images [46]. (Modified with permission)

This synergistic combination confirms that US provides essential high-resolution anatomical context while PAI provides the necessary functional and molecular-specific contrast [46], [47], [48].

Integrating complementary optical modalities elevates fundamental US diagnostic capabilities. Internal clinical delivery of these advanced sensors currently relies on conventional passive catheters, imposing substantial manufacturing and navigational constraints. Future multimodal systems offer significant potential to utilise the MSCR as a clinical carrier to resolve these physical limitations. A review about the current clinical carrier systems is detailed in Section 2.4.

2.3 Piezoelectric US transducer

Now focusing on US devices, US transducer engineering encompasses three primary categories: piezoelectric US transducers, piezoelectric micromachined ultrasonic transducers (PMUTs) and capacitive micromachined ultrasonic transducers (CMUTs).

Piezoelectric US transducers use the reciprocal nature of the piezoelectric effect. The converse effect converts an applied electrical potential into mechanical oscillations. The direct effect subsequently transforms returning acoustic echoes into electrical signals for data reception. This highly mature technology demonstrates exceptional operational stability combined with superior transmit and receive sensitivities [49]. Though these robust attributes have established piezoelectric US transducers as the undisputed gold standard for clinical US imaging, several inherent engineering limitations persist. These primarily comprise acoustic impedance mismatches alongside the utilisation of toxic lead within piezoelectric material compositions. Besides, the fabrication process remains complex due to intricate steps such as high-precision dicing. [50].

Advances in microelectromechanical systems (MEMS) are driving the development of PMUTs. These miniaturised devices offer excellent intrinsic electrical characteristics alongside seamless integration with application-specific integrated circuits (ASICs) [50]. Figure 2.15 shows a standard PMUT structure comprising a piezoelectric membrane formed by a patterned layer stack deposited directly on a silicon wafer. The application of an excitation voltage between the top and bottom electrodes drives this suspended membrane. The applied electric field induces transverse stress within the active piezoelectric layer. This specific stress profile forces the membrane to displace out of plane, generating a propagating pressure wave in the surrounding medium [51]. Structural manufacturing challenges remain a significant barrier. The engineering requirement for an exceptionally thin fabricated membrane often leads to physical cracking during processing. The operational frequency of the PMUT also exhibits extreme sensitivity to residual stress retained within the active piezoelectric layer [50].

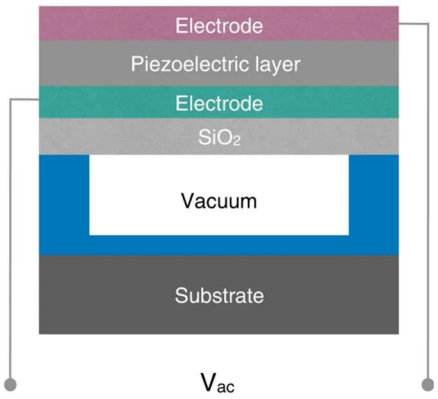

Figure 2.15 Schematic of a PMUT [50]. (Modified with permission)

CMUTs represent an alternative semiconductor-fabricated ultrasonic technology. Figure 2.16 shows the basic structure of a CMUT cell, which comprises a thin flexible membrane suspended over a vacuum cavity. A thin metallic layer deposited over this membrane functions as the top electrode. The underlying silicon substrate acts as the bottom electrode. An insulation layer deposited directly upon this silicon substrate effectively prevents mutual electrical contact between the two active electrodes [52], [53], [54]. This specific transducer structure yields a low acoustic impedance combined with good receive sensitivity. The inherently broad frequency bandwidth consequently produces exceptional axial imaging resolution [49]. However, there are some functional challenges, including chronic dielectric charging, low overall electromechanical efficiency, and inadequate transmit sensitivity [53], [54].

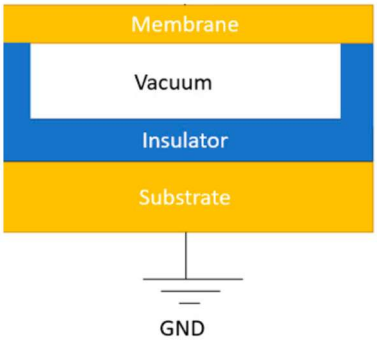

Figure 2.16 Schematic of a CMUT [53]. (Modified with permission)

While new micromachined technologies offer great theoretical potential, intricate fabrication requirements and structural fragility hinder clinical adoption for specialised robotic integration. The conventional piezoelectric transducer represents the most practical choice for this research project because of the proven reliability and mature manufacturing processes of standard piezoelectric materials. Meanwhile, these traditional devices ensure consistent acoustic performance during physical integration

with the MSCR platform. Therefore, this thesis focuses on the development and testing of US transducers based on piezoelectric material.

2.3.1 Transducer structure

Upon electrical excitation, the piezoelectric element resonates at its natural operational frequency. A fundamental engineering challenge arises from the significant acoustic impedance mismatch between the active piezoelectric ceramic, with an impedance of approximately 30 MRayl, and the target biological tissue, similar to water, with an impedance of roughly 1.5 MRayl. This substantial physical difference dictates strong energy reflection at the boundary interface in the absence of appropriate acoustic matching. Such internal reflections severely compromise both the overall diagnostic sensitivity and the operational bandwidth of the transducer.

Figure 2.17 illustrates the standard three-port network model utilised to mathematically analyse the complex electromechanical dynamics. This established analytical framework includes one electrical port and two distinct mechanical ports. The electrical port defines the direct connection to the driving voltage source. Simultaneously, the two mechanical ports characterise the physical boundaries corresponding to the front matching layer and the rear backing structure.

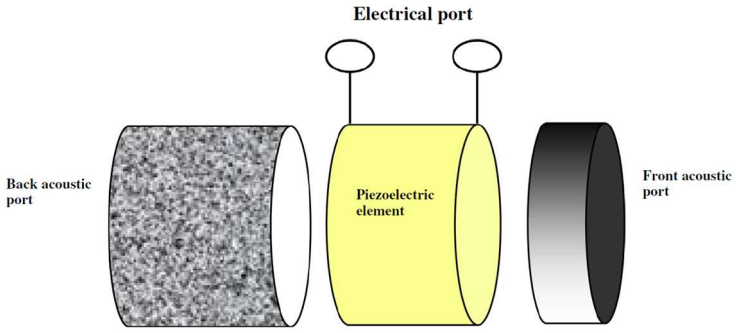

Figure 2.17 Basic structure of the piezoelectric transducer [55]. (Reuse with permission)

2.3.2 Transducer design

Each layer within the acoustic stack possesses a characteristic acoustic impedance, a fundamental property that dictates the transmission and reflection of acoustic energy at the interfaces [56]:

$$Z = \rho c \qquad \text{Eq. 2.1}$$

where ρ is the density of the layer and c is the speed of sound in the material.

For wideband transducer behaviour, the ideal thickness of the matching layer is λ/4, and the acoustic impedance of the matching layer is calculated as follows [57]:

$$Z_{\mathrm{m}} = \sqrt{Z_1 Z_2} \qquad \text{Eq. 2.2}$$

where Z_m is the acoustic impedance of the matching layer, whilst Z_1 and Z_2 are the acoustic impedances of the piezoelectric material and load medium, respectively. For a transducer with two matching layers, which can further increase the transmission efficiency of the US, the acoustic impedance can be described as [58]:

$$Z_{\mathrm{m1}} = \sqrt[7]{Z_1^4 Z_2^3} \qquad \text{Eq. 2.3}$$

$$Z_{\mathrm{m2}} = \sqrt[7]{Z_2^6 Z_1} \qquad \text{Eq. 2.4}$$

To quantify the performance of the piezoelectric active layer, three intrinsic parameters are critical: the piezoelectric coefficient, d_{33}, the electrical coupling coefficient, k_t, and clamped relative dielectric constant, ε_{33}^{S}.

The coefficient d_{33} represents the longitudinal strain induced per unit electric field. In tensor notation, the subscript '33' indicates that both the applied electric field and the resulting mechanical displacement occur along the material's poling axis. k_t serves as a measure of the material's transduction effectiveness. It is defined as the ratio of the stored converted energy to the total input energy. According to the IEEE standard on piezoelectricity, k_t is expressed as [59]:

$$k_t = \sqrt{\frac{\pi f_r}{2 f_a} \tan\left(\frac{\pi}{2} \frac{f_a - f_r}{f_a}\right)} \qquad \text{Eq. 2.5}$$

where f_r is the electrical resonance frequency and f_a is the electrical anti-resonance frequency of the material.

ε_{33}^{S} is a critical parameter that quantifies the material's ability to store electrical charge at high frequencies. This parameter fundamentally determines the transducer's static capacitance (C), which in turn dictates the electrical impedance match with the driving

electronics. The relationship between the electrical impedance magnitude Z_e and ε_{33}^S can be described as follows [60]:

$$Z_e = \frac{t}{2\pi f A \varepsilon_{33}^S \varepsilon_0} \quad \text{Eq. 2.6}$$

where t is the thickness of the material, f is the operating frequency, A is the area of the piezoelectric layer, and ε_0 is the vacuum permittivity. A higher ε_{33}^S is generally desirable for miniature transducers to prevent the impedance from becoming prohibitively high.

Theoretically, perfect acoustic transmission cannot be achieved through front-face matching alone. Due to the inherent impedance discontinuity at the boundaries, internal reflections within the piezoelectric element cause reverberation, resulting in an extended pulse duration, known as ring down [61]. For imaging applications, such temporal elongation severely degrades axial resolution. To mitigate this, a backing component is bonded to the rear face of the transducer. Its primary function is to dampen free vibrations by absorbing the acoustic energy radiated backwards, thereby shortening the spatial pulse length and broadening the bandwidth [62].

2.3.3 Piezoelectric materials

The performance of an US transducer is strongly related to the electromechanical properties of its active material. Currently, materials are categorised into five primary classes based on their structural composition: conventional lead zirconate titanate (PZT) ceramics, relaxor-based single crystals, piezoelectric polymers, textured ceramics, and composites.

Lead Zirconate Titanate (PZT) Ceramics:

Among the various piezoelectric candidates, PZT historically represented the ubiquitous industry standard for medical US transducers. Its dominance stems from the morphotropic phase boundary (MPB), a composition at which rhombohedral and tetragonal crystal phases coexist. This structural instability allows for easy polarisation reorientation, resulting in high values of k_t, d_{33} and ε_{33}^S [63]. Furthermore, PZT is highly adaptable because dopants can tailor its properties. This approach optimises soft PZT for high-sensitivity sensing and hard PZT for high-power transmission [63].

Relaxor-PT Single Crystals:

In recent decades, relaxor-lead titanate-based single crystals, such as PMN-PT or PZN-PT, have gained prominence in diagnostic imaging. Unlike polycrystalline ceramics, these domain-engineered crystals exhibit giant piezoelectricity, offering significantly higher strain levels and electromechanical coupling (k_{33} > 0.9) compared to conventional PZT [64]. This enables transducers with superior sensitivity and exceptionally broad bandwidths. However, these benefits come with trade-offs: single crystals are mechanically fragile, prone to fracture during dicing, and possess a lower coercive field and phase transition temperature, limiting their thermal stability [65]. Moreover, utilising k_{33} requires specific tall, narrow material structures.

Piezoelectric Polymers:

For specific reception-based applications, piezoelectric polymers such as polyvinylidene difluoride, PVDF, and its copolymer, P(VDF-TrFE), offer a unique advantage: low Z. This value is closely matched to biological tissue, minimising reflection at the interface and resulting in a broad frequency response [66]. Consequently, PVDF is the material of choice for wideband hydrophones [67], [68]. However, its low dielectric permittivity and weak k_t limit its efficacy in transmission, as it cannot generate sufficient acoustic power for deep tissue penetration [19].

Textured Piezoceramics:

Textured piezoelectric ceramics combine the superior electromechanical capabilities of single crystals with the structural robustness of conventional ceramics. Fabricated mainly using templated grain growth [69], these materials are engineered to align their crystalline grains along a specific crystallographic axis (typically <001>) within a polycrystalline matrix (Figure 2.18). This microstructural orientation imparts good piezoelectric properties, achieving d_{33} values similar to single crystal, i.e. nearly double that of PZT ceramics, while maintaining the superior mechanical fracture toughness and lower manufacturing costs associated with conventional ceramics [70]. This balance makes textured ceramic a promising candidate for next-generation high-frequency transducers, where both performance and durability are required [69].

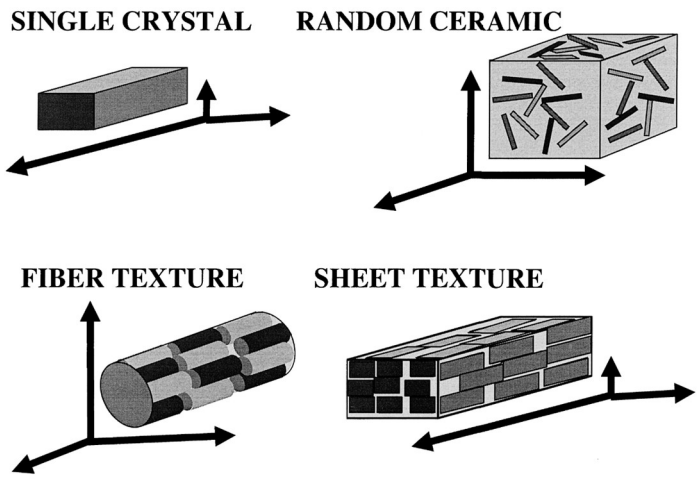

Figure 2.18 Different types of texture compared with a single crystal and random ceramic [69]. (Reuse with permission)

Piezocomposite:

To overcome the inherent acoustic impedance mismatch between piezoelectric materials and the propagation medium, the development of piezoelectric composites represented a fundamental structural evolution. In particular, the 1-3 connectivity composite structure has been widely adopted (Figure 2.19), with active ceramic pillars embedded within a passive polymer matrix [71]. This structural modification fundamentally alters the electromechanical boundary conditions of the active layer.

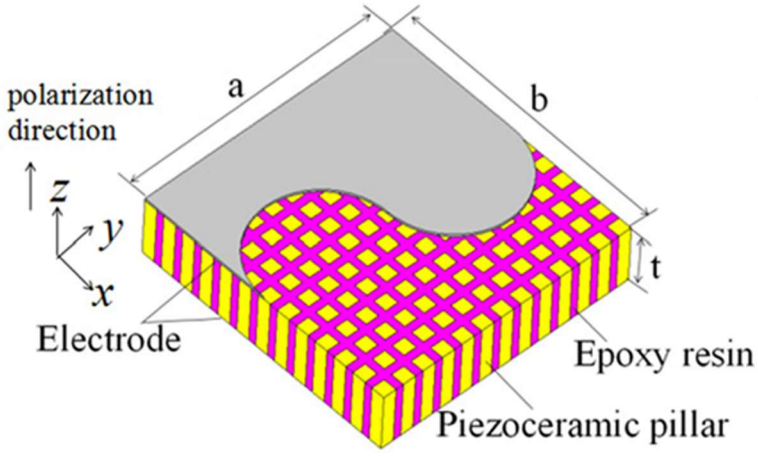

Figure 2.19 Schematic of a 1-3 piezoelectric composite structure [72]. (Modified with permission)

The primary advantage of introducing a polymer phase is the substantial reduction in acoustic impedance. By replacing dense ceramic material with a lightweight, compliant polymer, the effective acoustic impedance can be reduced from

approximately 30 MRayl to below 18 MRayl [1], [73], [74]. This results in a much closer impedance matching to biological tissue, thereby significantly improving acoustic energy transmission efficiency.

Additionally, the compliant polymer matrix mechanically decouples the ceramic pillars, mitigating the lateral clamping effects inherent in bulk piezoelectric materials. This boundary condition enables the pillars to vibrate as free rods in the efficient longitudinal mode rather than in a laterally clamped mode [71]. Consequently, the k_{eff} is maximised, approaching k_{33}, leading to substantial enhancements in both transducer sensitivity and operational bandwidth according to design choices [75].

The design of 1-3 piezocomposites requires rigorous optimisation of the ceramic volume fraction (VF). Composite transducers typically employ a volume fraction between 40% and 70%, as illustrated in Figure 2.20. A lower fraction near 40% optimises receiving sensitivity by maintaining a low acoustic impedance. A higher volume fraction approaching 70% maximises transmission efficiency. Variations in the volume fraction modify ε_{33}^{S} of the composite. The dimensions of the transducer should incorporate this dielectric value according to Equation 2.6 to achieve a target electrical impedance near 50 Ω [1].

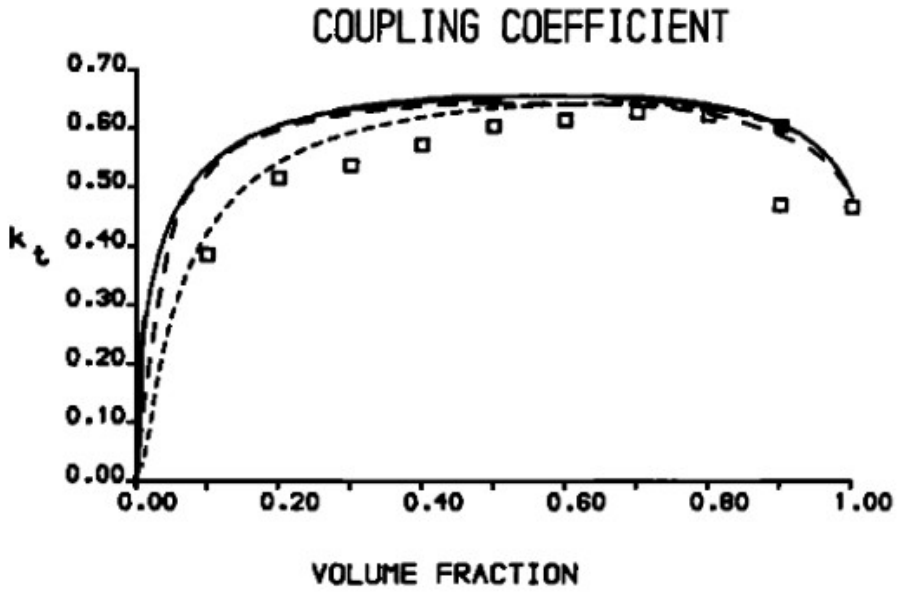

Figure 2.20 Relationship between volume fraction and coupling coefficient [76]. (Reuse with permission)

In addition to VF, the physical dimensions of the pillars are critical for maintaining vibrational purity. The pillar aspect ratio (AR) is defined here as the pillar height divided by its lateral width. A high AR produces slender pillars, shifting their lateral resonances to frequencies above the intended thickness-mode resonance and thereby reducing spurious responses within the operating frequency band. Conversely, a low AR may bring unwanted lateral modes close to the thickness resonance. A balance between VF and AR is therefore required, since increasing VF may require wider pillars and consequently reduce the AR. As a practical design guideline, a minimum AR of approximately 3:1 is commonly recommended to maintain pure thickness-mode operation [77].

While the 1-3 connectivity approach is widely used for single-element transducer development, 2-2 connectivity offers a more favourable balance between performance and manufacturability for 1D array transducer fabrication. By exploiting the height-extensional (beam) vibration mode, which exhibits a high electromechanical coupling coefficient [78], 2-2 composites can achieve broader bandwidths than conventional array structures without the manufacturing intricacy of 1-3 composite. Importantly, the sensitivity of 2-2 composite arrays is comparable to that of their 1-3 composite [79], [80], while offering a simpler and more reliable fabrication process. Consequently, in this thesis, a sub-dicing technique was adopted to realise a 2-2 composite structure for the array transducer and a 1-3 composite structure for the single-element transducer fabrication.

Meanwhile, the selection of PIN-PMN-PT single crystal for MSCRs was primarily based on its excellent performance. Although single crystal materials are relatively expensive, the fabrication of high-frequency transducers requires minimal material volume because of the small aperture size. In addition, the work aims to validate the feasibility of integration with the MSCRs, rather than to optimise transducer performance at this stage.

Compared with PMN-PT single crystal, PIN-PMN-PT single crystal offers improved thermal stability [1], which is important for fabrication and operation. Therefore, a trade-off was made between performance, cost, and the requirements of this proof-of-concept study. Based on these considerations, PIN-PMN-PT single crystal was selected as the active layer for MSCRs. In Chapter 5, the more advanced

Sm:PIN-PMN-PT single crystal was investigated to explore future optimisation of transducer performance for MSCR applications.

2.4 Carrier platforms for high-frequency US transducers

High-frequency US (frequency > 15 MHz) enables finer resolution for tissue layers, such as arterial walls or the mucosal layers of the gastrointestinal tract [62], [81], [82], [83], [84]. This resolution is critical for detecting and staging lesions that are invisible to standard imaging modalities. However, the physics of US propagation in media dictates that attenuation increases with frequency [85]. Therefore, the transducer must be physically inserted into the body, navigating lumens or cavities to reach the target tissue. This operational requirement imposes coupled engineering challenges upon the acoustic stack design and mechanical carrier. The carrier must provide a protective housing that shields the piezoelectric transducer and micro-coaxial interconnects while serving as a steerable delivery vehicle that navigates the transducer through potentially tortuous anatomy to reach the target position.

The design of these platforms requires a fundamental compromise between anatomical access and mechanical control. For example, highly flexible devices can navigate deep into the coronary vasculature but are susceptible to buckling under insertion forces. Conversely, rigid instruments offer stability but lack the compliance needed to traverse complex anatomies such as the sigmoid colon. Current clinical deployment strategies fall into four main mechanical architectures: flexible catheters, endoscopic systems, ultrasound-integrated needles, and capsule systems. The following review evaluates the mechanical principles, clinical implementation, and limitations.

2.4.1 Flexible catheter

A flexible catheter serves as the primary platform for minimally invasive diagnostics, most notably in intravascular ultrasound (IVUS). These devices are engineered to navigate extended vascular pathways to reach coronary or peripheral targets. As described by Nissen and Yock [86], the catheter body is typically a composite structure with a length exceeding 100 cm, comprising a lubricious inner liner, a braided reinforcement layer for torque transmission, and a soft outer polymer jacket. The fundamental operational principle relies on proximal actuation. The device possesses no intrinsic degrees of freedom (DoF) for active steering; instead, the operator manipulates an external handle, applying axial force to advance the tip and torque to

orient the imaging plane. Navigation depends on the ability of the device to track over a pre-placed guidewire, utilising it as a monorail to facilitate insertion into specific vascular branches [87].

Two primary transducer configurations exist within this platform, each with distinct mechanical implications. The first involves mechanical rotation. In Figure 2.21, a single-element transducer is mounted at the distal tip of a flexible drive cable spanning the length of the catheter. A motor housed in the proximal handle rotates this cable at high speed, sweeping the US beam to generate a cross-sectional image. The system incorporates a laser and couplers to enable OCT. These optical components operate concurrently alongside the US components to achieve multimodal imaging. While this design enables the integration of higher-frequency transducers and simplifies the fabrication of the acoustic stack, it introduces complex tribological challenges arising from the rotation of the core within a stationary sheath [88].

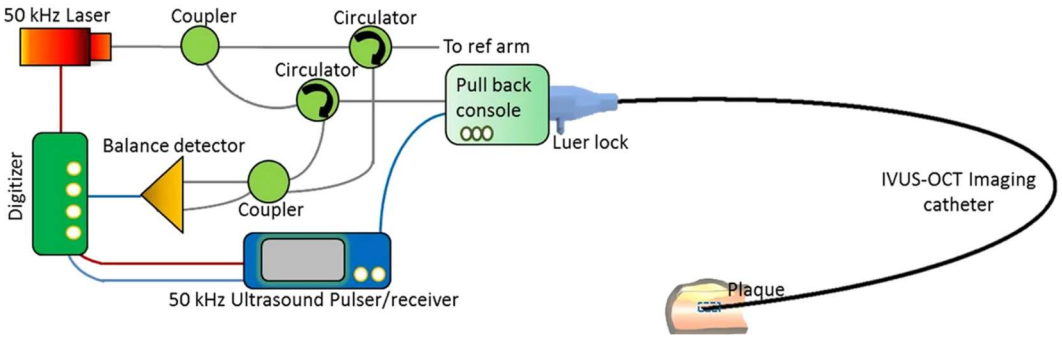

Figure 2.21 A schematic illustration of an IVUS imaging system [89]. (Reuse with permission)

The second configuration employs an array configuration. These catheters utilise a circular array of miniaturised piezoelectric elements distributed circumferentially around the distal tip. The array transmits and receives US signals radially. Beam steering is executed electronically via multiplexing ASICs integrated within the device tip [86], [90]. However, the inherent complexity of the required wiring and microelectronics frequently necessitates a larger element pitch and yields a lower f_c (typically < 20 MHz) than mechanically rotated systems [91].

2.4.2 Endoscopic system

For applications requiring high mechanical stability or the capacity for physical intervention (such as tissue biopsy), clinical practice utilises endoscopic US (EUS).

Unlike vascular catheters, these systems are engineered to navigate the larger lumens of the gastrointestinal tract and lungs, designed to achieve a functional equilibrium between structural stability and anatomical flexibility [92].

EUS instruments have larger dimensions and greater bending stiffness than intravascular catheters. They feature a semi-rigid insertion tube that houses US transducers, steel pull-wires for lever-driven tip deflection, and larger working channels to accommodate auxiliary instruments, as shown in Figure 2.22. The distal tip incorporates either an array [93] or a single-element transducer [94]. The inherent rigidity of the shaft constitutes a critical functional feature, enabling the operator to press the transducer firmly against the gastric or duodenal wall. This mechanical apposition ensures acoustic coupling and minimises respiratory motion artefacts during image acquisition [95].

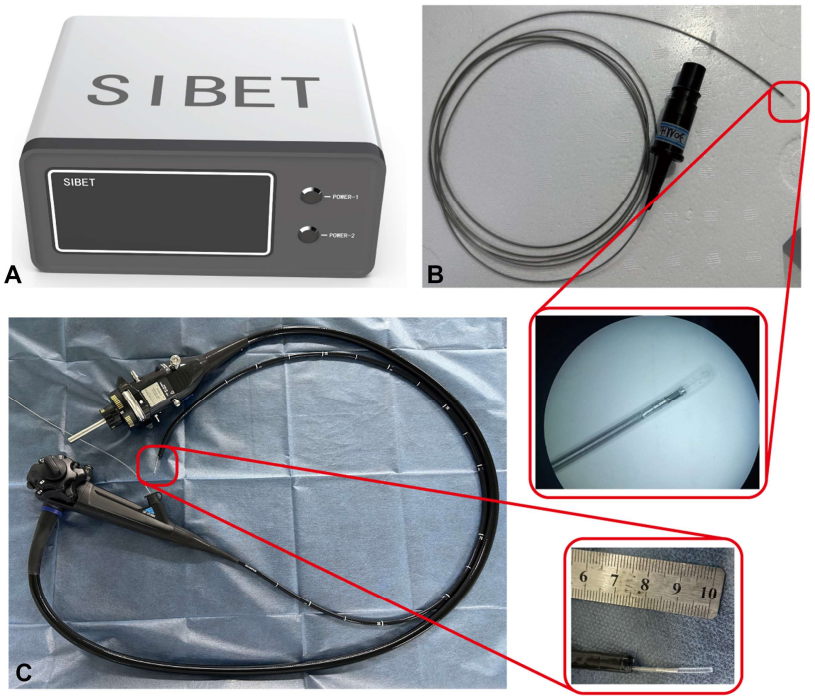

Figure 2.22 A photo of an EUS control system. A: US imaging device, B: a photo of the US micro probe and C: an endoscopic device equipped with an US micro probe [92]. (Reuse with permission)

A principal advantage of the EUS platform is its ability to serve as a stable foundation for deploying secondary instruments. Minami described the mechanics of EUS-guided fine-needle aspiration, in which a rigid needle is advanced through the working channel to puncture the gastrointestinal wall, enabling sampling of target tissues such

as lymph nodes, pancreatic masses, or cysts. The mechanical stability afforded by the semi-rigid endoscope shaft is critical for precise targeting and tissue acquisition [96].

2.4.3 US-integrated needle

The rigid needle represents an alternative carrier architecture for intracorporeal ultrasound. Rather than functioning solely as a passive puncture instrument, the needle shaft serves as a rigid conduit to deliver a miniature US transducer directly into deep soft tissues. These active needle systems are typically engineered with specific directional capabilities to suit the interventional trajectory. These include forward-looking configurations, where the transducer is mounted at the distal vertex to visualise tissue layers ahead of the puncture path [97], [98], and angled or side viewing designs [99], [100], where the element is integrated into the needle bevel or a lateral fenestration to assess the surrounding anatomical information.

The strict spatial constraints within the needle bore necessitate the miniaturisation of the US transducer, which consequently dictates the use of high operating frequencies. For instance, the fabrication of a high-performance 39 MHz needle transducer incorporating a modified PMN-PT single crystal with an ultrahigh clamped dielectric constant is detailed in [60]. Structurally, this device features a miniature aperture housed within a stainless-steel needle. This integrated configuration enables the instrument to function as a forward-looking scanner yielding real-time feedback on tissue strata directly from the distal tip, as illustrated in Figure 2.23.

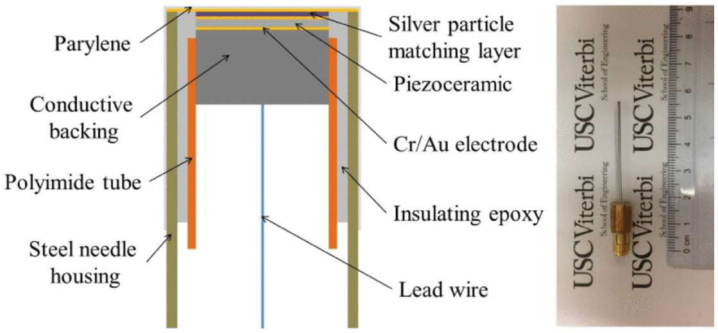

Figure 2.23 The schematic of the transducer and a photo of the transducer-integrated needle [60]. (Reuse with permission)

Advancing this architecture toward volumetric imaging, a stepped 2D array needle transducer was recently introduced. To fit a high-density array into a cylindrical needle without increasing the cross-sectional profile, a unique stepped substrate structure was engineered to accommodate 256 elements with a 100 μm pitch at the distal tip, as

shown in Figure 2.24. This geometric arrangement enables the generation of real-time 3D US images directly ahead of the needle. Preclinical validation demonstrated that this system provides comprehensive spatial depth perception during spinal puncture procedures. This capability allows clinicians to visualise the complex bony anatomy of the vertebrae and the spinal canal in 3D, representing a functional advancement unattainable using single-element transducers [101].

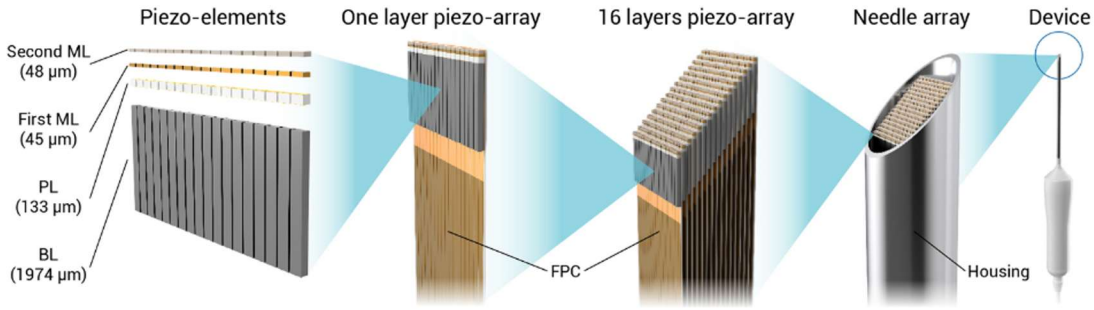

Figure 2.24 The schematic of the structure of the array needle transducer with design parameters. ML, matching layer; PL, piezo ceramic with an Au/Cr; BL, backing layer; FPC, flexible printed circuit [101]. (Modified with permission)

2.4.4 Capsule system

Capsule-based US systems have been developed to provide imaging in gastrointestinal (GI) tract that are difficult to access using conventional EUS. According to the mechanism used to generate the US scan, these systems can be broadly divided into three categories: internal mechanical scanning using a single-element transducer, electronic scanning using circular arrays, and external magnetic actuation of the transducer or the entire device.

A representative internal mechanical-scanning system is shown in Figure 2.25. In this design, a 39 MHz single-element transducer was connected to a rotary solenoid and gear mechanism. As the motor rotates, the transducer sweeps a 360° radial sector to enable cross-sectional imaging of the intestinal wall [102]. This rotation mechanism was also incorporated into a tethered multimodal optical-US capsule for first-in-human oesophageal imaging and subsequent evaluation in the porcine stomach and small bowel [103], [104]. Mechanical scanning provides wide angular coverage using relatively simple channel electronics. However, the motor and transmission mechanism increase device volume and power consumption [81].

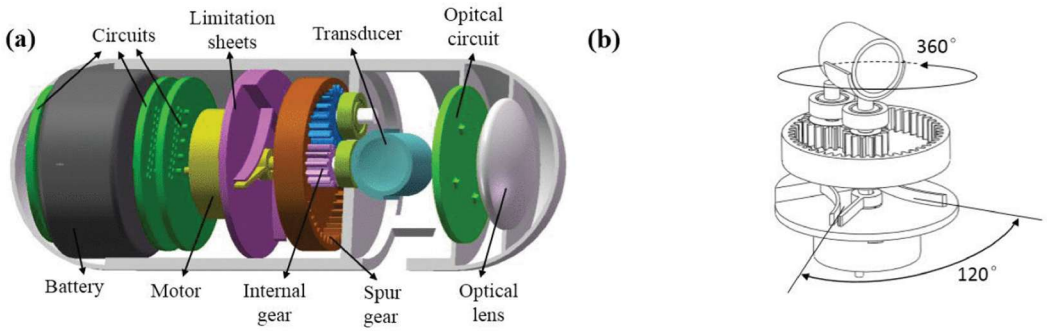

Figure 2.25 The structure of the US transducer integrated capsule: (a) the schematic of the capsule and (b) the rotation mode of the device [102]. (Modified with permission)

Alternative systems use electronic scanning with circular arrays. A 25 MHz circular array configuration comprising a segmented transmit ring and a 512-element receive array was investigated for cross-sectional GI tract imaging [105]. In this configuration, array elements are sequentially activated to generate images without rotating the transducer. The absence of an internal motor reduces mechanical complexity and permits more flexible scanning sequences. However, the increased element count introduces challenges in array fabrication, electrical interconnection and power management.

Despite advances in scanning capability, most reported US capsules remain tethered for navigation and positioning with limited active control. To overcome this limitation, recent research has focused on external magnetic manipulation to achieve precise navigation. However, the main limitation of standard cylindrical capsules involves a physical restriction to a maximum of 2 DoF in orientation. This restriction prevents precise targeting and necessary rolling motion during clinical procedures. Researchers employ an asymmetrical oloid-shape capsule to resolve this operational limitation. By embedding a 28 MHz high-frequency US array within the capsule, this synergistic integration realised comprehensive 3D histological imaging for gastrointestinal subsurface tissue [106].

Capsule-based US systems offer less invasive access to remote GI regions and subsurface imaging beyond optical capsule endoscopy. This specific anatomical environment presents a significantly larger cross-sectional area compared to human vascular system. This inherent size limitation prevents deep access into narrower physiological lumens. The miniature US transducers integrated MSCRs are also manipulated under remote magnetic control. This thesis executes initial *in vivo*

evaluations of this robotic platform within the GI tract to establish a fundamental baseline for future optimisation and diagnostic imaging within narrower anatomical environments.

2.4.5 Magnetic soft continuum robots

Conventional intracorporeal US transducers rely on passive mechanics and contact-dependent steering to navigate anatomical pathways [107]. These tethered systems exhibit limited DoF as well as non-linear force transmission and significant frictional dissipation [108]. The demand for miniaturisation and enhanced control is motivating the use of compliant materials to ensure safe navigation within complex luminal environments. The development of soft continuum robots (SCRs) partially resolves the inherent mechanical constraints and high force loss of conventional clinical instruments [109], [110], [111].

MSCRs represent an advanced variant of compliant architecture. Engineers embed magnetic segments within a thin elastomeric silicone matrix. This structural integration achieves remote actuation with high DoF at the millimetre scale [112]. Magnetic actuation shifts the navigation process from passive contact to active contactless steering. An external magnetic field exerts a specific torque on the functional tip. This applied force enables precise spatial orientation independent of the primary insertion vector. Recent developments enhance this physical capability using customised magnetisation profiles for atraumatic shape formation [113]. Reprogrammable magnetic moments provide critical intraoperative adaptability [114]. Active stiffness mechanisms further improve overall structural control [115]. These integrated functionalities enable the device to actively select specific paths through complex luminal environments. The platform navigates curved anatomical pathways using smooth adaptive motion which reduces internal frictional contact forces.

The absence of integrated sensing mechanisms creates a fundamental engineering bottleneck for MSCRs. Although strategies employing fibre Bragg grating (FBG) sensors [69] or Hall-effect sensors [116] have been proposed to provide real-time feedback on the shape and spatial position of the robot, they do not provide information about the local anatomical environment [117], [118]. Furthermore, embedding such instrumentation frequently necessitates a compromise in mechanical compliance; semi-rigid fibres or discrete sensor nodes effectively increase the bending stiffness of

the soft body, thereby constraining miniaturisation and the capacity to conform to tortuous anatomies. Consequently, operators must continue to rely on external imaging modalities such as fluoroscopy for navigation, increasing the working space and radiation exposure.

2.5 Significance of the research

This research resolves certain technical limitations of existing intracorporeal carriers. Traditional flexible catheters experience significant frictional dissipation during operation. A rigid needle inherently induces tissue trauma during deep intervention. The capsule has macroscopic dimensions that preclude navigation through narrow physiological lumens.

MSCRs resolve specific navigation and dimensional problems through remote magnetic steering and soft, slender bodies. This research validates the proof of concept combining these robotic platforms with US transducers. In this research, two version integration strategies are developed and characterised, evaluating specific sweep-scan capabilities for forward object imaging and rotational-scan capabilities for cross-section imaging under *ex vivo* conditions. *In vivo* rotational scan evaluations establish a research foundation for future optimisation.

In this thesis, the development and characterisations of single-element transducers and 1D linear arrays using novel Sm:PIN-PMN-PT single crystal piezoelectric materials were conducted. These evaluations demonstrate exceptional material sensitivity and broad bandwidth, confirming this specific material as a transducer candidate for MSCRs integration and broader biomedical US applications.

Chapter 3 Ultrasound transducer design and fabrication

3.1 Introduction

This chapter describes the design and fabrication of miniature US transducers. It focuses on piezocomposite single-element transducers and 1D linear arrays. The single-element transducers were developed for integration with MSCRs. They must be miniature for integration while providing suitable acoustic performance. A centre frequency of 15 MHz was selected to balance spatial resolution and penetration depth. Higher frequencies can improve spatial resolution. However, acoustic attenuation increases with frequency and reduces the useful penetration depth [3]. Higher frequency transducers also require thinner active layers and finer composite structures, which increase fabrication difficulty. Therefore, 15 MHz was selected for the proof-of-concept MSCR platform.

Following the selection of the centre frequency, simulation was used to determine the active layer thickness and aperture size. The aperture size affects the transducer capacitance and electrical impedance. These parameters influence energy transfer between the transducer and the 50 Ω pulser-receiver system. Reducing the aperture would facilitate MSCR integration but would also reduce the capacitance and affect electrical energy transfer [1]. The final single-element transducer dimensions were selected to remain compatible with the MSCR while maintaining good acoustic output.

The fabrication methodology relies on micromachining processes. Precision lapping is used to control the thickness of each layer. Dicing is used to form the composite structures and separate the array elements. The matching layers and backing layer are then assembled. Electrical connections are subsequently prepared. These procedures were adapted where necessary to meet the dimensional and integration requirements of the MSCR. Section 3.4 describes the equipment and fabrication procedures. It also discusses the practical problems encountered during fabrication and the approaches used to address them.

Beyond the manufacturing process, this chapter describes the characterisation performed before and after transducer finalisation. The passive material properties are measured for simulation and acoustic layer design. All the characterisation results

provide the technical basis for the MSCR integration and transducer studies presented in Chapters 4 and 5.

3.2 Simulation

PiezoCAD (Sonic Concepts, WA, USA), a commercial software package widely used for US transducer modelling, is based on the 1D KLM equivalent electrical circuit model [119]. This approach calculates the acoustic system response between the electrical terminals and the front acoustic port.

Material properties for the piezoelectric active elements are required input. In this thesis, PMN-PT, PIN-PMN-PT and Sm:PIN-PMN-PT single crystals were used. Similarly, properties for matching layers, backing layers, and the load medium were individually defined including layer thickness, sound velocity in the material and density.

The software generates key output functions. These include electric impedance, pulse-echo response in time and frequency domain and two-way insertion loss (IL). In this thesis, research focuses on transducer design and optimisation. The 1D model resolves the longitudinal wave propagation. This mathematical approach accurately and rapidly determines layer thickness and area dimensions. Meanwhile, this research incorporates 1-3 and 2-2 composite manufacturing techniques during fabrication which can isolate unwanted lateral vibration modes [1].

The 1D KLM model offers accurate simulation accuracy for single-element transducers and provides clear physical insight into layer-by-layer acoustic transmission. However, this analytical method is inherently less suitable for array simulations, as arrays require more rigorous multidimensional acoustic field analysis. Finite element analysis (FEA) can provide detailed simulations for complex acoustic field interactions. This multidimensional approach can evaluate lateral interference during array design and analyse dynamic material deformation. However, these capabilities are beyond the main scope of this thesis. The complex boundary conditions required in FEA may also introduce unnecessary computational complexity.

The primary aim of this thesis is to investigate the integration of US transducers with MSCRs, rather than to perform exhaustive US transducer optimisation. For this

purpose, the KLM model provides an efficient computational framework that is sufficient to support the initial proof of concept. Consequently, PiezoCAD was used to design both the single-element and array transducers presented in this thesis.

3.3 Material preparation

This section describes the preparation for active layer and passive layers before transducer fabrication. As noted in Chapter 2, passive materials are important for optimisation of US transducer performance. The characterisation method for passive materials at high frequencies, reported previously [85], was adopted for this study. This method was applied to characterise preparations of Epo-tek 301 (Epoxy Technology, Billerica, United States) epoxy mixed with either 2–3 μm silver powder or alumina powder with different ratios.

Piezoelectric single crystal PIN-PMN-PT and Sm:PIN-PMN-PT used in the study were supplied by TRS Technologies, Inc. (State College, Pa, USA) and PMN-PT was supplied by CTS Corporation (Lisle, IL, USA). The primary objective of preparing piezoelectric materials is to determine their fundamental properties, which serve as essential parameters for subsequent simulation and transducer design.

3.3.1 Passive materials

The experimental setup for characterisation of passive materials (Figure 3.1) consisted of a pair of 5 MHz transducers (Olympus, Tokyo, Japan) axially aligned at a set distance within a water tank. Lapped samples were mounted on a holder and positioned centrally between the transducers. A 5-cycle, 5 MHz sinusoidal burst was generated by a function generator (T3AFG500, Teledyne Technologies, California, USA) via 50-Ω output impedance, driving the transmitting transducer. Having passed through the medium and sample, the signal was detected by the receiving transducer and subsequently recorded by an oscilloscope (IDS-1202B, RS Components Ltd, Northants, United Kingdom). To ensure acoustic coupling, the transducers and sample were immersed in deionised (DI) water at room temperature.

The time-of-flight (ToF) difference (Δt_l) for longitudinal propagation through the sample was determined by cross-correlating the signal acquired with the sample in the path against a reference signal acquired without the sample (i.e., a water-only path).

Δt_l is related to the longitudinal acoustic velocity in the sample (c_l) by the following equation [120] :

$$\Delta t_l = t_1 - t_2 = \frac{D}{c_i} - \left(\frac{D-d}{c_i} + \frac{d}{c_l}\right) = \frac{t}{c_i} - \frac{t}{c_l} \qquad \text{Eq. 3.1}$$

where t_1, t_2 are the two signal start times, D is the distance between the transducers, t is the thickness of the measured samples and c_i is the longitudinal velocity in water.

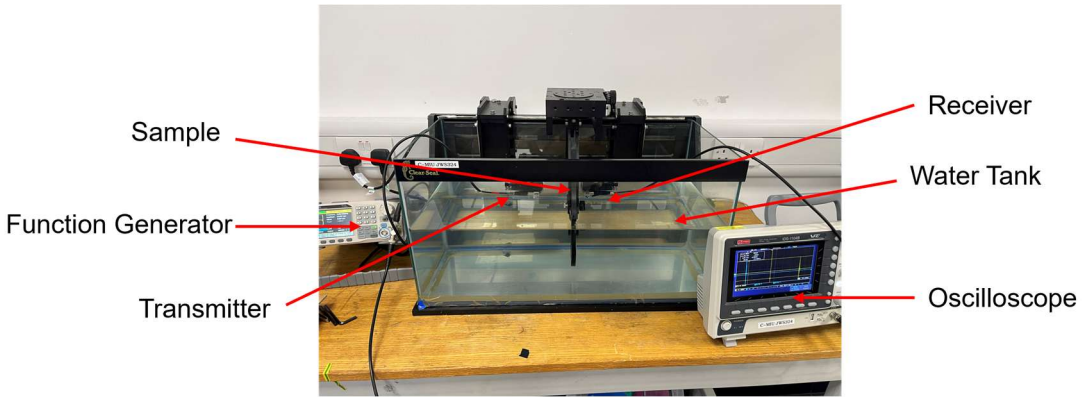

Figure 3.1 Set-up for ToF measurement.

The initial material for matching layers were selected based on the literature [121], [122]. As the reported materials were unavailable, alternative formulations with comparable acoustic impedances were prepared and experimentally evaluated. Three samples were tested for each ratio, and the mean results presented in Table 3.1 were used to select the most suitable formulation. For fabrication, all samples were cast into cylindrical moulds. Following curing, the samples were demoulded, lapped to a specific target thickness, and polished to minimise acoustic losses. The final diameter, thickness, and weight of each polished sample were measured for subsequent calculations.

Table 3.1 Properties of multiple passive material samples.

Sample*	Density (g/cm^3)	Speed of Sound (m/s)	Acoustic Impedance (MRayl)
1:2.4 Epo-tek 301 and 2–3 μm silver powder	3.19 ± 0.04	1828 ± 11	~5.83
1:2.7 Epo-tek 301 and 2–3 μm silver powder	3.26 ± 0.01	1855 ± 13	~6.05
1:2.7 Epo-tek 301 and 3 μm alumina powder	2.26 ± 0.01	3270 ± 5	~7.39
1:2.5 Epo-tek 301 and 9 μm alumina powder (uncentrifuged)	2.21 ± 0.02	3254 ± 5	~7.19
Epo-tek 301	1.09 ± 0.01	2610 ± 4	~2.84

*Ratios are specified as weight ratios.

3.3.2 Piezoelectric material properties

Piezoelectric properties were quantified using an impedance analyser (E4990A, Keysight, California, USA) equipped with a test fixture (16034E, Keysight, California, USA) suitable for bulk samples, including plates, discs, and rings. The electrical response was recorded in impedance magnitude / phase (Z-θ) mode over a frequency range of 5 MHz to 30 MHz. k_t was calculated using Equation 2.5.

$\varepsilon_{33}^S/\varepsilon_0$ can be calculated using the parallel capacitance and dissipation factor (C_p-D) mode at a frequency of $2f_a$ based on the following equation [75]:

$$\frac{\varepsilon_{33}^S}{\varepsilon_0} = \frac{C_{33}^S\, t}{\varepsilon_0 A} \qquad \text{Eq. 3.2}$$

where A is the area and t is the thickness of piezoelectric material. ε_0 is the vacuum permittivity which is 8.85×10^{-12} F/m.

The speed of sound (c) in the material can be calculated based on the thickness and the resonance frequency using the following equation:

$$c = 2f_a t \qquad \text{Eq. 3.3}$$

The piezoelectric constant d_{33} was measured by a quasi-static Berlincourt meter (ZJ-6B, Tianjin Yingnaishi Technology co., LTD, Tianjin, China).

3.4 Fabrication of ultrasound transducer

This section describes the equipment utilised in transducer fabrication and the manufacturing workflows for both single-element 1-3 composite transducers and 64-element 1D linear arrays. Emphasis is placed on the specific engineering solutions developed to overcome high-frequency fabrication challenges, such as the precision dicing of fragile single crystals as well as the success of the optimised techniques like 'epoxy-framing' and multi-stage dicing.

3.4.1 Single-element transducer fabrication

3.4.1.1 Material preparation

Hand lapping

The aim of lapping is to control the thickness of piezoelectric materials, composites and passive layers including matching and backing layers. Following lapping, surface polishing is crucial for applying electrodes as the adhesion will increase with finer polishing. Controlling layer thickness is important to the final performance of transducers as many parameters are dependent on layer thickness including the electrical and mechanical resonance frequencies, the damping of the transducer, imaging resolution and efficiency [37]. A common method to decrease the thickness of a layer is to use a lapping machine [19], [123]. With this technique, samples are attached and detached to a glass plate several times. As the thicknesses of the active layer and matching layers for high-frequency transducers are extremely small, within 100 μm, the samples can be damaged easily during these processes [37]. Therefore, a hand lapping method, avoiding repeated attachment and detachment, was used for the work in this study.

Each layer of the US transducer is either mounted or cast directly on a small 4.5 cm^2 area glass plate. Figure 3.2 shows the set-up for hand lapping, with a flat granite block used as the substrate for the whole lapping procedure.

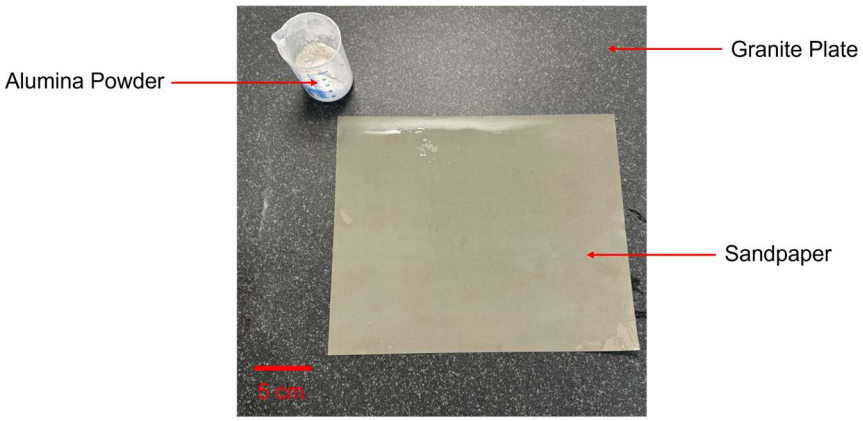

Figure 3.2 Set-up for hand lapping.

Initially, the glass plate was thoroughly cleaned with either ethanol or isopropyl alcohol (IPA). The plate was then placed on a hot plate and heated to 65°C. Quartz wax (Logitech, Glasgow, UK) was subsequently applied to the heated glass surface and allowed to melt. The sample was then positioned onto the molten wax. To prevent sample fracture during clamping, a rubber plate was placed over the sample to act as a cushioning buffer. Finally, the entire assembly was clamped securely by a customised fixture and allowed to cool to room temperature, fixing the sample to the glass plate. To reduce accelerated lapping at the sample periphery and enhance overall uniformity, four sacrificial alumina substrates were mounted to the four corners of the glass plate using cyanoacrylate adhesive (super glue). These substrates were subsequently lapped simultaneously with the sample. Figure 3.3 illustrates the fixture during the cooling process, alongside a view of the completed assembly showing the sample mounted onto the centre of the glass plate.

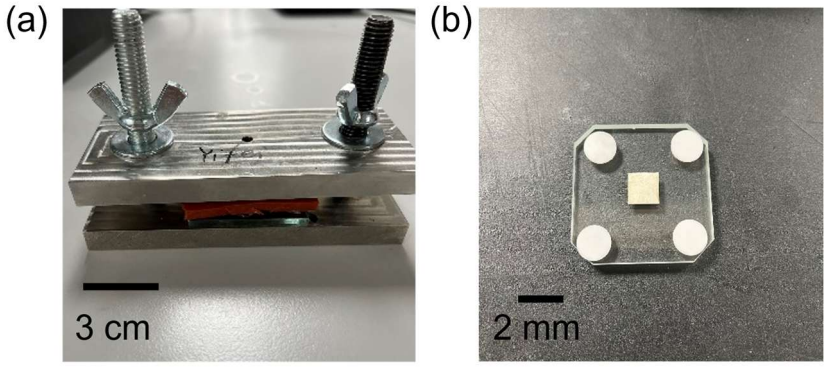

Figure 3.3 (a) The fixture and (b) the sample mounted on the glass plate.

Sandpapers with different grits were used gradually (Figure 3.4). For initial coarse lapping, 1000-grit sandpaper was utilised. The sample thickness was monitored periodically throughout this process using a contact measurement gauge (CG10,

Logitech, Glasgow, UK). When the thickness reached 50 µm above the final designed value, the abrasive was changed to 3000-grit sandpaper. For the final 10 µm of material removal, 5000-grit sandpaper was employed. Finally, a polyurethane polishing plate (Logitech, Glasgow, UK) was used in conjunction with a colloidal silica suspension (Struers ApS, Ballerup, Denmark), particle diameter 0.05 µm, for the final polishing step. The entire process was controlled to ensure the final sample thickness was within ±3 µm of the simulated target thickness.

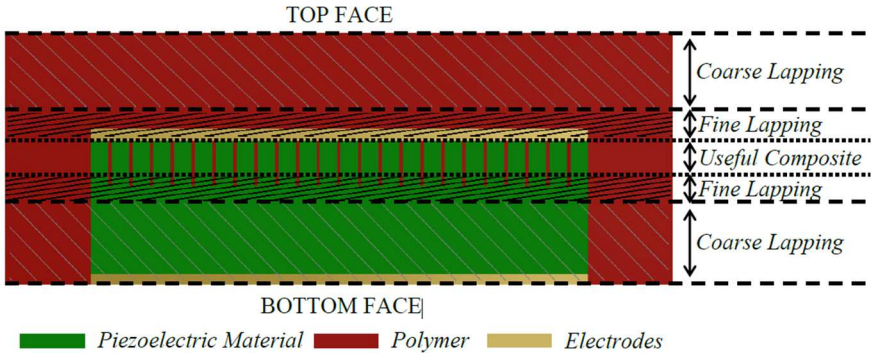

Figure 3.4 Schematic of lapping stages of a 1-3 composite sample [123].

Precision dicing

Precision dicing is utilised to realise the exact lateral dimensions of transducer stacks, to implement the dice-and-fill method for piezocomposite fabrication [75] and to create kerfs for array fabrication. Shown in Figure 3.5, a DAD3350 (DISCO, Tokyo, Japan) dicing saw consisted of a dicing unit and a cooling unit. The cooling unit supplies 21°C DI water, which serves the dual purpose of cooling the sample and blade and flushing away debris generated during the dicing process. The dicing unit is equipped with a porous ceramic vacuum chuck table that secures the sample and adhesive film to ensure a precise cutting height.

Figure 3.5 The view of the Disco dicing saw.

The operational procedure involves several preparatory steps. First, the cooling unit's water level must be verified to ensure an adequate supply for the duration of the process. The appropriate blade is then selected, mounted onto the holder, and subsequently calibrated to inspect for any potential damage. Following calibration, the required processing parameters are defined in the recipe interface. An initial cut is performed to establish the hairline alignment of the blade. As the positioning of this first cut can be imprecise, it is preferentially performed on a sacrificial sample. Once the hairline alignment is set, the dicing saw executes the automated dicing process according to the parameters defined in the recipe until the operation is complete.

For different designs and applications, various specifications of blades were used. Two key factors matter: one is the thickness of the blade which decides the kerf width and the other is the depth of the blade cut which is the so-called exposure. In this chapter, the blade most frequently employed was the finest available from Disco, with a kerf of 13 μm and an exposure of 430 μm. This blade was essential for the fine-pitch dicing required in the composite stack and array fabrication. Thicker blades (e.g., 96 μm thickness and 1750 μm exposure) were typically utilised for sectioning larger plates into smaller specimens.

Electrode deposition

During lapping, the electrodes on the piezoelectric material are removed, therefore new layers of electrodes need to be applied on the major surfaces. The most important consideration is the compatibility between the electrode metal and the piezoelectric material. In this work, titanium (Ti) was selected to be used as the adhesion layer and gold (Au) as the conductive layer. [124]. Figure 3.6 shows a MEB 550S (Plassys, Marolles-en-Hurepoix, France) electron beam evaporator used for metal deposition in the James Watt Nanofabrication Centre. Prior to deposition, the samples were carefully mounted on a 6-inch holder. The load chamber was then evacuated to a base pressure of 1×10^{-6} mbar to minimise contamination and oxidation during the process. Conductive layers of Ti and Au were subsequently deposited onto the sample surfaces, with final thicknesses of 20 nm and 150 nm, respectively. The deposition rates, selected via the system's control panel, were 0.3 nm/s for Ti and 0.5 nm/s for Au. These rates were adopted from the user manual to ensure optimal film quality and adhesion.

Figure 3.6 The Plassys MEB 550s e-beam evaporator.

3.4.1.2 Single-element bulk acoustic stack fabrication

The fabrication of a single-element transducer is a multi-step procedure, where each stage demands meticulous execution. A schematic representation of the single-element transducer stack fabrication process is presented in Table 3.2:

Table 3.2 Fabrication process for single-element transducer stack.

Process steps	**Diagram**
a. The glass carrier plate and the sample are thoroughly cleaned using acetone followed by IPA. Prior to mounting, the thickness of the sample is measured at five distinct points (the four corners and the centre) using a micrometre to establish a baseline, and the values are recorded. Additionally, the thickness variation of the glass plate itself is quantified to ensure uniformity.	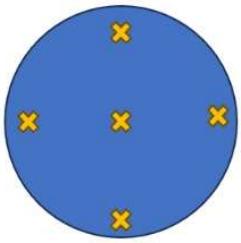
b. The active material is mounted onto a glass carrier plate using either low-temperature (65°C) or high-temperature (100°C) mounting wax. The assembly is then placed into a compaction fixture. To ensure even compression and prevent the wax from adhering to the tools, a wax paper barrier and a rubber pad are placed atop the sample. The assembly is then compressed and allowed to cool to ambient temperature.	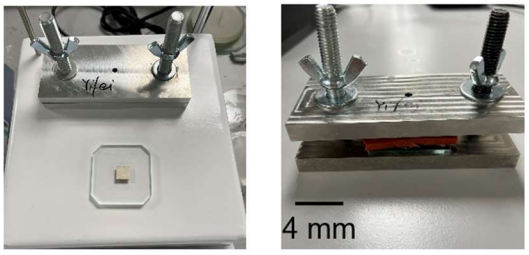

Process steps	Diagram
c. Four spacers which are made of alumina are placed at the corners for reference and for controlling the hand lapping speed. Use sandpaper to lap the sample down to the thickness wanted. Use from 1000 to 5000 grits wet sandpapers and alumina powder to lap the sample. Measure the thickness with the contact measurement gauge from time to time, ensuring the thickness variation is within 3 µm. Use the contact measurement gauge to measure the final thickness of the sample and with the glass plate.	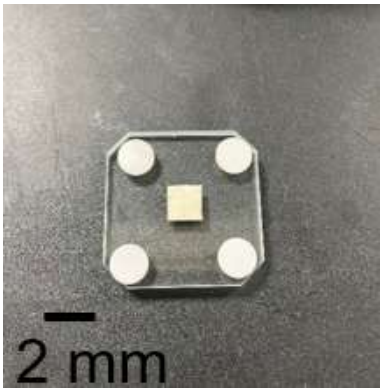
d. Prior to metallisation, the specimen is thoroughly cleaned using acetone, followed by IPA. Polyimide tape is utilised to mask the glass plate, leaving only the top surface of the piezoelectric sample exposed for deposition. The electrode metal is then deposited onto the exposed surface. Finally, the polyimide tape is carefully removed.	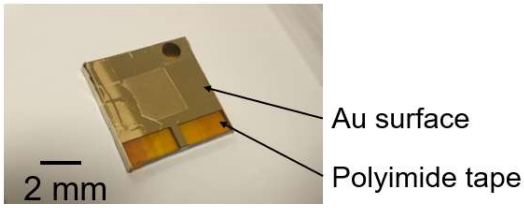
e. A containment dam is constructed around the sample using gypsum bars. The resulting gaps, both between the gypsum bars and between the dam and the glass plate, are sealed using a rapid two-part epoxy compound.	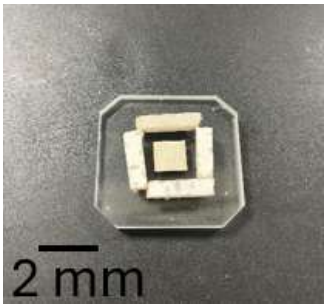
f. Epo-tek 301 epoxy is first degassed for 15 minutes. Subsequently, the degassed epoxy is combined with 3 µm silver powder at a specific weight ratio. The mixture is prepared in a weighing boat and stirred for 5 minutes to ensure homogeneity.	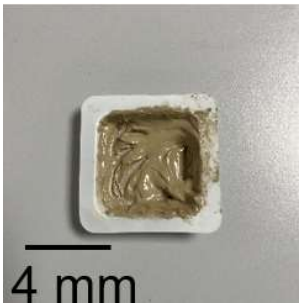

Process steps	Diagram
g. Prior to filling, the surface of the specimen is treated with an AP131 adhesion promoter. This promoter is applied to enhance adhesion between the matching layer and the electrode surface. The prepared silver epoxy mixture is then carefully deposited into the prefabricated dam using a stirring rod. The dam is subsequently sealed using polyimide tape, preparing the sample for centrifugation.	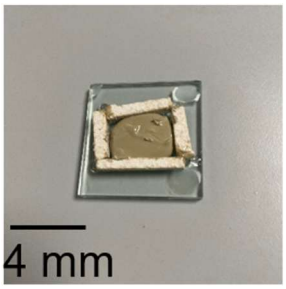 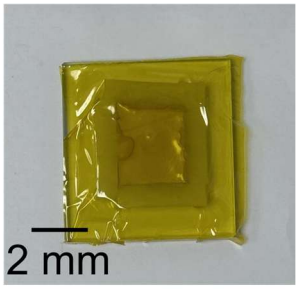
h. The sample is centrifuged at 3,000 revolutions per minute (rpm) for 15 minutes [85]. Subsequently, the sample is cured following the standard protocol: either in a heated oven per the datasheet specifications or ambient temperature curing overnight. Then the matching layer is lapped to the designed thickness.	
i. The transducer stack, complete with the applied matching layer, is diced out using the dicing saw. The diced stack is then carefully flipped and mounted on a new glass plate. The procedure for applying the backing layer is subsequently repeated on the newly exposed side. This includes centrifuging and curing the backing material. Finally, the completed assembly is lapped down to its final designed thickness.	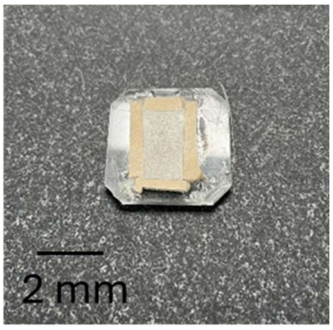
j. Reference lines are inscribed on the back of the glass to aid dicing alignment. The assembly is then covered with transparent polyimide tape. The samples are subsequently diced into their final specified dimensions.	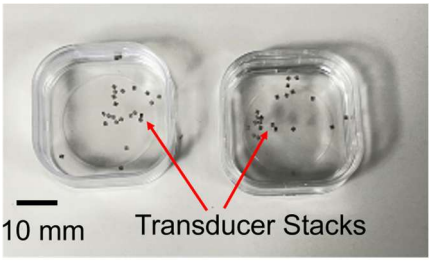

3.4.1.3 1-3 Composite Fabrication

For 1-3 composite transducer fabrication, the 1-3 composites were fabricated using a conventional dice-and-fill method [125], [126]. Figure 3.7 shows a schematic of dice-and-fill method process.

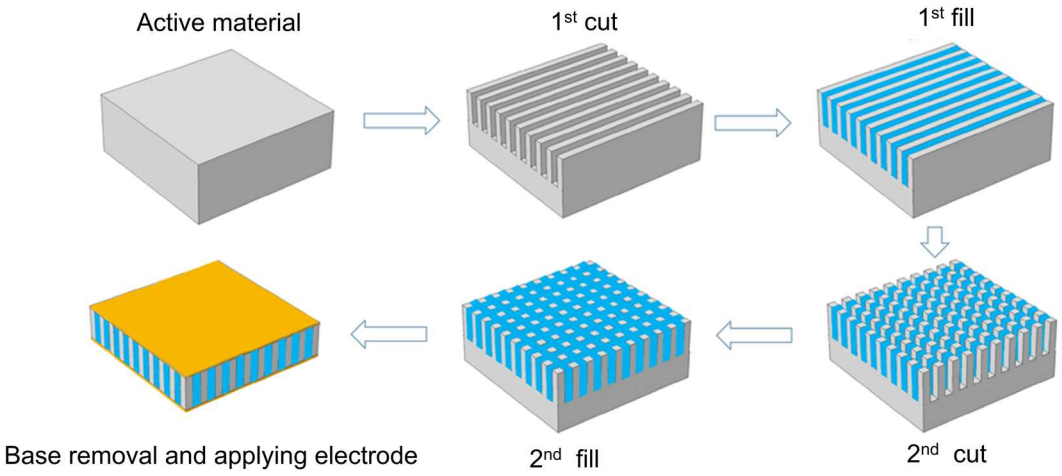

Figure 3.7 Process of dice-and-fill method.

To maximise the pillar AR, thereby achieving an optimal pulse shape, a 13 µm kerf dicing blade (Disco Corp, Tokyo, Japan) and a 50 µm cutting pitch were selected [77], as described in Chapter 2. For 18 MHz transducer stack fabrication, a target AR of 2 and a composite VF of 55% were chosen for both the PIN-PMN-PT single crystal and the Sm-doped PIN-PMN-PT single crystal (TRS Technologies, PA, USA) used in Chapter 4. Due to the limited availability of the Sm-doped PIN-PMN-PT single crystal, all dicing tests and process parameter optimisation were conducted using the standard PIN-PMN-PT single crystal material.

A significant fabrication challenge arises from the inherently fragile and brittle nature of these single crystals [65], [127]. This results in low yields during conventional dice-and-fill fabrication, as illustrated in Figure 3.8. Mechanical blade friction and hydrodynamic forces from the cooling water jet directly fracture the piezoelectric pillars.

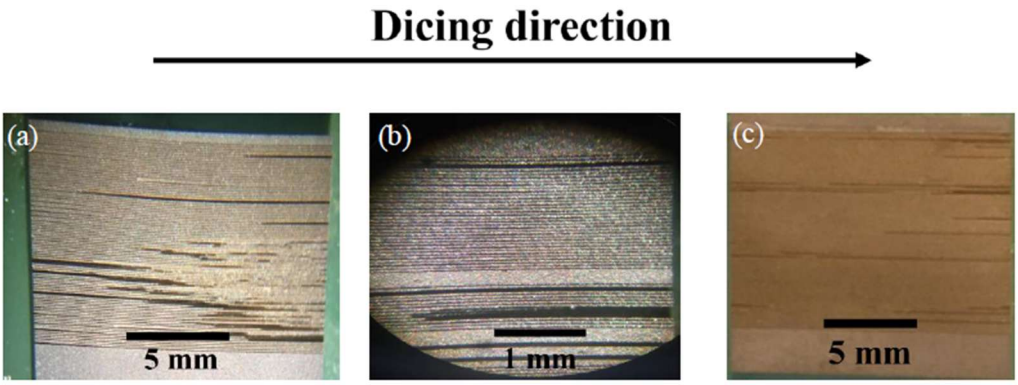

Figure 3.8 Examples of collapsed planks in 1-3 composite fabrication diced at (a) 36 µm, (b) 37 µm and (c) 38 µm [19].

Optimised dicing protocols were established to maximise pillar integrity. Previously, through extensive testing, McPhillips determined the optimal single-crystal dicing parameters to be a feed speed of 0.2 mm/s and a spindle speed of 12,000 rpm [37]. Later, Moldovan introduced a multi-stage cutting technique to mitigate mechanical stress. This method utilised a two-pass, step-down cutting process for each kerf. The initial pass was performed at half the final protrusion depth. A second pass was then conducted along the same path at the full protrusion depth. This approach was implemented specifically to minimise the mechanical stress exerted on the material during dicing [123]. The adoption of these optimised process parameters and cutting strategies enabled fabrication yields approaching 100% pillar integrity. Another reported strategy is the "double-pitch dicing" method [19]. This technique involves an initial dicing pass at twice the final pitch, filling the kerfs with epoxy, and then performing a second dicing pass to bisect the epoxy-filled slices. The dicing parameters for these three protocols are summarised in Table 3.3.

To circumvent this limitation, researchers have explored alternative methods such as laser micromachining and deep reactive-ion etching (DRIE) to achieve higher AR and improve fabrication yields [100], [128]. While these methods improve pillar stability, they are substantially more time-consuming, often doubling or even tripling the total processing time compared to a standard dice-and-fill procedure.

Whing dicing the piezoelectric materials, structural failure occurs mainly during the 1st cutting direction. These fractures concentrate at the terminal edges of the individual planks. The subsequent epoxy kerf filling process increases structural strength prior to

the 2nd orthogonal cut. This reinforced architecture prevents further pillar collapse during the 2nd cut.

During dicing, plank collapse is hypothesised to be a consequence of the blade's clockwise rotation. At the completion of each pass, as the rotating blade exits the sample, vibrations in the blade assembly may cause transient misalignments. This can lead to abruptly increased frictional forces or even momentary collisions between the blade and the newly cut sample edge. It is proposed that the material, which is under maximum mechanical stress at this exit point, is thereby induced to fracture. Piezoelectric single crystals were used in this thesis, which exhibit physical fragility compared to standard piezoelectric ceramics. This inherent material weakness leads to worse plank collapse during the dicing. To resolve this issue, an "epoxy-framing" technique was implemented. Prior to dicing, the single crystal sample was encapsulated within a surrounding epoxy frame, which was subsequently cured, as shown in Figure 3.9 (a). The epoxy frame prevents damage primarily by providing mechanical support to the fragile planks and pillars during dicing. The cured epoxy extends the cutting path beyond the single crystal boundary, allowing the blade to pass from the crystal into epoxy smoothly rather than directly into a free edge to prevent local bending and fracture. Figure 3.9 (b) shows the boundary between the epoxy frame and the single crystal during the dicing. All planks are observed to be structurally intact and free of fractures after dicing.

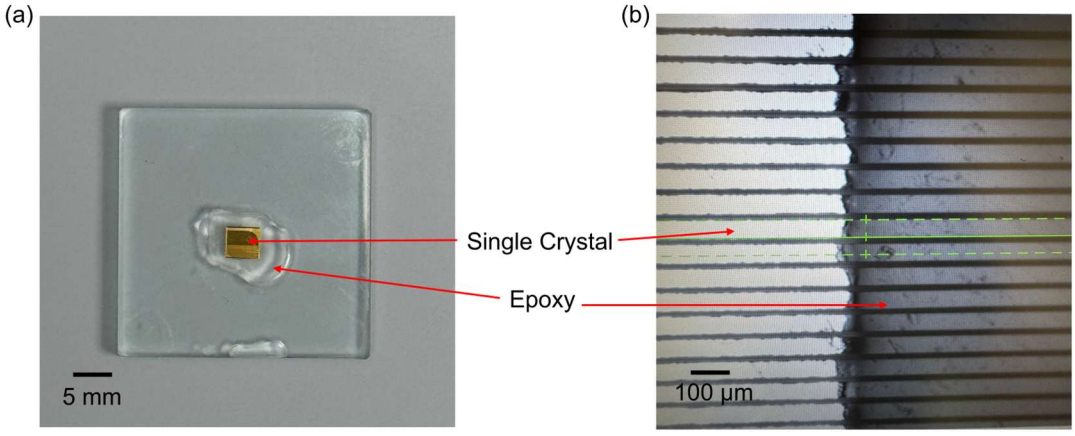

Figure 3.9 (a) Photo of epoxy frame surrounding single crystal sample and (b) View of boundary between single crystal and epoxy.

The cured epoxy frame functions as a sacrificial run-out region contiguous with the sample. As the dicing blade completes its pass and exits the crystal, this epoxy border

provides a stable mechanical transition. This physical extension mitigates the transient misalignments and impact forces previously identified at the material boundary, significantly improving pillar integrity. This strategy avoids the substantial time penalty associated with the "double-pitch" technique. The total processing time for this epoxy-framed approach remains the same as that of a conventional dice-and-fill procedure.

Table 3.3 summarises the diverse techniques and dicing parameters evaluated across previous literature and the current study. Methods 1 and 3 share identical pitch with this research while utilising excessively low feed speeds that significantly extend total dicing duration. Method 3 incorporates an additional "double pitch" technique that physically doubles the overall fabrication time. Method 2 employs a repetitive two pass step down cutting procedure that prolongs total manufacturing time. As detailed in the table, the proposed method achieves the maximum feed rate and highest overall fabrication efficiency. The cutting depth in this study is shallower than Method 1 while remaining sufficient for high-frequency transducer fabrication.

Table 3.3 Dicing parameters for 1-3 composite in single crystal materials.

Method	Method 1 [37]	Method 2 [123]	Method 3 [19]	Method 4 (This study)
Blade Kerf (μm)	13	28.5	13	13
Cut Depth (μm)	250	N/A	130	120
Pitch (μm)	50	250	76	50
No. of Cuts	2	4	4	2
No. of Fills	2	2	4	2
Feed Rate (mm/s)	0.12	0.12	0.10	0.50
Spindle Speed (rpm)	12000	12000	20000	20000

For 1-3 composite stack fabrication, the single crystals were diced in one direction with a depth of 120 μm. Epo-tek 301 was subsequently employed to fill the kerfs. The same procedure was applied for the second direction of cuts. The extra epoxy was

removed, and conductive Ti/Au layers (20 nm/150 nm) were deposited onto the top surface. Then the stack was flipped and lapped to the design thickness, $t = 70$ µm. Conductive layers were deposited onto the bottom surface. Figure 3.10 (a-c) show top views of 1-3 composite. The backing layer was subsequently applied, following the procedure detailed in Table 3.2. Figure 3.10 (d) shows a front view of a stack under scanning electron microscopy (SEM). Given that the acoustic impedance of the composite is approximately 16.5 MRayl, a single layer of Parylene C was selected to function as both the sole acoustic matching layer and a protective, waterproof coating.

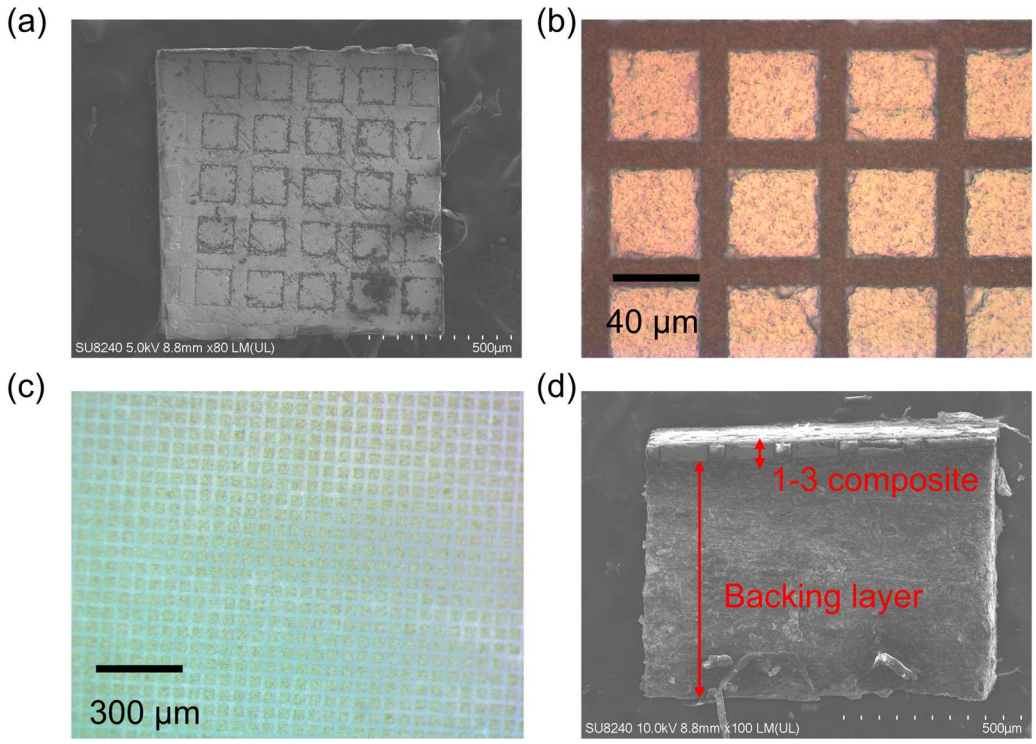

Figure 3.10 Top surface of 1-3 composite under (a) SEM and (b–c) microscope and (d) front view of a stack under SEM.

3.4.1.3 Single-element transducer fabrication

Wiring and housing

After preparation of the acoustic stacks, the transducers are assembled by electrical wiring followed by integration into the housing. In this section, different strategies of wiring and housing methods are discussed. For integration with an MSCR, it is necessary to keep the weight of the whole transducer as small as possible to minimise influence on the movement of the MSCR. A study has been conducted that the MSCR can take a payload of at least ~3 g [69]. For miniature US transducer fabrication, a metal housing is commonly used as that is conductive for ground connection and rigid

for protection [62], [129], [130]. However, the density of the metals is normally much larger than plastic or epoxy. To minimise the influence on the movement of a MSCR and the dexterity imparted by its soft nature, a modification of the housing strategy was used here. A schematic for the cross section of a normal metal housing transducer configuration and one for modified configuration for MSCR are shown in Figure 3.11.

The key difference between the conventional and modified housings is the location of the ground electrode. In both configurations, the core of the coaxial cable is connected to the conductive backing layer using conductive silver epoxy. With the metal housing, an extra conductive Ti/Au layer is applied to the conductive matching layer and the top surface of the housing. Consequently, the ground connection is linked with the mesh of the coaxial cable through the metal housing.

In the modified configuration, the electrical connection cannot be linked with the front side of the piezoelectric material directly because a polyimide tube with thin wall thickness is used for the inner housing. In the same way as the conventional method, Ti/Au conductive layers are applied to the front surface of the matching layer and the polyimide tube. Importantly, silver epoxy is used to extend the top electrode to the outside of the inner polyimide tube. The mesh of the coaxial cable is connected to the silver epoxy on the wall. Another polyimide tube with a larger diameter is chosen to be an outer housing, and the space between the inner and outer polyimide tubes is filled with Epo-tek 301 for protection. Without a metal housing, this modified structural strategy makes the whole transducer lighter. The other ends of the coaxial cable are connected to the core and the wall of a SMA connector for electrical transmission. A process diagram (Table 3.4) of the modified housing illustrates the operations required during the wiring and housing procedure.

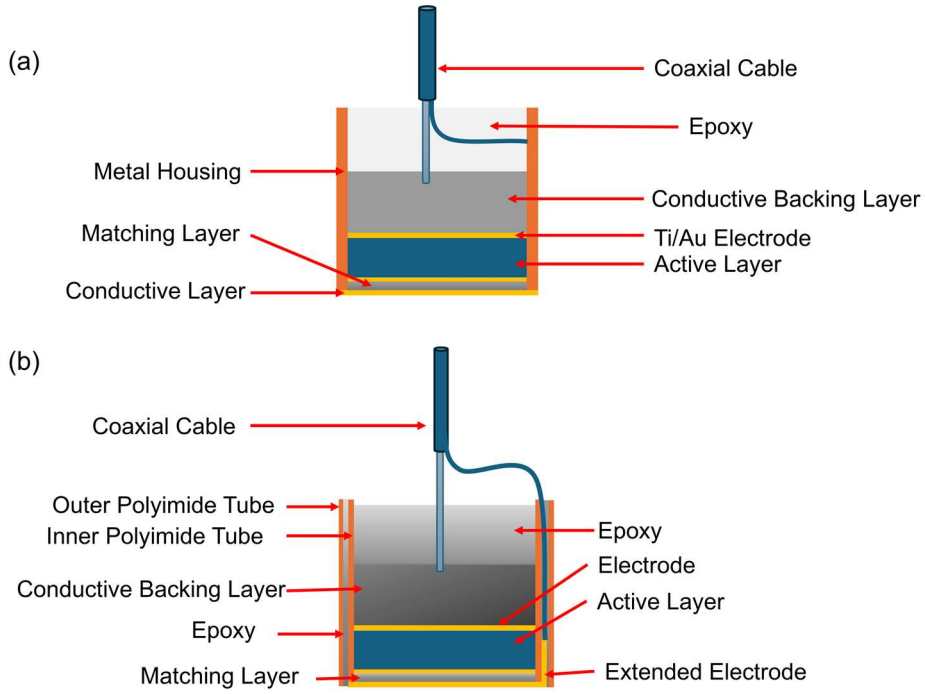

Figure 3.11 (a) Schematic of normal metal housing and (b) modified housing for MSCRs.

Table 3.4 Fabrication process diagram for wiring and housing strategy.

Process steps	Diagram
a. The outer insulation of the micro coaxial cable is mechanically stripped from both the transducer and SMA connector ends using a precision blade. Under microscopic observation, the inner core conductor is meticulously separated from the outer shielding braid, which is subsequently twisted into a consolidated strand. Finally, the electrical conductivity of both the core and the shield are verified using a multimeter.	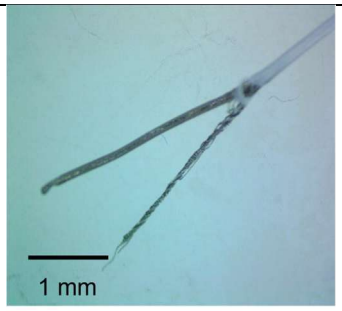
b. A sheet of double-sided tape is applied to a circular glass plate. A single transducer stack is then positioned onto the tape, ensuring that the matching layer faces the adhesive surface. Finally, a rubber pad is utilised to carefully compress the entire assembly, guaranteeing sufficient adhesion between the stack and the glass plate.	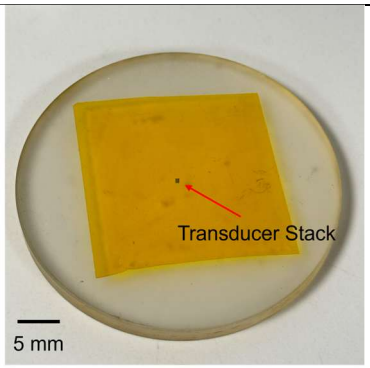

Process steps	Diagram
c. The core conductor of the coaxial cable is electrically terminated to the back electrode of the transducer stack using E-solder 3022 silver epoxy (Von Roll, USA). Following the curing of the silver epoxy, the transducer stack is encased within a polyimide tube. The resultant void, encompassing the electrical connection point, is subsequently filled with a protective epoxy compound to ensure mechanical integrity and insulation.	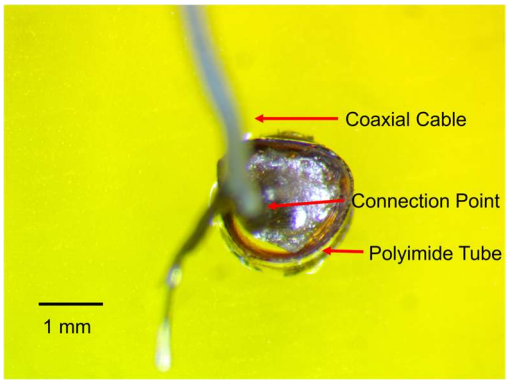
d. Ti/Au electrode layers are deposited onto the front surface of the transducer. Utilising E-solder 3022 conductive silver epoxy, the ground connection (from the coaxial shield) is extended to the outer side of the polyimide tube under microscopic observation.	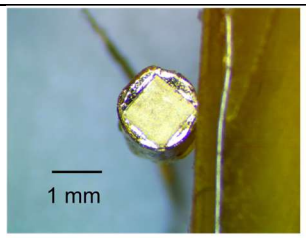 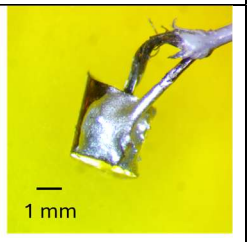
e. The final transducer assembly is enclosed within a larger polyimide tube, and the resulting void is subsequently filled with an epoxy compound to provide robust mechanical integration and protection. Prior to the final coating, the surface of the stack is treated with an A174 adhesion promoter (Merck Group, Darmstadt, Germany). Finally, a Parylene C coating is deposited to a specific thickness over the entire transducer, serving as both the second acoustic matching layer and a biocompatible waterproof barrier.	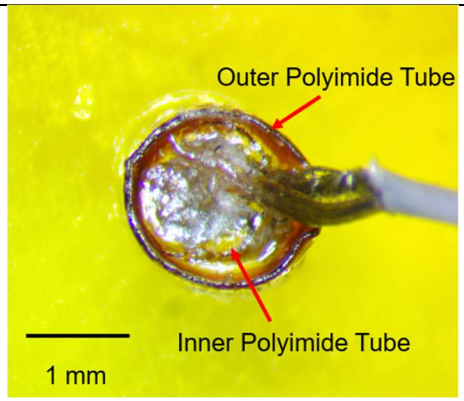

Electrical connectivity

The fabrication of the transducer is an intricate, multi-stage process that demands rigorous manual precision, particularly during the electrode deposition and wiring phases. Therefore, an electrical connectivity check becomes necessary to determine connectivity information after each step. Particularly, after steps a, c, d, e in Table 3.4 either the connectivity between two points on the surface or the connectivity between surface and wires should be checked by a digital multimeter.

Parylene coating

Parylene C is an FDA (U.S. Food and Drug Administration) approved polymer that exhibits a desirable combination of properties, including excellent chemical inertness, high biocompatibility, superior mechanical flexibility, and high thermal stability. Owing to these attributes, it has been widely adopted for numerous biomedical applications [131]. Parylene C forms a uniform pinhole free layer that researchers have utilised as a matching and water proof layer in US transducer development for years [1], [132], [133].

In this study, a PDS 2010 Labcoter (Specialty Coating System, Indianapolis, USA), Figure 3.12 (a), was used to generate a Parylene C film on US transducer stacks. The chemical vapour deposition process for Parylene C proceeds in three distinct stages: vaporisation, pyrolysis, and deposition. Initially, the solid dimer precursor was loaded into the vaporiser and heated to ~200 °C, causing it to sublime directly into a gas. This dimer vapour is then transferred to the pyrolysis furnace, where it was subjected to a temperature of ~680–700 °C. This high temperature cleaves the dimer, transforming it into a reactive monomer gas. Finally, this monomer is introduced into the deposition chamber at ambient temperature, where it spontaneously polymerises onto all exposed substrate surfaces, forming a uniform, transparent, and highly conformal film. Figure 3.12 (b) illustrates the coating process within the Parylene coating chamber.

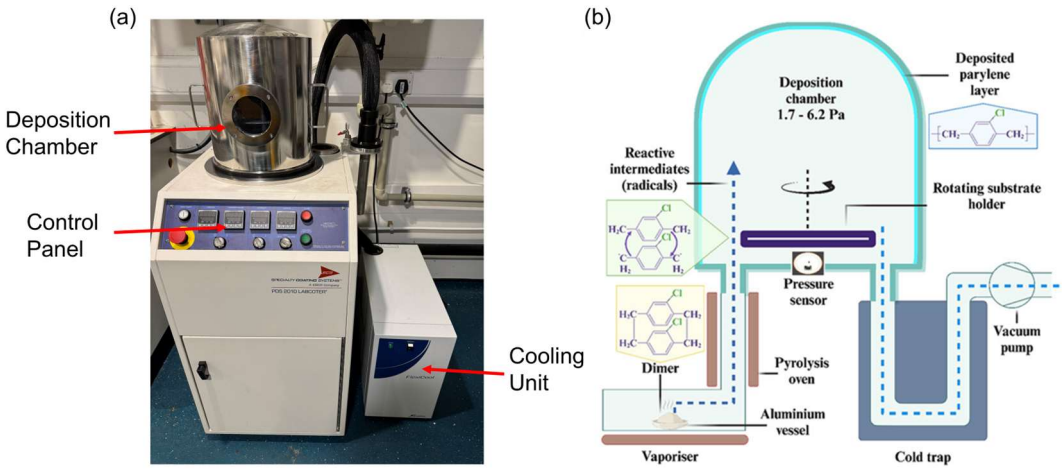

Figure 3.12 (a) Photo of Parylene coater and (b) schematic of the process within the Parylene coater [134]. (Modified with permission)

The thickness of the Parylene C layer is a critical parameter in ultrasonic transducer fabrication, necessitating a precise characterisation of the relationship between the

initial dimer mass and the final deposited thickness. To establish this calibration, a series of deposition runs was performed using varying initial masses of the dimer precursor. For each run, Parylene C was deposited onto glass slides, and the resulting film thickness was measured using DektakXT stylus surface profiler (Bruker Corporation, Tucson, USA). Figure 3.13 plots the mean resulting Parylene C film thickness as a function of the initial dimer mass. The relationship is shown to be highly linear, as confirmed by a linear regression analysis which yielded a coefficient of determination (R^2) of 0.9983. The regression equation is:

$$y = 0.4725x + 0.523 \qquad \text{Eq. 3.4}$$

with a standard error of 0.0238. x is the weight of the dimer and y is the thickness of the expected Parylene C layer.

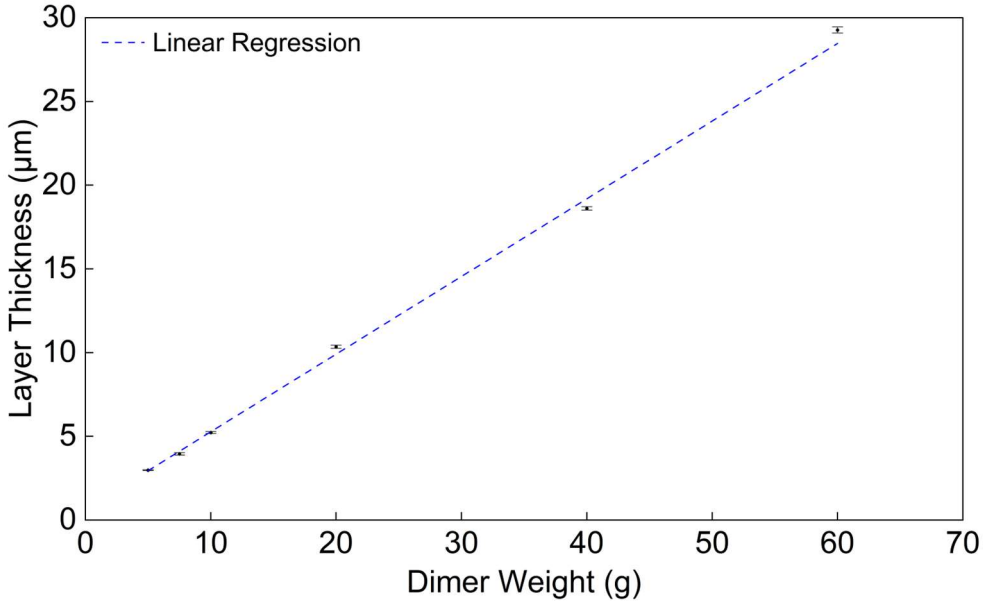

Figure 3.13 Relationship between Parylene C film thickness and dimer weight.

3.4.2 1D linear array transducer fabrication

3.4.2.1 Design consideration

In ultrasonic phased array imaging, the suppression of grating lobes typically requires the element pitch to be less than one wavelength [135], [136]. However, in high-frequency fabrication, strictly adhering to this criterion is challenging due to the resolution limits of dicing equipment and flexible circuit manufacturers. Consequently, a design trade-off regarding the pitch is often necessary.

Beyond the pitch, the geometry of the individual piezoelectric pillars is critical for spectral purity. In a linear array design, the primary objective is to isolate the thickness vibrational mode; however, lateral modes can couple with and distort this desired thickness mode if the element geometry is not optimised. Therefore, to suppress these unwanted modes, the AR of the elements in a 2-2 composite must adhere to specific design guidelines [137]:

$$w \leq \frac{c_l}{4f_c} \qquad \text{Eq. 3.5}$$

where w is the element width, c_l is the longitudinal wave velocity in the piezoelectric material and f_c is the centre frequency of the array element.

For this study, a high-frequency array was designed with f_c = 15 MHz and 64 elements. Based on the measured longitudinal velocity of the material ($c_l \approx 4400$ m/s), the critical single crystal width required to eliminate unwanted modes was calculated to be $w \leq 73.3$ µm. To accommodate the fabrication limits of the flexible circuit, a pitch of 100 µm was selected, with electrical connections bifurcated into odd and even groups to relax the circuit pitch to 200 µm.

To satisfy the element width criterion ($w \leq 73.3$ µm) within these 100 µm pitches, a sub-dicing strategy was employed. A dicing blade (ZHZZ AZ series, DISCO, Tokyo, Japan) with a kerf of 12 µm was used to perform a cut with a depth of 120 µm at the centre of each element. This process yielded two key benefits: it ensured compliance with the design guideline (Equation 3.5) by reducing the effective sub-element width, and it reduced the width-to-thickness ratio to 0.38. This modification serves to maximise the AR, thereby increasing energy conversion efficiency and ultimately the SNR of the final image [138].

Flexible array circuit

The corresponding flexible circuit was designed using JLC Easy EDA (JLCPCB, Shenzhen, China) and fabricated by PCBWay (Shenzhen, China). Figure 3.14 (a) shows the flexible printed circuit board (fPCB) for the array. Several key considerations guided the circuit design. Firstly, to minimise crosstalk and internal-element interference, the lengths of the parallel traces were limited. A trace length of 12 mm in the flexible circuit was selected as a compromise, ensuring

sufficient reach to the connectors (Figure 3.14b) of the Verasonics research US system (Vantage 128, WA, USA). Secondly, the fPCB required transparency and minimal thickness to achieve precise alignment during bonding to the array elements. Consequently, a total thickness of 70 µm was chosen, and the design omitted an integrated reference ground plane, as the ground signal was carried instead by a separate conductive copper cable.

The interconnect was fabricated as a fPCB with copper traces 100 µm wide and 9 µm thick. These traces are encapsulated within a polyimide substrate. To enhance mechanical stability at the connection interface, the connector region is reinforced with a 0.2 mm thick FR4 stiffener. Furthermore, the contact pads are treated with an immersion gold finish with a thickness of 0.03 µm to ensure reliable electrical conductivity and oxidation resistance.

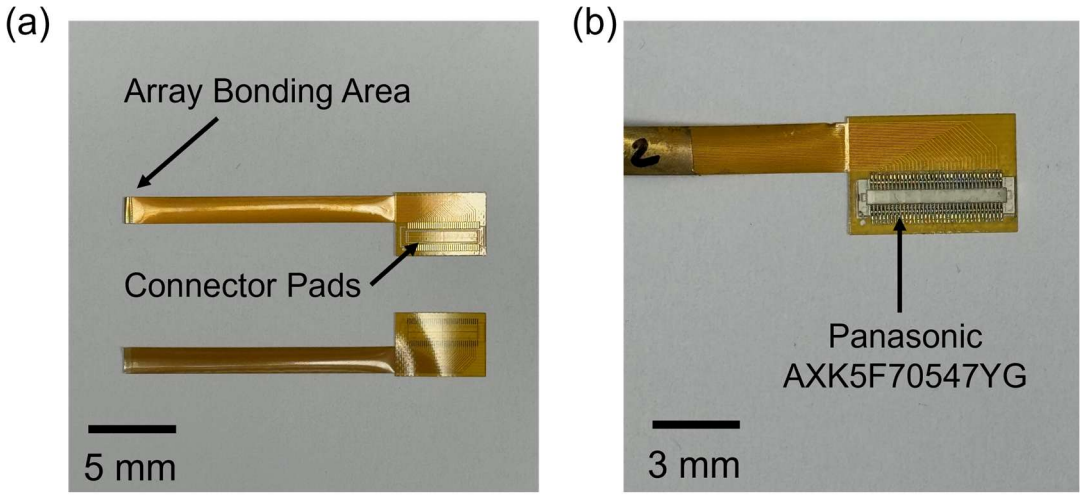

Figure 3.14 (a) Flexible PCBs for a 15 MHz array and (b) connectors to the control system.

3.4.2.2 Fabrication processes

The manufacturing of arrays follows a structured workflow. This section outlines the specific fabrication process, summarised in Table 3.5, detailing the characterisation protocols implemented during and after assembly, along with an analysis of the technical challenges encountered.

Table 3.5 Fabrication process for a1D linear array.

Process steps	Diagram
a. The piezoelectric sample is mounted onto a glass plate. Subsequently, the material is diced at the designed pitch, with an additional sub-dicing cut executed along the central axis of each element. The resulting kerfs are filled with Epo-tek 301 resin, and the assembly is degassed to ensure void-free encapsulation and cured overnight at room temperature.	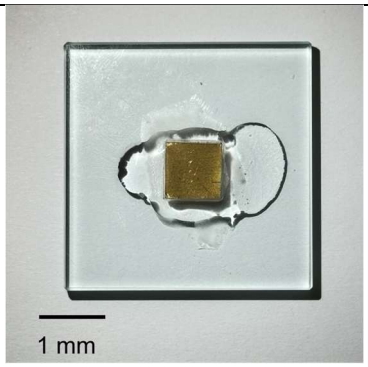
b. Any excess epoxy is initially removed through a lapping step. The sample is subsequently inverted and lapped to the specified design thickness. Following this, both surfaces are polished. Finally, Ti/Au layers are deposited on the surface.	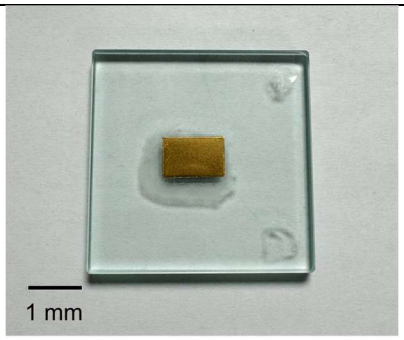
c. The assembly is diced at the designed pitch to mechanically separate and isolate the individual active elements.	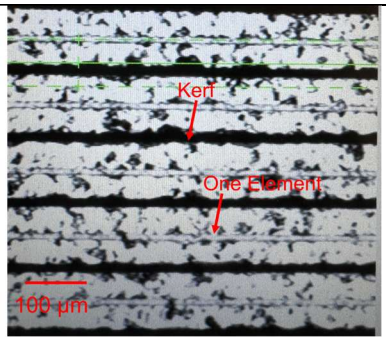
d. The transducer elements are precisely aligned with the corresponding conductive traces of the flexible circuit. A controlled quantity of Epo-tek 301 adhesive is applied to the interface, and the assembly is subsequently compressed utilising a dedicated bonding fixture. The assembly is maintained in an oven at 40 °C overnight.	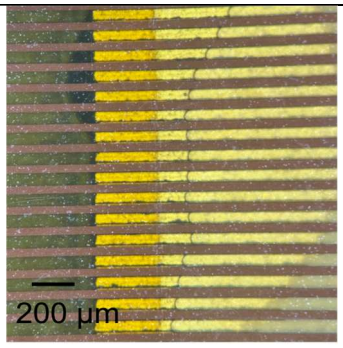

Process steps	Diagram
e. The ground cable is positioned between the transducer elements. Subsequently, E-solder 3022 conductive silver epoxy is utilised to securely bond the cable to the glass carrier plate.	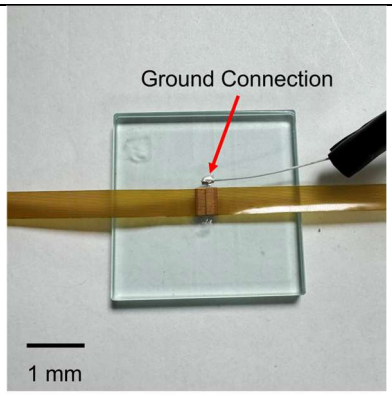
f. The flexible circuit and the ground cable are encapsulated together within a composite backing formulation, consisting of epoxy resin loaded with alumina powder. The assembly is subsequently placed in an oven and cured at 40 °C overnight.	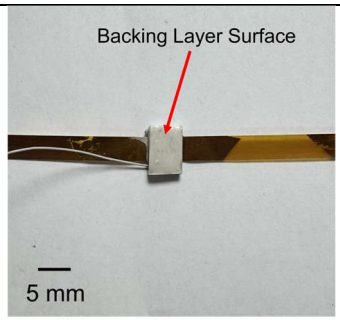
g. Following the metallisation of the opposing surface, the first matching layer is lapped to its specified thickness and bonded to the top surface of the array stack utilising Epo-tek 301. Finally, a Parylene C layer is deposited over the stack to function as the second acoustic matching and waterproof layer.	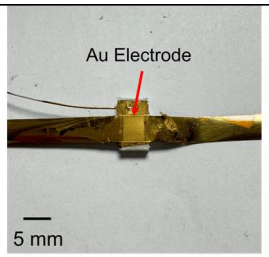 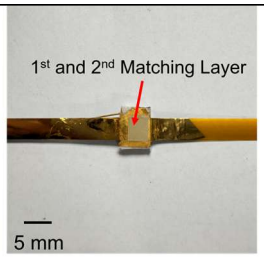

Electrical continuity

Prior to committing to final fabrication, the electrical viability of the pressure-contact method was validated. One flexible circuit was bonded with a sample plate with the same pitch. This initial validation test (Figure 3.15a) utilised a multimeter to confirm that the proposed clamping mechanism (Figure 3.15b) could establish a reliable conductive path between the flexible circuit and the array elements. This validation was critical, as the final assembly process, wherein the odd- and even-numbered flexible circuits are bonded to the array (Figure 3.15c), is irreversible. Consequently, following the complete, irreversible assembly, the functionality of each array element was verified using the impedance analyser. The presence of a characteristic impedance resonance was used as the criterion to confirm that the element was active and correctly connected.

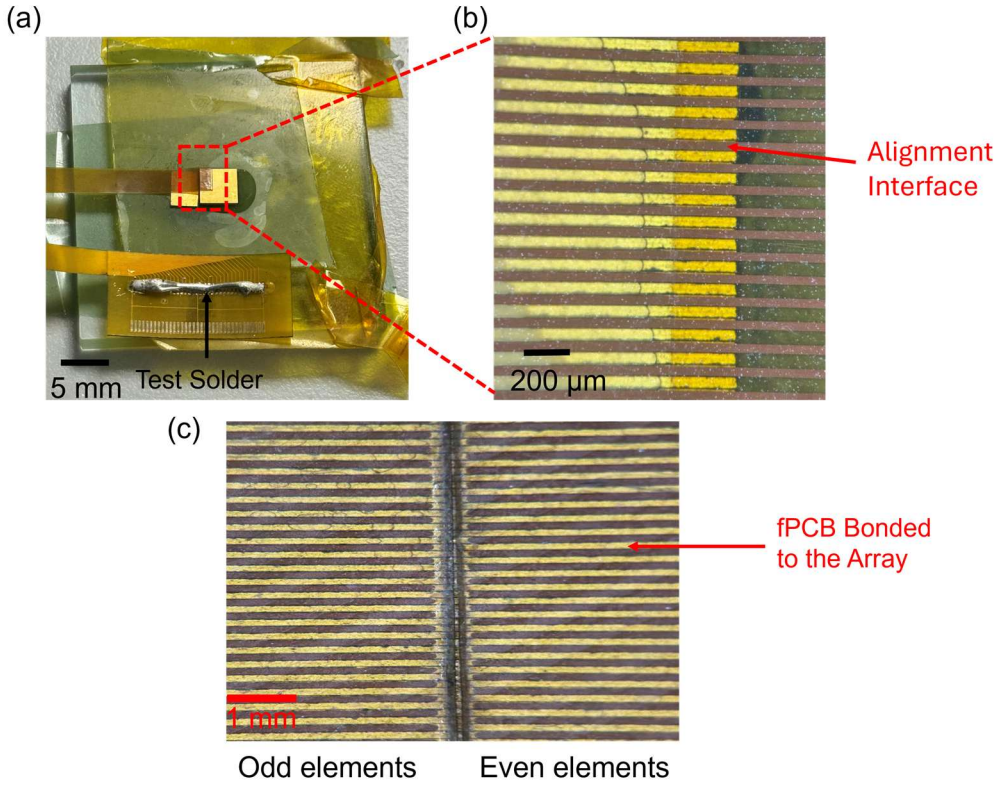

Figure 3.15 Conductivity test and fPCB integration of the array. (a) Configuration for electrical connection test, (b) magnified view of the elements showing precise alignment and (c) view of the top surface after complete integration with the fPCB.

Electrode delamination

As an active element is composed of two 38 µm wide sub-elements and a kerf, the top electrodes between each active element must be electrically isolated. A significant

fabrication challenge was encountered during the dicing stage: the delamination of these fine-featured electrodes, as illustrated in Figure 3.16. This failure was attributed to a combination of factors, including poor metal adhesion, potentially due to insufficient surface preparation after lapping and polishing.

To mitigate this delamination, a surface treatment step was introduced prior to metallisation. Plasma cleaning (YES-G1000, Yield Engineering System, Inc., CA, USA) was performed on both sides of the stack along with the glass plate to thoroughly clean the surfaces and improve the adhesion of the subsequent Ti/Au layers.

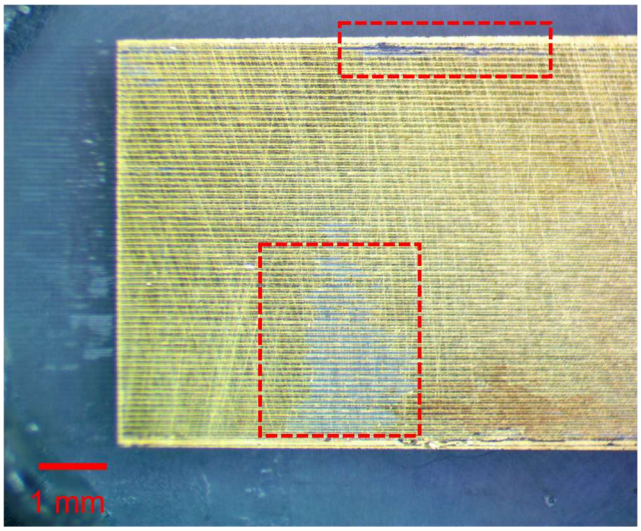

Figure 3.16 Delamination of electrode.

Capacitance measurement

To evaluate fabrication uniformity, the capacitance of each element in the array was measured at 1 kHz using the impedance analyser. This measurement also served as a rapid diagnostic tool for identifying fabrication failures. As illustrated in Figure 3.17, the *C* values for two elements were lower than those of the others. Subsequent pulse-echo testing confirmed that these two elements were non-functional. This failure is attributed to electrical disconnections that occurred during the integration of the fPCB with the array elements.

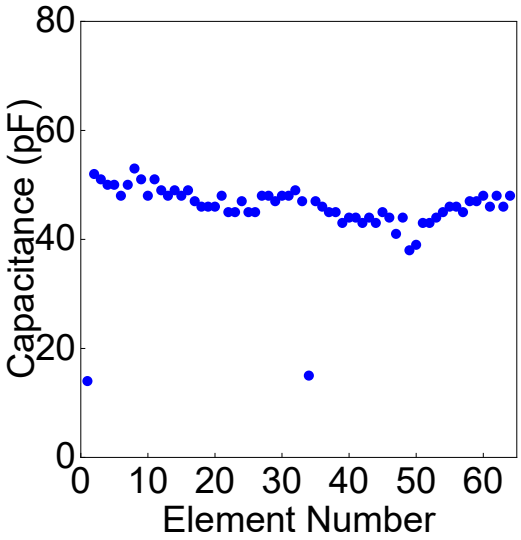

Figure 3.17 The capacitance of elements in a sample 64 element array.

3.5 Transducer characterisation

This section outlines the functional characterisation regime used to validate the fabricated devices. A suite of quantitative performance metrics is defined, ranging from electrical impedance spectroscopy and pulse-echo measurements to imaging-specific parameters, including spatial resolution, sensitivity, SNR, and inter-element crosstalk. The measured results of the transducers fabricated in this thesis are listed in Chapter 4 and 5.

3.5.1 Electrical impedance spectroscopy

The impedance magnitude / phase spectra of the single-element transducers, and 1D array transducers were measured by the E4990A impedance analyser with frequency from 5–30 MHz (Figure 3.18a). A commercial test fixture (16047E Keysight, California, USA) in Figure 3.18 (b) was installed for array element measurements.

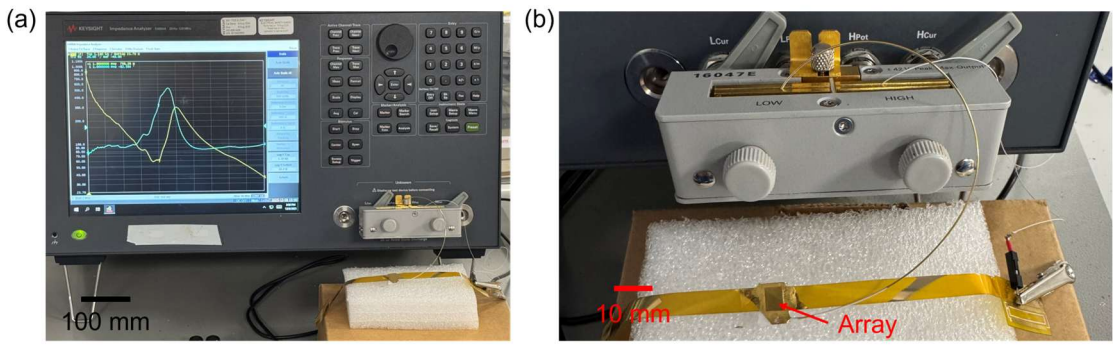

Figure 3.18 (a) Impedance analyser and (b) test fixtured used in 1D array element impedance measurement.

Prior to measurement, appropriate range selection and system calibration were necessary to exclude measurement artefacts arising from low-frequency resonances, cabling, and other electrical components. From the impedance spectra, f_r, f_a and effective coupling coefficient, k_{eff}, can be estimated according to according to the IEEE standard [59]:

$$k_{eff} = \sqrt{1 - \frac{f_r^2}{f_a^2}} \qquad \text{Eq. 3.6}$$

3.5.2 Pulse-echo response

Pulse-echo measurements were performed using an automated US scanning system (Figure 3.19). The system comprised a pulser/receiver (DPR 300, BYK Additives & Instruments, Wesel, Germany), a data acquisition (DAQ) system (PXIe 1071 and NI 5772, National Instruments, Austin, TX, USA), and a linear x-y motion system (Motion Link Ltd, Berkshire, UK).

During the measurement, the transducers were submerged in DI water at room temperature. The pulser/receiver generated a broadband negative pulse (1.55 μJ energy, 48.7 Ω damping) to excite the transducers. The returning echo signals were first routed through an analogue band-pass filter, applied by the pulser/receiver. The filtered signals were then captured and digitised by the DAQ system. Finally, the time-domain echo waveforms were processed using a fast Fourier transform (FFT) to obtain their frequency spectra.

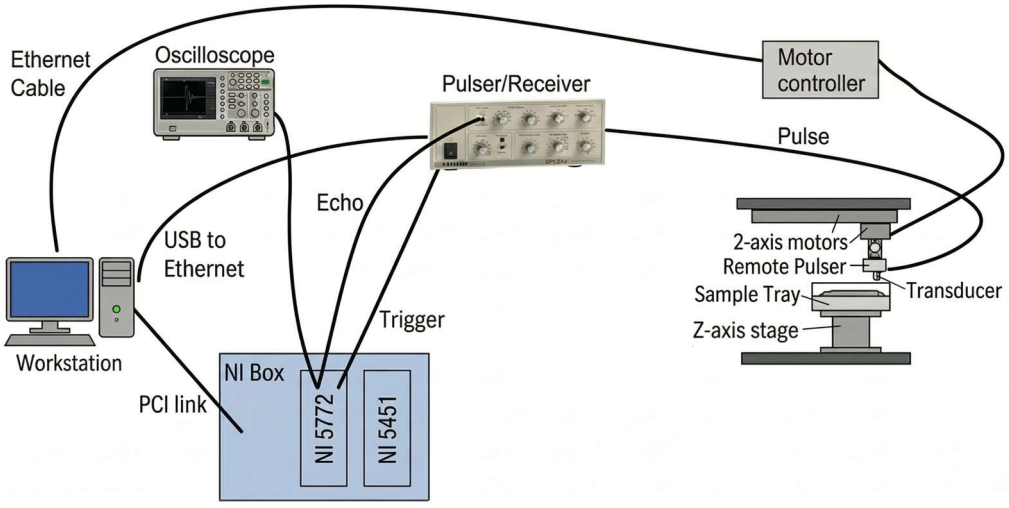

Figure 3.19: The schematics of the US imaging system.

3.5.3 Spatial Resolution

The spatial resolution of the transducers was initially assessed by scanning a wire phantom. Five tungsten wires with a diameter of Ø = 10 μm were secured onto a 3D-printed holder and submerged in DI water at room temperature. The wires were arranged with a spacing of 1 mm in both the lateral and axial directions. The transducer was mounted onto a motorised stage that performed scanning with a horizontal step size of 10 μm and excited with the pulser/receiver. The acquired data were averaged 32 times at each step to reduce noise. The images of the wires are reconstructed in Figure 5.5 (a), (d), and (g). The lateral and axial resolutions of each transducer were subsequently calculated using the following equations:

$$R_{\text{lateral}} = \frac{\lambda \times F}{l} \qquad \text{Eq. 3.7}$$

$$R_{\text{axial}} = \frac{\lambda}{2 \times BW} \qquad \text{Eq. 3.8}$$

where λ is the wavelength of the US in water, F is the focal length, and BW is the bandwidth of transducer. As the transducers are unfocused, the near-field distance (N) for a flat single-element transducer is calculated by:

$$N = \frac{l^2 \times f_c}{4c} \qquad \text{Eq. 3.9}$$

where l is the diameter of the acoustic aperture, c is the speed of sound in medium and f_c is the centre frequency of the transducer.

3.5.4 Sensitivity

The two-way insertion loss, IL, was evaluated for transducers as normal over a target frequency range, e.g. $5 < f < 28$ MHz for 15 MHz transducers. The transducers were excited during the measurement using a function generator (DG4102, RIGOL, Beijing, China) with a 5-cycle sinusoidal burst output via a 50-Ω impedance. The reflected echo signals from a flat quartz plate in DI water at room temperature were recorded using a digital oscilloscope (IDS-1202B, RS Components Ltd, Northants, United Kingdom) with a 1-MΩ input impedance. IL was calculated as:

$$IL = 20log\frac{V_1}{V_0} + 1.9 + \alpha \times 2d \times f_c^2 \qquad \text{Eq. 3.10}$$

$$\alpha = 2.2 \times 10^{-4}\ dB\ mm^{-1}MHz^2 \qquad \text{Eq. 3.11}$$

where V_1 and V_0 are the peak-to-peak voltages of the transmitted and received signals, respectively. The 1.9 dB term accounts for US signal loss at the quartz surface and α is the attenuation coefficient of US in water. $2d$ accounts for the round trip distance travelled by the transmitted and reflected waves [139].

3.5.5 Signal-to-noise ratio

The SNR serves as a critical metric for evaluating the transducer's detection capabilities within a tissue or tissue mimicking phantom.

From the images acquired by the Verasonics Vantage 128 research US system, a region of interest (ROI) exhibiting a stable signal response was selected to determine the mean signal amplitude (V_{tissue}). Concurrently, a distinct background region devoid of scattering targets was selected to characterise the noise floor (V_{noise}). The SNR was subsequently calculated using the following equation:

$$SNR = 20log\frac{V_{\text{tissue}}}{V_{\text{noise}}} \qquad \text{Eq. 3.12}$$

3.5.6 Crosstalk

For an US array transducer, one of the indicators showing interference between transducer elements is crosstalk. The combined electrical and mechanical crosstalk of the array was quantified across various adjacent element pairs and directions.

The experimental procedure involved utilising a function generator (DG4102, RIGOL, Beijing, China) to excite a single array element. The induced response signals from the adjacent elements were subsequently measured and recorded using the oscilloscope. The resulting crosstalk, expressed in decibels (dB), was calculated using the following relationship [95]:

$$Crosstalk = 20log\frac{V_2}{V_1} \qquad \text{Eq. 3.13}$$

where V_2 the excitation voltage applied to the tested element, and V_1 is the measured response voltage on the adjacent element.

3.6 Summary

This chapter has presented a methodology for the fabrication of high-frequency ultrasonic transducers, encompassing the engineering workflow from simulation to fabrication and experimental characterisation. Both single-element transducers and 1D linear arrays were developed, demonstrating the successful integration of each layer and precision manufacturing techniques.

Protocols were established to address high-frequency fabrication challenges, particularly in the processing of 1-3 piezocomposites and array elements. The implementation of 'epoxy-framing' effectively mitigated mechanical failure in fragile single crystals. This optimised method improved 1-3 composite fabrication efficiency.

In summary, the specific equipment setups, customised fixture designs, and step-by-step fabrication procedures described in this chapter provide a robust foundation for the reliable production of high-performance ultrasonic transducers. The methodologies developed here not only resolve specific manufacturing bottlenecks but also offer a robust fabrication process for future high-resolution imaging applications.

Chapter 4 High-frequency ultrasound transducer integration with MSCR*

4.1 Introduction

In this chapter, the innovation lies in the synergistic co-design of miniaturised US single-element transducers with MSCRs, with the aim to establish a proof-of-concept platform that enables simultaneous advancements in navigation, localisation and diagnostic imaging. The feasibility of this integrated architecture is evaluated via preclinical porcine models. The primary objective of these trials is to demonstrate the fundamental capability for intracorporeal imaging by US and potentially localised drug delivery by MSCR, addressing the functional requirements necessary for future deployment in anatomically challenging regions such as neurovascular and pancreaticobiliary networks [140] (Figure 4.1). These proof-of-concept demonstrations were designed to provide a basis for translating the technology toward broader clinical applications.

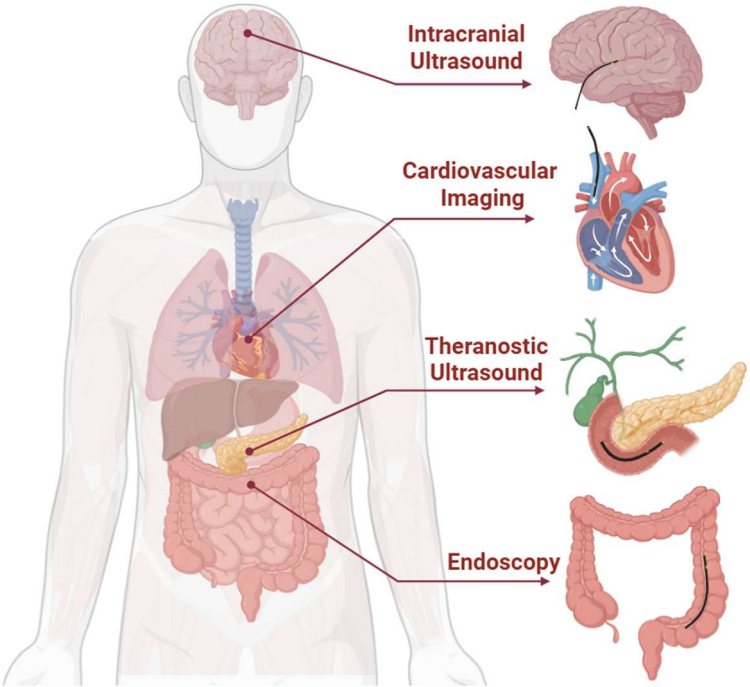

Figure 4.1 Applications for US-enabled MSCRs. (BioRender (2026) https://BioRender.com/mxcqli2)

* This work was conducted in collaboration with A. Bacchetti, a PhD student in the STORM Lab at the University of Leeds. A. Bacchetti was responsible for the fabrication and control of the MSCR. I was responsible for US-related work, including transducer fabrication and characterisation, US system control, data acquisition, and the integration of the US transducers with the MSCR. The US-related work was conducted in the C-MIU Lab at the University of Glasgow.

4.2 MSCR fabrication and integration

The incorporation of active US components into MSCRs introduces engineering challenges distinct from passive sensing solutions. Specifically, the integration of coaxial interconnects introduces mechanical stiffness that can impede the continuum flexibility of the robot, while the added payload mass may dampen the kinematic response under magnetic actuation. Furthermore, preserving signal integrity through micro-connectors is critical for high-fidelity data acquisition.

Beyond the robot itself, the definition of an optimal deployment strategy, specifically the delivery mechanism required to navigate the MSCR to the target site, remains a key design consideration. Therefore, establishing a fabrication protocol that ensures high-yield electromechanical integration without degrading MSCRs' performance is important.

This section introduces two integration configurations, Tentacle 1 (T1) and Tentacle 2 (T2), developed to address potential clinical challenges. Configuration T1 was the first prototype. This prototype was utilised for initial characterisations while validating physical integration feasibility. Configuration T2 represents the subsequent iteration, featuring enhanced structural uniformity and expanded functionalities.

The T1 configuration (Figure 4.2) consists of a cylindrical MSCR with a diameter of 3 mm. A discrete assembly method was used to construct this model. The MSCR was fabricated prior to transducer integration. A single-element transducer was then positioned at the distal tip for axial imaging or at the lateral surface for side imaging.

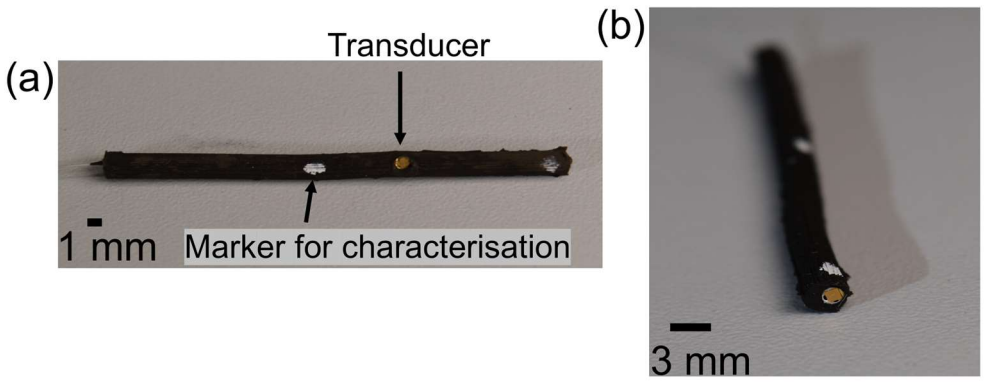

Figure 4.2 Images of integrated transducer layouts for T1 MSCR designs with (a) an axial tip-based transducer and (b) a lateral transducer situated 25 mm from the distal tip.

The T2 configuration (Figure 4.3) was engineered to expand these fundamental capabilities. It introduces rotational scanning and potential drug delivery. The T2 design specifically addresses the geometric constraints of minimally invasive interventions. This configuration achieves miniaturisation and functional integration without compromising the underlying magnetic response.

The T2 device features a reduced cross-sectional profile to navigate narrow and tortuous anatomical networks. This size reduction enables access to organ branches unreachable by the T1 architecture. The integrated dual-transducer configuration provides two diagnostic modalities. The lateral transducer can be used to perform rotational scanning to resolve cross-sectional morphology and detect wall-adhered pathologies, such as atherosclerotic plaques. The axial transducer conducts sweep scanning to provide a forward-viewing assessment during navigation. The device can potentially execute a complete scan-detect-treat workflow following pathology identification. It also employs independent auxiliary channels to enable potential drug delivery, establishing a closed-loop system for site-specific therapy.

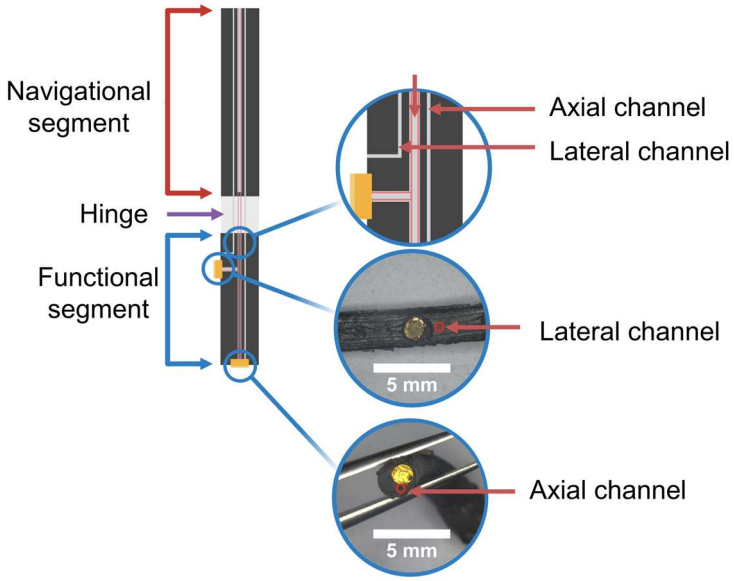

Figure 4.3 Schematic of finalised T2 device with integrated transducer layouts for T2 MSCR designs

The system was designed for deployment through the instrument channel of a standard commercial endoscope. This endoscope functions as the primary delivery vehicle to the region of interest. The final device was restricted to a diameter of 2.5 mm to fit within the endoscope working channel. Ultrafine 48 AWG coaxial cables (Alpha Wire, New York, USA) were selected for US signal transmission. These specific cables

minimise the adverse effects of interconnect stiffness on the continuum mechanics of the MSCR. This integrated architecture required a multi-stage fabrication protocol.

4.2.1 US Transducer design and fabrication

The 1-3 composite US transducer was developed using PIN-PMN-PT single crystals following the procedure in Section 3.4.1.

The area of the transducer's piezoelectric component was designed to be 1 mm^2 to match the 50 Ω load of the coaxial cable and pulse-receiver, and for integrating with the MSCR diameter. Acoustic characterisations were conducted to evaluate the performance of the PIN-PMN-PT single crystal based 1-3 composite US transducers, and the results are presented in Figure 4.4.

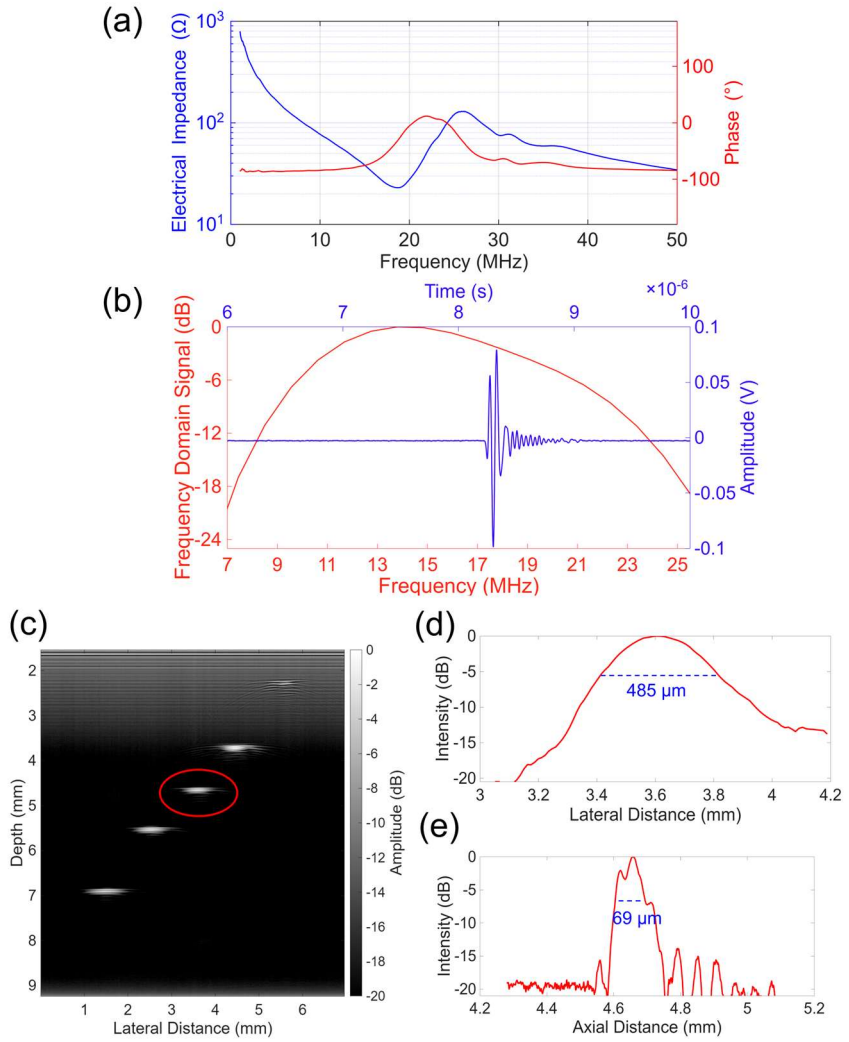

Figure 4.4 (a) Measured impedance magnitude / phase spectra of PIN-PMN-PT 1-3 composite transducer, (b) measured pulse-echo response in time and frequency domain, (c) B-scan for wire phantom image, (d) and (e) lateral and axial resolution measurement.

Electrical impedance spectroscopy (Figure 4.4a) was conducted to evaluate the transducer's basic performance. The electrical resonance and anti-resonance frequencies were measured to be 17.5 MHz and 25.2 MHz, and k_{eff} was estimated as 0.72. Pulse-echo characterisation (Figure 4.4b) was then performed to measure the transducer's f_c and the -6 dB bandwidth. The resolution was evaluated using the wire phantom described in Section 3.5.3. B-scan imaging for the wire phantom (Figure 4.4c) was plotted, and the resolution (Figure 4.4d) of the transducer was measured subsequently. Two-way IL was measured following the protocol in Section 3.5.4. The overall transducer performance is summarised in Table 4.1. These validated acoustic parameters guarantee good US imaging capabilities, establishing a foundation for integration with MSCRs.

Table 4.1. Performance summary for PIN-PMN-PT 1-3 composite US transducer.

Properties	
k_{eff}	0.72
f_c	15.3 MHz
-6dB bandwidth	73%
Two-way IL	22 dB
Lateral resolution	485 μm
Axial resolution	69 μm

The transducers fabricated for MSCR exhibited better performance than other reported 1-3 composite-based devices in Table 4.2 owing to exceptionally high piezoelectric and coupling coefficients.

Table 4.2. Comparison of sensitivity of 1-3 composite-based US transducers.

Transducer active material	IL (dB)
PMN-PT single crystal 1-3 composite [100]	28.4
BNBT-6 sol-gel fiber 1-3 composite [141]	34.8
KNNS-BNZH 1-3 composite [142]	30.0
KNN 1-3 composite [74]	25.1
PIN-PMN-PT single crystal 1-3 composite (This work)	22

4.2.2 Tentacle 1 fabrication

This section describes the integration of miniature custom-fabricated US transducers and associated electrical interconnects within a cylindrical MSCR with 50 mm length and 3 mm diameter. In Figure 4.2, two configurations were developed to facilitate specific sensing modalities during navigation:

- Lateral Configuration (Figure 4.2a): The transducer is oriented perpendicular to the robot's axis, positioned 25 mm from the distal tip, to facilitate lateral proximity sensing.
- Axial Configuration (Figure 4.2b): The transducer is embedded axially at the distal tip of the MSCR, enabling forward-facing sensing.

The fabrication workflow for the T1 MSCR prototype is illustrated in Figure 4.5. Modular injection moulds were produced via fused filament fabrication (PLA, Ultimaker S5, The Netherlands) to define the cylindrical geometry. The soft robotic matrix was composed of a silicone elastomer (Ecoflex 00-30, Smooth-On Inc., PA, USA) doped with neodymium-iron-boron (NdFeB) microparticles (MQFPB+, Magnequench GmbH, Germany) in a 1:1 mass ratio. The composite mixture was homogenised and degassed in a high-vacuum centrifugal mixer at 1400 rpm and 20 kPa for 90 seconds. Prior to injection, a nitinol rod with a diameter of 0.75 mm was positioned within the mould to serve as the core for the central internal wiring channel. Additionally, cavities with a diameter of 1.50 mm were created at the distal tip and lateral sidewall using appropriately positioned nitinol inserts to accommodate the transducer housing. The prepared mixture was subsequently injected into the mould cavity, and thermal curing was conducted at 40 °C for 20 minutes. To facilitate visual deflection analysis, white markers were applied at the distal tip of the T1 soft robot body.

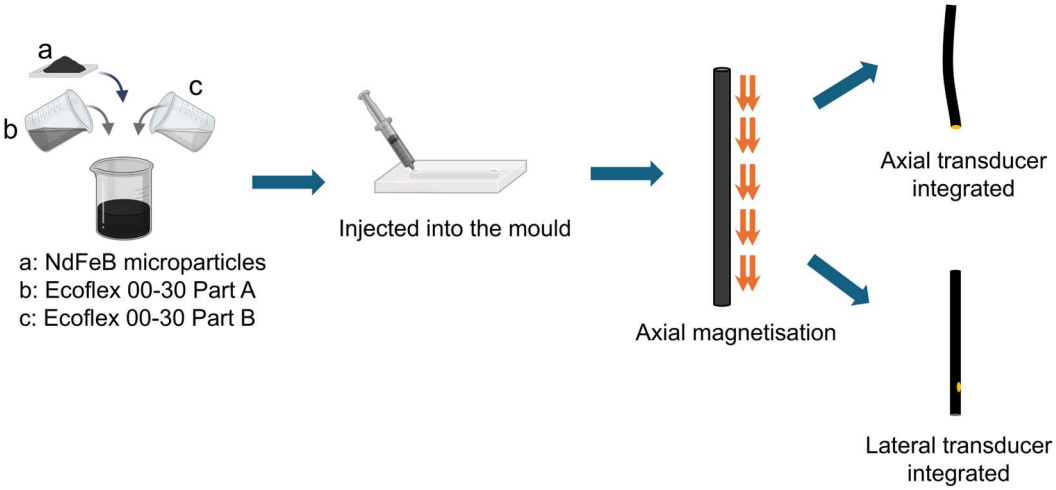

Figure 4.5 Overview of T1 fabrication procedure with integration of millimetre-scale US transducers. (BioRender (2026) https://BioRender.com/xhrw81q)

Following the initial cure, the transducer cabling was guided through the pre-formed central channel using a nitinol stylet with a length of 50 mm. The transducer was seated within its designated cavity and encapsulated using a small volume of magnetic silicone paste, which was cured under identical thermal conditions to ensure mechanical continuity. Post-integration, the MSCR was retained within its mould to prevent deformation and positioned within an impulse magnetiser (IM-10-30; ASC Scientific, RI, USA) in axial alignment with the impulse field. To establish a uniform axial magnetic profile, the samples were subjected to five sequential magnetic impulses of 4.50 T.

4.2.3 Tentacle 2 fabrication

The T2 prototype comprises two distinct functional sections: a proximal navigational segment and a distal functional segment. They were fabricated separately to allow for differential magnetisation profiles before final integration. The fabrication workflow for the T2 MSCR prototype is illustrated in Figure 4.6.

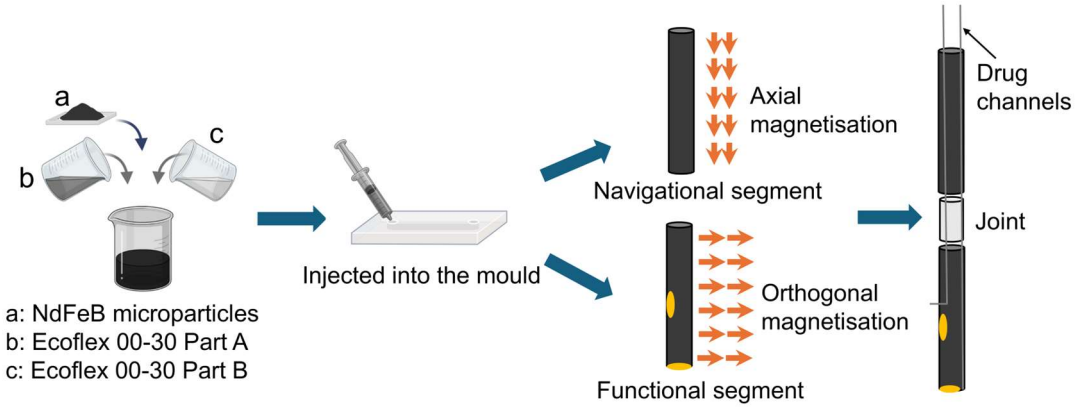

Figure 4.6 Overview of T2 fabrication procedure with integration of millimetre-scale US transducers.（BioRender (2026) https://BioRender.com/xhrw81q)

The navigational segment was produced using the same magnetic silicone formulation and degassing protocol as the T1 device. During mould design, two locating holes for the nitinol rods were incorporated into the CAD model and fabricated as part of the 3D-printed mould to define independent drug delivery channels. Prior to injection, two nitinol rods with diameter of 0.5 mm were positioned within the cylindrical mould with a length of 25 mm and a diameter of 2.5 mm. Additionally, a 0.5 mm-diameter braided sheath was centrally aligned to serve as a conduit for the two transducer coaxial cables, functioning as an internal backbone to maintain MSCR stability during mechanical insertion. The magnetic silicone mixture was subsequently injected into the mould cavity to encapsulate these internal structures. Following thermal curing, the transducer cabling was threaded through the central braided channel using a short nitinol stylet, and the segment was subjected to axial magnetisation.

The functional segment was fabricated in a geometrically similar mould with a length of 25 mm, featuring pre-defined cylindrical cavities to accommodate the dual-transducer configuration. A transducer was embedded at 10 mm from the distal tip with a lateral orientation and another one was integrated at the extreme distal tip in a forward-facing axial configuration. Additionally, two nitinol rods with diameters of 0.5 mm were inserted to generate independent drug delivery channels. This segment was cured under standard conditions and subsequently underwent orthogonal magnetisation.

To assemble the complete device, the two segments were aligned within a designed combination mould, separated by a gap of 5 mm. Fluidic continuity for the drug delivery system was established using bridging nitinol mandrels with a diameter of

0.5 mm: a rod with a length of 60 mm was utilised to ensure the continuity of the axial channel, while a rod with a length of 45 mm defined the lateral channel path. The 5 mm gap was subsequently filled with a non-magnetic silicone elastomer (undoped Ecoflex 00-30). Upon final curing, the rods were removed, and the channels were routed such that the lateral channel exited adjacent to the lateral transducer and the axial channel exited at the distal tip, completing the fabrication.

4.2.4 Ultrasound phantom fabrication

Soft tissue-mimicking phantoms were fabricated using Ecoflex 00-30 silicone. The two-part pre-polymer was combined in a 1:1 mass ratio and subjected to centrifugal degassing at 1400 rpm and 20 kPa for 90 seconds to eliminate entrapped air voids. The mixture was subsequently cast into bespoke moulds, which consisted of PLA external casings and high-resolution resin inserts (Formlabs Form 3+, MA, USA). Following casting, the samples were thermally cured at 40 °C for 20 minutes.

Two distinct phantom geometries were developed to evaluate the proximity sensing precision of the MSCR under varying orthogonal magnetic field conditions. For quantitative analysis, proximity was defined as the radial separation between the lateral surface of the MSCR and the luminal wall of the phantom. Both phantoms were immersed in DI water during use.

The first phantom incorporated specific channel profiles to replicate different anatomical regions. The linear straight channel (LS channel) had a uniform cylindrical lumen with a diameter of 10 mm and a length of 70 mm to simulate large linear vessels such as the ascending aorta. A second fabricated phantom has the LS channel geometry while incorporating a structural aneurysm (LSA channel) to assess the detection and dimensional estimation of pathologies. This LSA model replicated the baseline cylindrical geometry but included a lateral cavity representing an elliptical aneurysm with a diameter of 14 mm extending 6 mm radially from the tissue wall.

To investigate the transducer's capacity for multi-layer sensing and sub-surface imaging, a third phantom was constructed containing a discrete target. A copper wire with a diameter of 1 mm was embedded in a silicone block at a depth of approximately 1 mm from the surface. Copper was selected to provide a high acoustic impedance contrast with the silicone matrix. This configuration was designed to simulate small-

scale abnormalities, such as atherosclerotic plaques or early-stage arteriovenous malformations, located within the superficial sub-endothelium.

4.3 Characterisation of MSCR

Characterisation of the T1 prototype design was conducted within a Helmholtz coil system. These experiments quantified the mechanical deflection performance both with and without the transducer payload, thereby isolating the effect of the transducer mass on the deflection behaviour of the soft robot under magnetic actuation. Functional testing demonstrated the system's capability for real-time proximity sensing. Specifically, the side-viewing transducer utilised pulse-echo data to gauge the separation distance from organ or tissue walls during navigation, as well as for the diagnostic detection of pathologies such as aneurysms. Additionally, the axial transducer was employed to perform sweep imaging, successfully resolving sub-surface abnormalities.

The functional characterisation of the T2 prototype was performed using an external permanent magnet (EPM) system (NdFeB, Grade N52, KJ Magnetics, USA), with the primary objective of evaluating the rotational kinematics of the MSCR under orthogonal rotating magnetic fields and the resulting ultrasonic imaging quality. The experimental validation followed a progressive protocol: an initial bench test was performed using a wire phantom, followed by *ex vivo* assessments of porcine tissue in a custom-designed 3D-printed fixture. Finally, to establish imaging efficacy in realistic biological environments, rotational scans were conducted within the lower rectum and upper oesophagus of an *in vivo* porcine model.

4.3.1 Deflection methodology

When subjected to a spatially homogeneous external magnetic field, B, an MSCR generates a resultant torque arising from the interaction between the applied field and the internal magnetisation of the doped elastomer matrix. Modelling the axially magnetised cylindrical architecture as a magnetic dipole with a magnetic moment m, the device experiences an aligning torque, τ, governed by the following relationship [143]:

$$\tau = m \times B \qquad \text{Eq. 4.1}$$

The mechanical manifestation of this torque is strictly dictated by the orientation of the remanent magnetisation vector relative to the robot's principal geometric axes. In axially magnetised systems, the torque induces a bending moment that curves the soft body to align its longitudinal axis with the field lines. Conversely, for architectures characterised by lateral magnetisation, the resultant torque drives the robot to rotate about the central axis of its cross-section, inducing torsional deformation as the system attempts to align its internal transverse magnetisation vector parallel to the external magnetic field.

This magnetic loading is counteracted by internal elastic restoring forces generated as the MSCR undergoes deformation. Consequently, a state of static equilibrium is established, governed by the composite stiffness of the structure, which aggregates the mechanical contributions of the viscoelastic elastomer matrix and integrated functional components, such as electrical wiring. Within this theoretical framework, gravitational effects are considered negligible; thus, the deformation is modelled exclusively as a balance between the applied magnetic torque and the restorative elastic torque. Furthermore, as the external magnetic field is assumed to be spatially homogeneous, the spatial gradient of the field vanishes. This results in a net zero magnetic force, implying that the torque τ constitutes the sole active magnetic driver governing the kinematic interaction.

The integration of single-element transducers at discrete locations along the MSCR, combined with the axial routing of electrical interconnects, introduces increased mass and points of high local flexural rigidity. This mechanical heterogeneity attenuates the deflection amplitude when compared to a pristine, axially magnetised cylindrical reference MSCR lacking functional components. Therefore, comprehensive characterisation was performed via experimental analysis under varying orthogonal field conditions to quantify the deviations.

The deflection characteristics and accessible workspace of the MSCR were evaluated under controlled exposure to homogeneous magnetic fields. The robotic prototypes were vertically cantilevered within a three-dimensional Helmholtz coil system (3DXHC12.5-300, Dexing Magnet Tech. Co., Ltd., Xiamen, China). Figure 4.7 is a photo of the Helmholtz coil system. To capture quasi-static deflection profiles, a high-

resolution optical camera (acA2040-120uc, Basler AG, Ahrensburg, Germany) was aligned orthogonally to the primary plane of actuation.

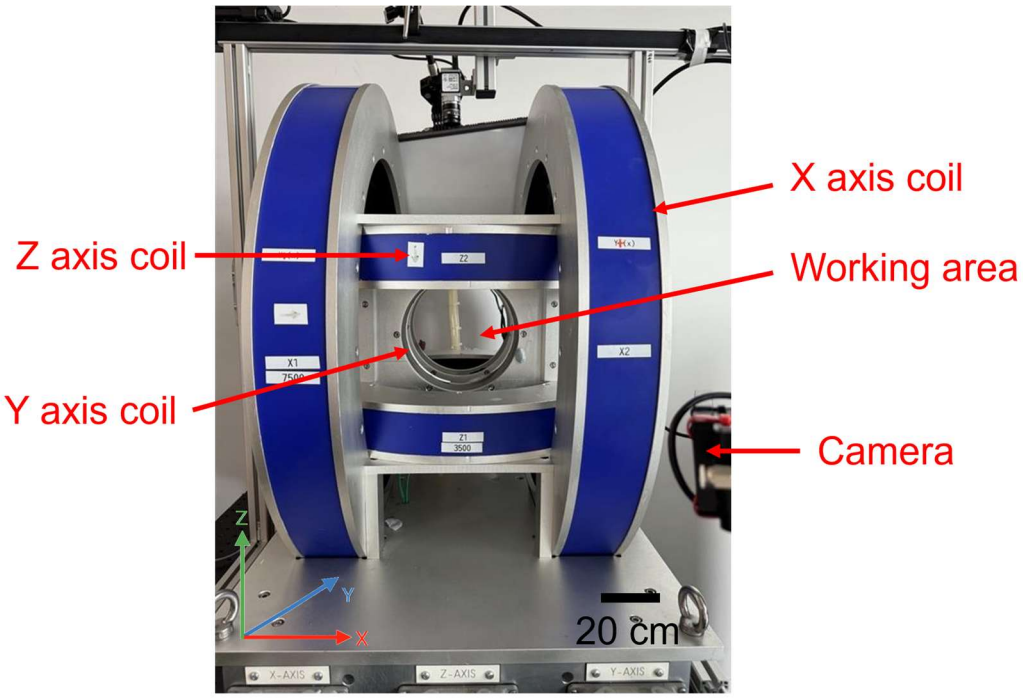

Figure 4.7: 3D Helmholtz coil setup for deflection characterisation.

Two distinct experimental protocols were executed to assess performance across different field regimes. The first characterisation involved an orthogonal magnetic field sweep ranging from 0 mT to 5 mT in increments of 0.5 mT in the X direction. This regime was designed to compare the sensitivity of tip deflection under low-field conditions. The second experiment expanded the orthogonal field sweep to a range of 0 mT to 15 mT in increments of 2.5 mT in the same direction. This broader range facilitated the investigation of the upper deflection limits and saturation behaviour.

Deflection performance under orthogonal field conditions

Characteristic deflection profiles were obtained for the cylindrical reference and transducer-integrated MSCRs. These related achieved tip deflection angle to orthogonal magnetic field strength. To provide a consolidated visualisation of the kinematic response, the recorded deflection profiles for all MSCR configurations were rotated to a vertical orientation and superimposed on the single composite plot shown in Figure 4.8.

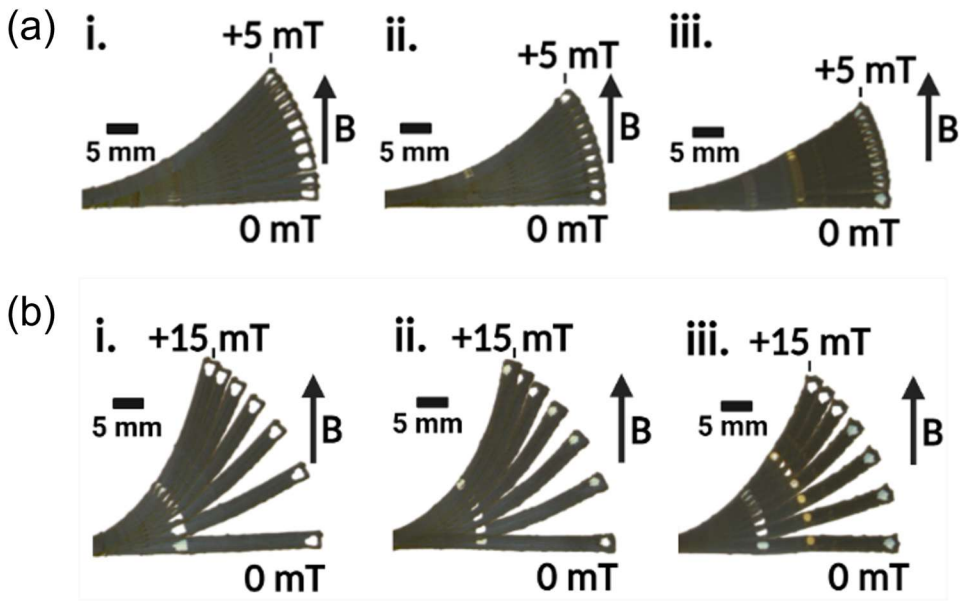

Figure 4.8 (a) Deflection profiles under 0 − 5 mT orthogonal magnetic field sweeps: i. cylindrical reference, ii. MSCR with an axial tip transducer, iii. MSCR with a lateral transducer and (b) deflection profiles under 0 − 15 mT orthogonal magnetic field sweeps: i. cylindrical reference, ii. MSCR with an axial tip transducer, iii. MSCR with a lateral transducer.

The pristine cylindrical reference consistently exhibited superior tip deflection angles compared to the functionalised transducer designs. However, the degree of deviation varied between the two experimental regimes, revealing distinct mechanical responses for the axial and lateral configurations in Figure 4.9.

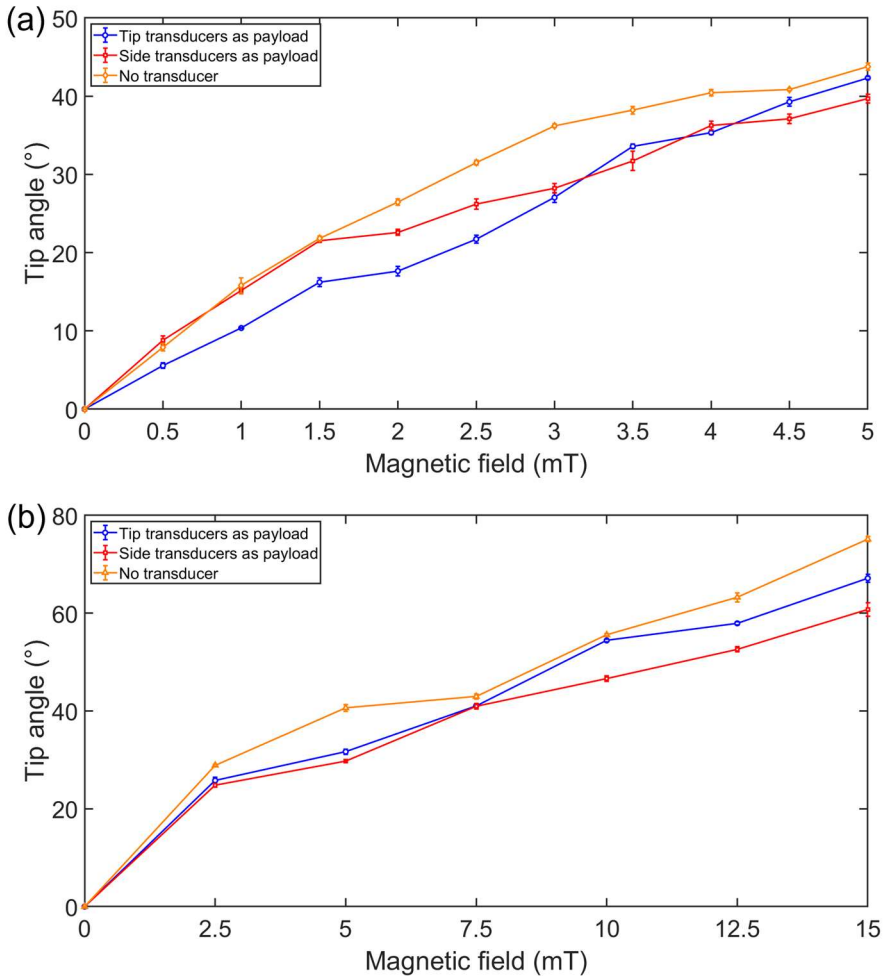

Figure 4.9 Comparison of tip deflection angle between cylindrical and transducer-integrated MSCRs under (a) 0 - 5 mT and (b) 0 - 15 mT orthogonal magnetic field sweeps. One sample of each MSCR type was tested three times, and the error bars represent the standard deviation of the three repeated measurements.

In the low-field experiment (0 mT to 5 mT), which evaluated initial responsiveness and fine control, the impact of component integration was most pronounced in the axial design. The axial configuration demonstrated a substantial mean discrepancy of 21.1% relative to the reference. The suppressed responsiveness, particularly below 1.50 mT, is attributed to the maximum mechanical impedance occurring at the distal tip, where the combined mass of the transducer and the increased rigidity introduced by the internal wiring directly counteract the magnetic torque.

The lateral design exhibited superior performance in this regime compared with the axial design, with a reduced mean deviation of 9.4%. This behaviour is explained by the positioning of the transducer at the midpoint, which created a mechanical 'fulcrum'. While the proximal segment experienced restricted deflection due to embedded

cabling, the unencumbered distal segment retained significant mobility. This 'fulcrum effect' allowed the tip to deflect more freely at low field strengths, reducing the discrepancy relative to the reference to as low as 5.42% in the initial increments.

In the broader high-field experiment (0 mT to 15 mT), intended to assess the saturation limit, the mechanical trends shifted. As the magnetic torque increased, the axial design overcame its initial inertial resistance, resulting in a narrowed mean discrepancy of 9.7% relative to the reference.

In contrast, the lateral design demonstrated a larger mean deviation of 16.2% over this wider range. Although the 'fulcrum' facilitated initial tip movement, the rigid mid-body integration effectively partitioned the MSCR into two segments with distinct stiffness profiles. At higher field strengths, the stiffened proximal segment (containing the wiring) constrained the device's overall curvature, preventing it from achieving the uniform, continuous bending profile observed in the cylindrical reference and limiting the maximum achievable deflection angle.

The two experiments share an overlapping magnetic field range from 0 mT to 5 mT. The MSCR deflection angles differ between the two datasets within this specific region. This variation results directly from the use of different magnetic field increments. These incremental differences alter the magnetic loading pathway and change both the deformation evolution and the effective loading rate. Thus, the system reaches different final deformation configurations within this low-field regime.

Although these kinematic variations exist, the discrepancy between the transducer-integrated MSCRs and the reference has minimal impact on clinical applicability. Given the high degree of unstructured complexity characteristic of intracorporeal environments, coupled with the inherent non-linear control challenges associated with soft continuum actuation, the recorded performance deviation should not compromise the operational efficacy of the device.

4.3.2 Proximity sensing

The proximity sensing capabilities for both positional tracking and diagnostic assessment were evaluated through a systematic navigation study within the LS and LSA channel geometries. The MSCR was mechanically coupled to a PTFE delivery

tube with a diameter of 2 mm via a heat-shrink polymer interface. Automated axial insertion was driven by a stepper motor (NEMA 17, GEMS Motor, USA) suspended vertically above the magnetic workspace.

The experimental protocol involved advancing the MSCR in discrete steps of 2 mm until the lateral transducer was fully submerged and acoustically coupled within the channel lumen. To maintain a stable, centric pose throughout the insertion trajectory, a constant holding magnetic field of -15 mT was applied along the global Z-axis. The insertion process spanned 17 steps. At each discrete interval, three independent pulse-echo measurements were acquired. These acoustic readings were subsequently compared against the kinematic ground truth provided by the stepper motor to quantify the navigational accuracy. Proximity distances were calculated utilising the ToF calculation in Section 3.3.2, derived from the time delay between the emitted pulse and the received echo:

$$s = \frac{c_l \times t_0}{2} \qquad \text{Eq. 4.2}$$

where s is the transducer-wall separation distance, c_l is the propagation speed of US in distilled water and t_0 is the period between pulse generation and return to the transducer. To validate the acoustic data, the calculated ultrasonic proximity values were cross-referenced with optical measurements derived from high-resolution video feeds, which served as the geometric ground truth.

Proximity sensing of phantom channel

In the experiments conducted within the LS channels, characteristic profiles (Figure 4.10) were generated to correlate the transducer's instantaneous relative position with the accuracy of the proximity measurements. This analysis allowed a continuous assessment of measurement fidelity throughout the insertion trajectory.

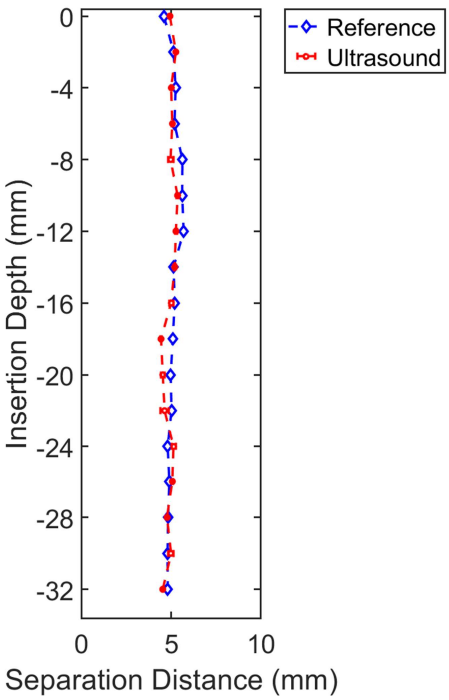

Figure 4.10 Comparison of US proximity measurements versus optical reference in the LS channel. Error bars represent the standard deviation derived from three independent measurement datasets.

Quantitative analysis within the LS channel revealed a mean absolute deviation of 0.288 mm relative to the reference. An average percentage difference of 5.61% was found throughout linear channel insertion. This low error margin validates the system's capacity to maintain high measurement fidelity over extended operational ranges, effectively demonstrating its utility for the precise characterisation of linear luminal environments exhibiting variable cross-sectional dimensions along their length.

Diagnostic proximity sensing of aneurysm

The capability of the transducer to detect localised luminal variations was evaluated by cross-referencing visual and ultrasonic proximity measurements throughout the insertion trajectory within the LSA channel (Figure 4.11).

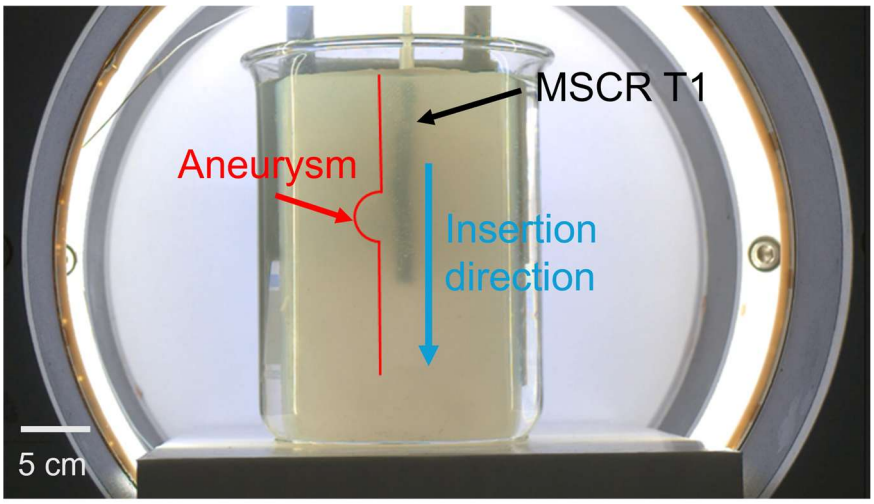

Figure 4.11 Illustration of LSA phantom for aneurysm detection.

The acoustic profile (Figure 4.12) obtained during the scan was characterised by discontinuous signal detection regions corresponding to the geometry of the simulated pathology. The upper and lower apertures of the simulated aneurysm were successfully identified at insertion depths of 22 mm and 34 mm, respectively. However, the intermediate regions exhibited signal discontinuities; these signal dropouts were attributed to the oblique angle of incidence along the curved cavity walls, which caused the acoustic energy to be reflected away from the transducer face. Notably, a distinct signal peak was recorded at 28 mm, corresponding to the apex of the cavity where the beam incidence was perpendicular to the interface.

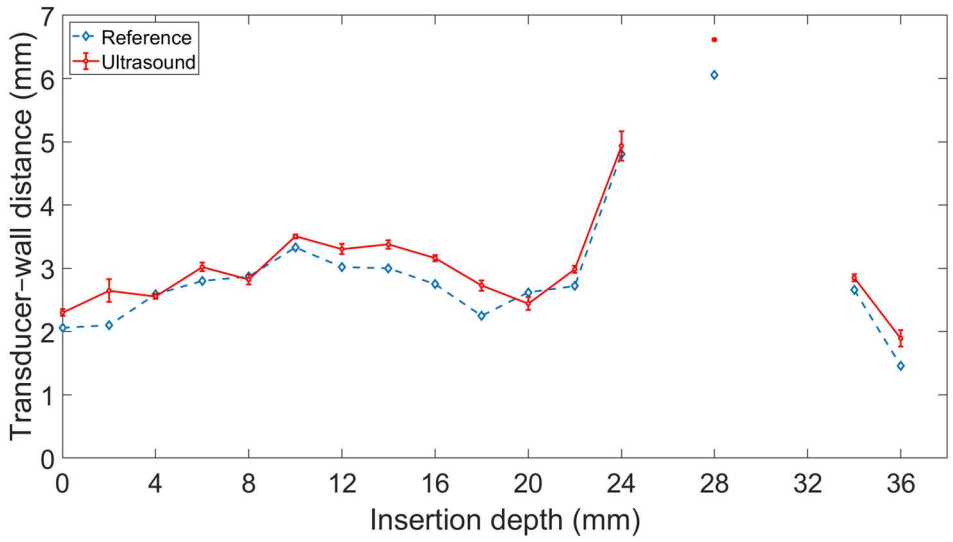

Figure 4.12 Comparison of US proximity measurements versus optical reference in the LSA channel. Missing data points indicate signal loss. Error bars represent the standard deviation derived from three independent measurement datasets.

A weak reflection was also detected at the 24 mm position, likely originating from internal reflections within the phantom structure. This artefact contributes to the measurement deviation and suggests complementary rotational cross-sectional B-scans would be needed to differentiate true geometric features from acoustic noise.

Quantitatively, the system achieved a mean absolute difference of 0.285 mm relative to the reference, and an average percentage difference of 11.07%. The total width of the aneurysm was measured to be 12 mm. The observed discrepancy in this diameter estimation is attributed primarily to the coarse step resolution of the motor actuation and the inherent fabrication tolerances of the phantom model. For the maximum depth measurement, a 9.14% difference was observed between the ultrasonic data and the visual ground truth. These results demonstrate the potential of the integrated transducer for both intra-operative positional sensing and diagnostic metrology.

4.3.3 Axial sweep scan

Sweep imaging of embedded abnormality

To evaluate the imaging capabilities of the axial transducer, the MSCR was subjected to a controlled orthogonal magnetic field sweep ranging from -1.20 mT to +1.20 mT in discrete increments of 0.20 mT (Figure 4.13). At each discrete measurement point, the US transducer was operated in transmit - receive mode. This actuation protocol enabled the device to perform a sweep scan of a copper wire of 1 mm diameter in the phantom to assess signal resolution. The robotic assembly was rigidly suspended in a vertical orientation, maintaining a nominal distance of approximately 1 mm from the phantom surface. Throughout the magnetic sweep, a total of thirteen US acquisitions were executed. To enhance the SNR, the return echo signals were acquired by the oscilloscope, averaged over 64 cycles, and subsequently stored for analysis. The datasets were utilised to spatially resolve the transducer's position relative to both the external surface boundary and the embedded subsurface anomaly.

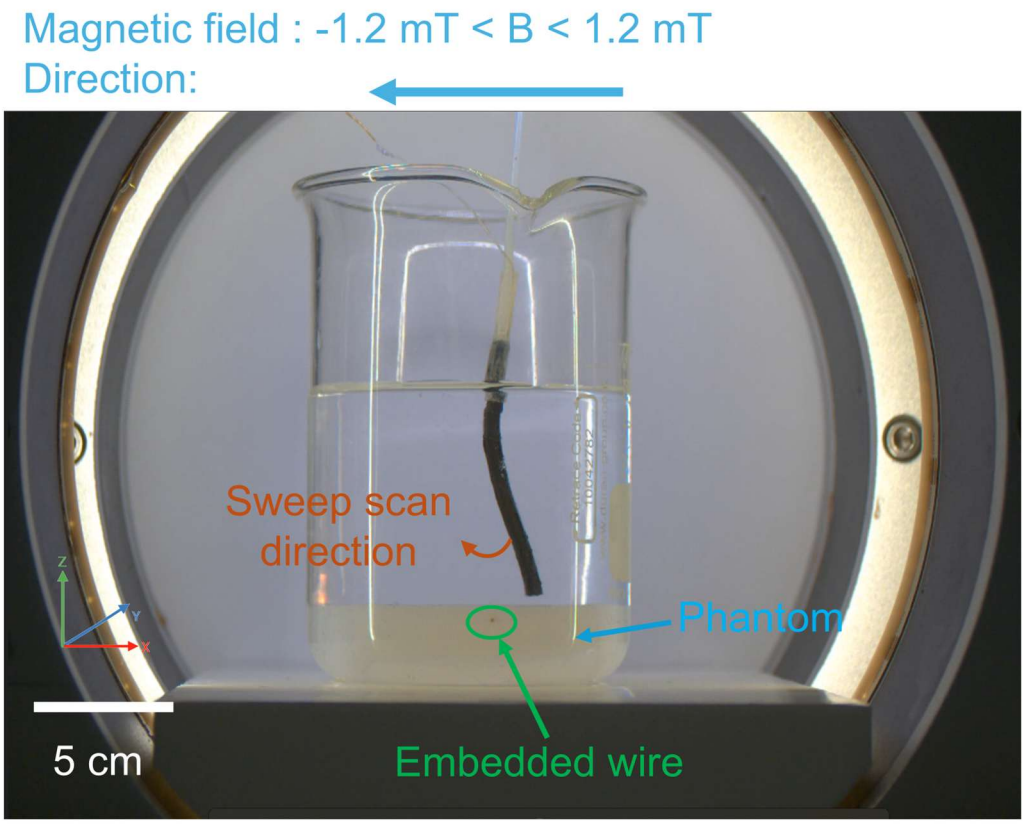

Figure 4.13 Illustration of multi-layer sensing sweep scan in the Helmholtz coil setup.

The resulting B-scan image is presented in Figure 4.14. The data reveal a distinct, high-intensity boundary corresponding to the phantom surface, indicating strong acoustic impedance contrast. Simultaneously, the contour of the embedded copper wire is clearly resolved within the phantom. Notably, the grey-scale amplitude of this embedded wire is attenuated relative to the surface interface, a phenomenon attributed to the combined effects of significant surface reflection and acoustic attenuation within the silicone phantom.

These results validate the capability of the distally integrated axial transducer to simultaneously characterise surface topography and detect subsurface endoluminal abnormalities within a single diagnostic sweep. Crucially, measurement fidelity was preserved across a tip deflection range of ±14°, suggesting applicability for imaging within large-diameter structures, such as the aortic trunk.

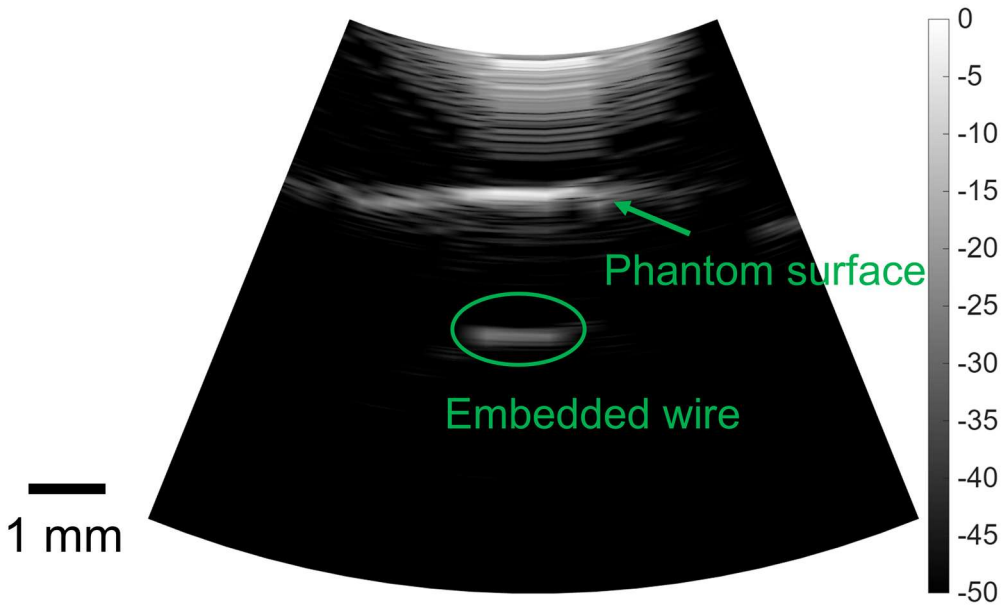

Figure 4.14 The B-scan image for the sweep scan.

Two critical kinematic constraints were identified during the characterisation process. Firstly, the MSCR exhibited limited mechanical responsiveness to magnetic field perturbations below 0.20 mT due to internal structural stiffness; consequently, a minimum field increment of 0.20 mT was established to ensure discrete, resolvable motion steps. However, this resulted in relatively large positional steps between successive A-scans, limiting the spatial sampling density and preventing the reconstruction of a fully smooth B-scan image. Future designs should increase the effective magnetic dipole moment of the MSCR to generate greater magnetic torque at lower field strengths, thereby enabling smaller field increments, finer positional control and smoother scanning. Secondly, while this validation utilised the controlled magnetic field gradient provided by the Helmholtz coil, clinical deployment will require an EPM attached to a robot arm. The inherent nonlinearity of EPM fields will introduce additional complexity into the control algorithm required to execute uniform-sweep scans in a realistic surgical environment.

4.3.4 Rotational scan of *ex vivo* phantom

Following the initial validation of the T1 prototype using the embedded wire phantom, and subsequent to the optimisation and fabrication of the integrated T2 platform, a rotational scan test was performed. The primary objective of this was to evaluate the kinematic rotational authority of the MSCR when subjected to the complex field

interactions of an EPM, alongside an assessment of the resultant ultrasonic imaging fidelity produced by the lateral transducer. This investigation is a critical bench-top validation, establishing the fundamental performance baselines required for high-resolution cross-sectional pathology scanning in clinical scenarios.

The experimental validation platform (Figure 4.15) comprised a cylindrical, axially magnetised EPM with a uniform diameter and length of 101.6 mm. This magnetic actuator was mounted to the end-effector of a 7-DoF serial robotic manipulator (LBR Med R820, KUKA, Germany) to enable precise field orientation [106]. US pulse-echo signals were captured using the oscilloscope, with data acquisition and storage controlled by a custom MATLAB (MathWorks, MA, USA) control algorithm. The data acquisition system operated at a maximum sampling interval of 0.3 s, with each recorded waveform averaged 16 times.

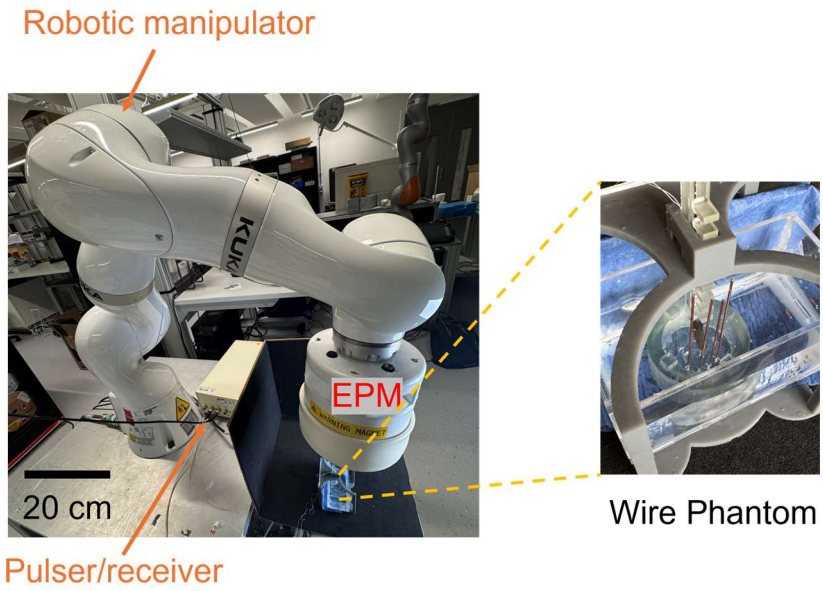

Figure 4.15 The experimental setup for rotational scaning.

During the experimental procedure, actuation was achieved exclusively by rotating the EPM to modulate the magnetic field vector, thereby inducing a resultant torque to drive the rotation of the MSCR. The remaining DoF of the robotic manipulator were utilised strictly to maintain the precise spatial positioning of the magnet relative to the test fixture. To systematically evaluate imaging performance and establish the optimal scanning velocity, a parametric study was conducted across a range of angular speeds. The robotic manipulator was programmed to execute rotations at velocities ranging from 10% to 60% of its maximum rated capability of 30 °/s. Throughout these trials,

the rotation was strictly constrained to a 180° sector to ensure operational safety and preserve the device's mechanical integrity.

The integrated T2 prototype was suspended from a custom 3D-printed fixture and fully submerged within a DI water bath to ensure acoustic coupling (Figure 4.15). To evaluate the rotational and imaging performance of the system, a wire phantom was constructed using five vertical copper wires with diameters of 0.5 mm. These targets were distributed across a 180-degree angular sector relative to the central axis of the device. The first wire was positioned at a radial distance of 5 mm from the scanning centre, while the subsequent four wires were arranged at increasing radii of 6, 7, 8 and 9 mm.

Figure 4.16 presents the B-scan reconstruction acquired at a robotic rotation speed of 10 °/s. A comparison between the designed 3D phantom model and the acoustic image revealed that only four of the five embedded wire targets were resolved. Since the angular positions of the wire targets were predefined in the model, the detected targets were used to estimate the angular coverage of the scan. This indicated that, although the external magnetic actuator completed a 180° rotation, the distal functional tip of the MSCR achieved an effective angular displacement of approximately 120°.

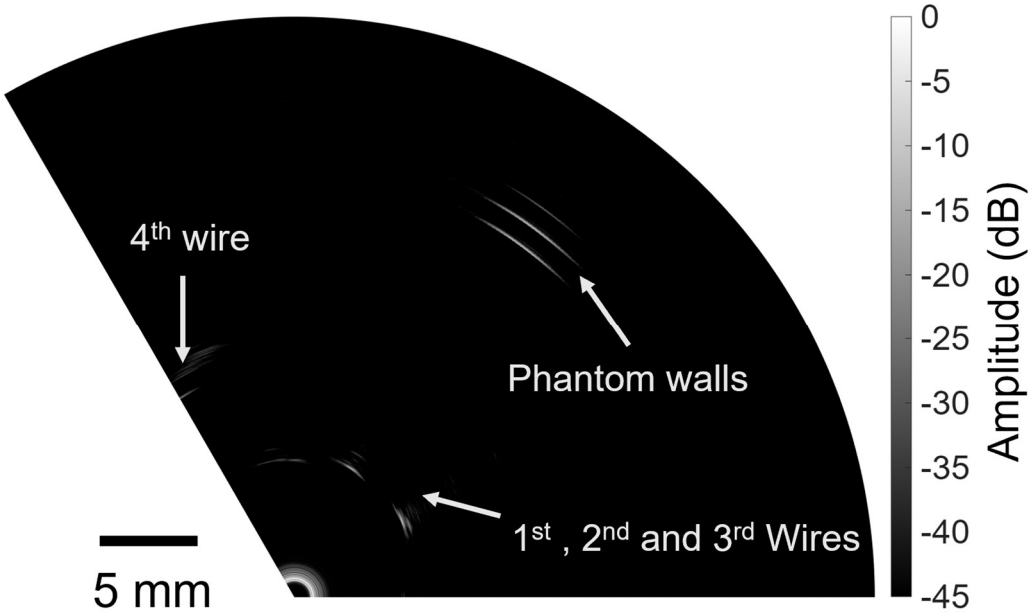

Figure 4.16 B scan rotational imaging of the wire phantom with 10 °/s rotation speed, showing a step between the third and fourth wires, which will be analysed in the subsequent discussion. (Dynamic range: 45 dB)

This kinematic discrepancy arises from the mechanical boundary conditions of the device, specifically the proximal fixation of the catheter. Although the MSCR is conceptually divided into a distal functional segment and a proximal navigation segment, the applied magnetic torque acts primarily upon the functional tip. Consequently, the rotation of the tip is counteracted by the inherent torsional stiffness and elastic restoring forces accumulated along the length of the polymer body. This mechanical impedance prevents a 1:1 transmission of rotation, resulting in the observed reduction in the total scan angle.

The relationship between actuation speed and image quality was systematically evaluated at speeds ranging from 10% to 60% (3°/s to 18°/s). Scanning velocities of 10%, 20%, and 30% (3°/s, 6°/s, and 10°/s) provided adequate spatial sampling and well-defined target boundaries. Under these conditions, the average spacing between successive scans remained within approximately one acoustic wavelength, which was adopted as the minimum practical requirement for continuous image reconstruction in this proof-of-concept system. At scanning velocities of 40% (12°/s) and above, the increased spacing between successive scans reduced the spatial sampling density and resulted in visibly coarser and less continuous target boundaries.

Further, detailed inspection of the 10 °/s scan reveals specific spatial anomalies: the partial visualisation of the phantom wall and a pronounced non-linear spacing between the third and fourth wire targets. The wire images suggest the motion of the MSCR is not strictly confined to pure axial rotation. Due to the continuous mechanical linkage between the functional and navigation segments, the magnetic coupling inevitably induces off-axis forces. This results in a hybrid kinematic response where the primary axial rotation is accompanied by secondary lateral displacement or bending. This complex motion profile distorts the relative spatial positioning of the distal targets, and is the most likely cause of the observed deviation in the location of the fourth wire relative to the preceding three.

After the resolution analysis performed on the wire phantom, the imaging protocol was advanced to a biologically relevant medium. An *ex vivo* porcine belly tissue specimen, Figure 4.17, was fixed within a custom-designed 3D-printed cylindrical fixture to simulate a luminal environment. The specimen was scanned, utilising the identical acquisition parameters established in the previous experimental phase.

Figure 4.17 Photograph of a section of *ex vivo* porcine belly mounted for scanning.

The B-scan reconstruction of the *ex vivo* porcine abdominal tissue is presented in Figure 4.18. Consistent with the lateral move observed in the phantom trials, the central luminal profile deviates from a concentric circular arc, exhibiting distinct geometric irregularities. This morphological distortion serves as further evidence of the complex kinematic coupling, confirming that the magnetic actuation induces unintended lateral displacement during axial rotation.

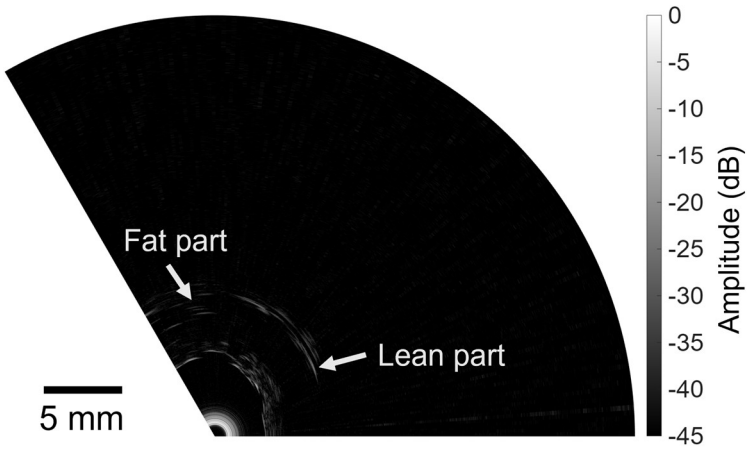

Figure 4.18 The B-scan rotational imaging of the porcine belly.

Despite these geometric deviations, the system successfully differentiated between distinct tissue types based on their acoustic properties. The lean regions were characterised by high echogenicity, producing strong interfacial reflections; however, this was accompanied by rapid signal attenuation, limiting the depth of visualisation in these specific zones. In contrast, the fat regions exhibited lower initial reflectivity

but significantly reduced acoustic attenuation, thereby permitting the visualisation of deeper anatomical structures and providing superior penetration depth.

Furthermore, the analysis highlights the critical influence of transducer orientation on image fidelity. It was observed that maintaining a normal angle of incidence between the ultrasonic beam and the tissue interface maximised SNR. However, given the under-actuated nature of the current magnetic control scheme, the precise angular alignment of the transducer varies throughout the rotational trajectory. As the device relies on passive kinematic compliance, this alignment cannot be actively corrected in real-time, leading to variations in image clarity across the scan sector.

While the current prototype demonstrates an effective scanning range of approximately 120° per actuation cycle, clinical cross-sectional pathology assessment usually demands full 360° circumferential coverage. To bridge this gap, two strategic approaches are proposed to extend the effective field of view. Firstly, the MSCR system could operate within a multimodal diagnostic workflow in which macro-scale imaging modalities, such as CT [69], [144], would provide global anatomical road mapping, while the MSCR would be deployed for high-resolution, localised imaging of specific regions of interest identified by the primary modality. Secondly, to achieve standalone 360° visualisation, a multi-stage acquisition protocol could be implemented. By manipulating the external magnetic actuator, specifically by temporarily retracting or repositioning the field source, the neutral resting pose of the MSCR can be mechanically reset. This would allow the device to execute sequential sector scans, for example, three 120° sweeps, which could subsequently be registered and computationally stitched to reconstruct a 360° cross-sectional profile. A similiar reconstruction principle was demonstrated by Liu et al., who combined complementary angular datasets acquired using a back-to-back dual-element IVUS catheter to reconstruct a more complete 360° vascular cross-sectional image [145].

4.4 *In vivo* experiment in a porcine model

Building upon the insights gained from the *ex vivo* bench-top validation, experimental evaluation of the T2 platform was advanced to an *in vivo* porcine model. The animal experiments were conducted in accordance with the Animal (Scientific Procedures) Act 1986 and the guidelines provided by NC3Rs and ARRIVE [146].

The device was deployed in two anatomical regions, the upper oesophagus and the lower rectum, to evaluate performance across varied luminal geometries. The primary objectives of these trials were twofold: firstly, to validate the feasibility of the magnetic control strategy under realistic physiological conditions, characterised by complex friction coefficients and dynamic tissue interactions; and secondly, to quantitatively assess the performance of the ultrasonic rotational scanning modality *in vivo*.

It is important to define the scope of this investigation. The axial imaging modality was excluded from this protocol, as its integration with the non-linear EPM actuation scheme had not yet had sufficient validation to warrant *in vivo* deployment. Furthermore, while the T2 architecture is designed with theragnostic capabilities, the evaluation of the drug delivery subsystem was conducted as an independent investigation and is distinct from the work presented in this thesis. Consequently, the analysis in this chapter focuses exclusively on the efficacy of ultrasonic imaging and the MSCR's kinematic response.

The experimental setup utilised for the trials is shown in Figure 4.19. To ensure consistency, the magnetic control and the ultrasonic data acquisition employed during the *in vivo* trials were identical to the protocols established during the preceding *ex vivo* validation phase.

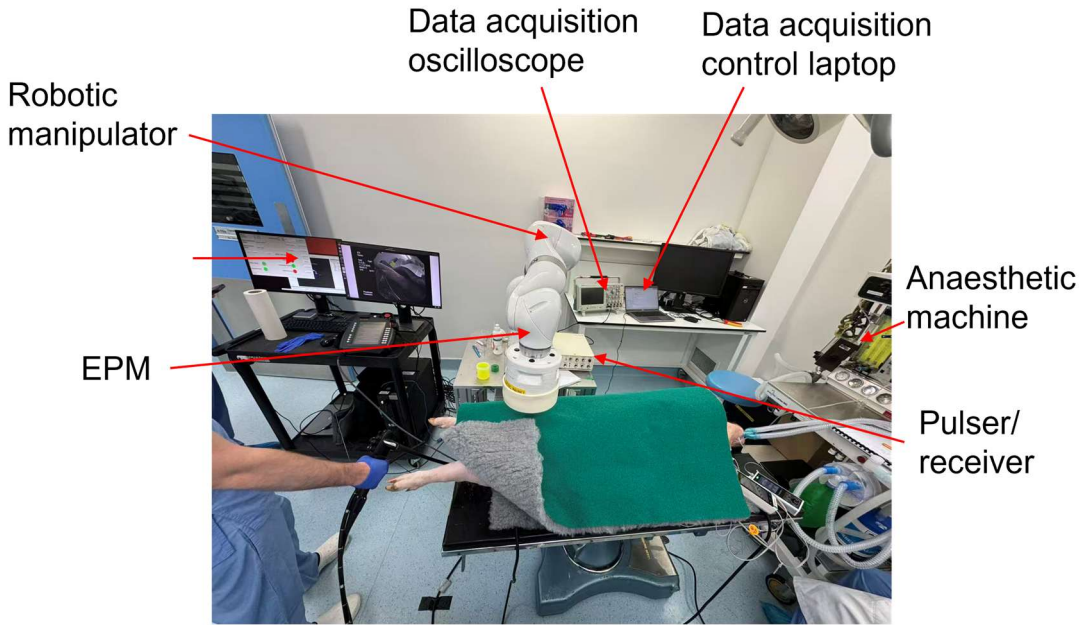

Figure 4.19 Detailed illustration of the *in vivo* setup.

Figure 4.20 depicts the complete T2 assembly incorporating dual US transducers. To facilitate axial translation within the lumen, a nitinol rod with a diameter of 0.5 mm was adhesively bonded to the proximal end of the device. This auxiliary mechanical component was required to provide manual propulsion, as the magnetic field gradients generated by the EPM are optimised for torque generation and do not exert sufficient attractive force to overcome frictional resistance for linear advancement in the anatomy. Additionally, signal transmission between the distal transducers and the external pulser/receiver unit was established via standard SMA connectors.

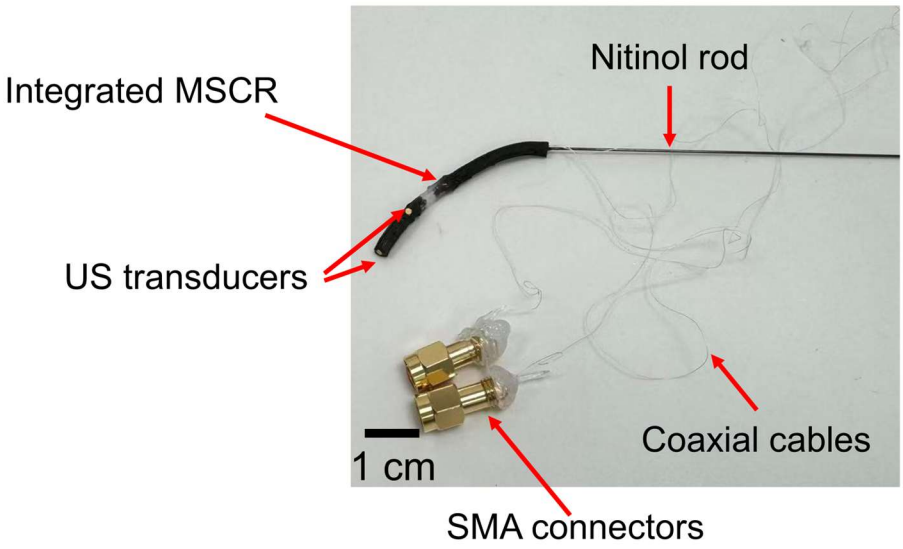

Figure 4.20 The fully integrated T2 device.

Due to the inherent structural compliance of the MSCR, direct insertion into the tissue lumens was mechanically unfeasible. To address this, a rigid polyvinyl chloride (PVC) guide tube was utilised as a primary delivery conduit to navigate the device to the proximity of the target anatomical site (Figure 4.21). Once the guide tube was positioned, the MSCR was mechanically advanced through the distal opening of the sheath using the proximal nitinol rod until the functional tip was correctly situated within the region of interest.

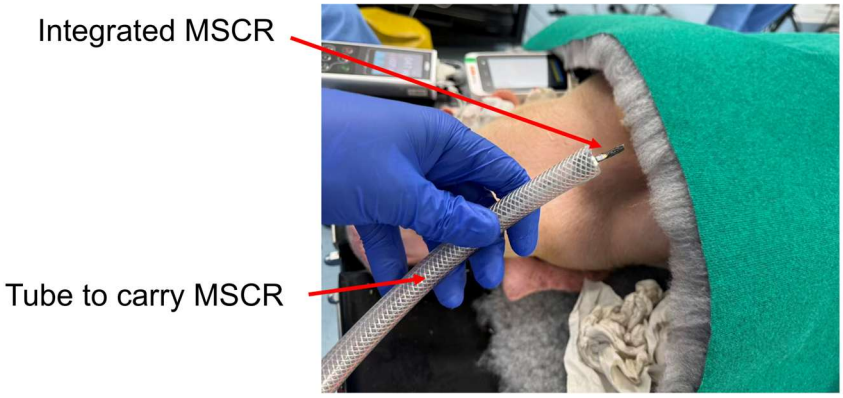

Figure 4.21 Experimental MSCR setup for *in vivo* porcine validation.

Upon successful deployment, magnetic actuation was initiated with the EPM executing rotations at 4.05°/s. Synchronously, the ultrasonic transducer was energised to emit pulse sequences. The resulting backscattered echo signals were captured by the oscilloscope, with the data acquisition, buffering, and storage processes performed by a MATLAB algorithm hosted on a laptop.

The experimental protocol was executed sequentially in the upper oesophagus then the rectum to evaluate the T2 platform. Testing the device in these two distinct anatomical regions allowed assessment of its performance under different geometric constraints and tissue interaction properties.

Figure 4.22 demonstrates the successful reconstruction of the internal oesophageal mucosa and adjacent tissue boundaries. These results demonstrate that the T2 platform can perform intraluminal imaging within a biological environment, successfully differentiating between the lumen wall and surrounding anatomical structures. However, the experimental procedure also highlighted significant challenges regarding acoustic transmission.

Unlike the *ex vivo* bench tests which utilised a water immersion bath, the *in vivo* environment lacked a consistent fluid medium to ensure continuous acoustic coupling. Although US transmission gel was applied to the transducer surface prior to insertion, an adequate amount could not be consistently delivered to the transducer-tissue interface, and the irregular anatomical geometry further prevented consistent physical contact between the transducer and the tissue wall. This intermittent contact resulted in fluctuations in signal stability and amplitude throughout the scanning procedure.

Furthermore, the tribological environment within the oesophagus differed markedly from the controlled phantom setups. The variable frictional forces acting upon the device surface introduced significant kinematic uncertainty. In the absence of an optical camera to provide visual feedback, the precise angular displacement of the functional tip could not be verified in real-time. The B-scan presented in Figure 4.22 was reconstructed using the same method as in the bench tests. Sequential A-scans were distributed across the assumed the° angular range, and their echo depths were mapped into polar coordinates to form the image. The 120° range was estimated from the preceding phantom experiment rather than directly measured *in vivo*.

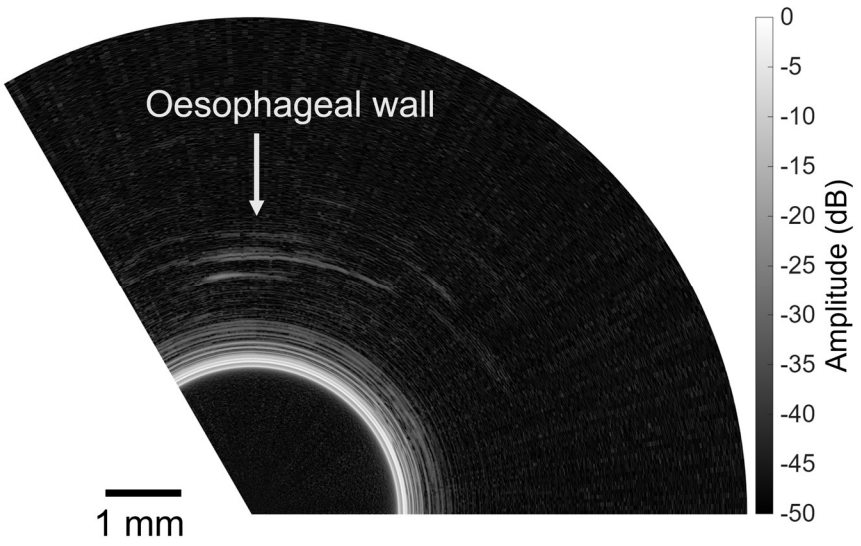

Figure 4.22 Porcine oesophagus US images acquired using the T2 device.

Finally, the deployment phase revealed mechanical constraints associated with the device's physical properties. The inherent softness of the MSCR, while beneficial for safety, proved disadvantageous during axial insertion. High frictional resistance from the tissue interface impeded smooth forward translation, causing the catheter to undergo compression rather than advancement. This necessitated repeated manual manipulation and positional adjustments to successfully navigate the device to the target imaging site.

The replication of this protocol within the rectal cavity yielded no discernible imagery due to distinct physiological constraints. Unlike the oesophagus, the rectum is characterised by a collapsed luminal state except when passing material and this exerted significant compressive pressure on the device. Combined with the inherent

softness of the MSCR, this generated excessive frictional resistance that the magnetic actuator could not overcome. Consequently, the MSCR was mechanically immobilised, preventing the rotational motion required for ultrasonic scanning and highlighting a critical mechanical limit of the current soft robotic architecture in high-contact environments.

4.5 Conclusions

This chapter has presented the design, fabrication, and characterisation of millimetre-scale, sensorised MSCRs. The platform utilises integrated miniature US transducers to facilitate intracorporeal proximity measurement, and cross-sectional and multi-layer diagnostic sensing. Experimental characterisation of the impact of transducer integration indicated a determinate relationship between component placement and maximum deflection. It was established that an MSCR with an axially integrated US transducer maintained a deflection profile within 9.7% of a pristine cylindrical reference. Similarly, a design incorporating a lateral transducer achieved a deflection profile within 16.2% of the reference. Notably, the lateral configuration exhibited a distinct stiffness increase at the integration site, creating a ‘fulcrum’ effect that locally altered the bending curvature. A complete structural redesign was implemented in the T2 version, which resolved this effect.

The lateral US design demonstrated the capability to detect simulated pathological luminal boundaries. This performance highlights the system's potential as a reliable platform for real-time positional estimation and cross-section surface diagnostics.

The axial design had good measurement fidelity under variable orthogonal field conditions, validating its potential as a multi-layer diagnostic instrument for the detection and scale estimation of embedded sub-surface abnormalities. This capability opens up the opportunity to utilise US measurements for computational reconstruction of embedded pathologies, allowing the assessment of their progression. Integrating this with magnetically controlled two-axis surface scanning may enable the reconstruction of 2D multilayer images, significantly improving the visualisation of complex anatomical structures.

Following static characterisation, the system's dynamic performance was evaluated using rotational scanning protocols. These trials successfully validated the T2

prototype's ability to resolve cross-sectional features in both phantom and *ex vivo* tissue environments. However, kinematic analysis revealed a discrepancy between the actuation input and the distal tip response, with the MSCR achieving approximately 120° of effective rotation against a 180° magnetic input due to the torsional stiffness of the proximal navigation segment. Furthermore, a parametric study found that scanning speeds exceeding 10 °/s led to signal aliasing and image degradation, thereby establishing a clear operational limit for high-resolution acquisition with the current instrumentation.

The translational potential of the platform was further assessed through *in vivo* validation in a porcine model. The trials conducted in the upper oesophagus confirmed the operational feasibility of the magnetic control strategy under physiological conditions, successfully reconstructing luminal boundaries despite the challenges of acoustic coupling. However, deployment within the rectum highlighted the critical limitation that the inherent structural compliance of the soft body was unable to overcome the significant frictional resistance and compressive forces imposed by the collapsed luminal walls, resulting in mechanical immobilisation. These findings underscore the complex trade-off between softness for safety and rigidity for kinematic authority in high-contact anatomical environments.

Looking forward, the precise metrology provided by the onboard US transducer may serve as a feedback component in a closed-loop control architecture, modulating magnetic field strength and vector orientation for improved intra-operative shape-forming. To strengthen the contribution of this platform technology, future research should involve characterisation under more dynamic magnetic manipulation scenarios and within phantoms exhibiting greater geometric variability. This should include navigating bifurcations and detecting complex luminal constrictions. Furthermore, subsequent studies should characterise transducer performance under realistic variable flow conditions, utilising media that mimic the acoustic properties of physiological fluids.

Chapter 5 Sm:PIN-PMN-PT single-element transducer and array

5.1 Introduction

Single-element transducer-integrated MSCRs are currently constrained by the inability to perform real-time imaging, which requires time-consuming offline reconstruction after each scan. Meanwhile, the mechanical rotation required for sector scanning proved suboptimal currently during *in vivo* experiments. This chapter details two specific advancements to improve the performance of the US-integrated MSCR. The first phase of this development incorporates novel piezoelectric materials for high-performance single-element transducers.

With the emergence of advanced piezoelectric materials, there is motivation to investigate their superior performance to enhance the imaging capabilities of US integrated into the MSCRs. The first part of this chapter [1] reports the design, fabrication and characterisation of a 15 MHz 1-3 composite US transducer incorporating Sm:PIN-PMN-PT single crystal and compares its behaviour with undoped PIN-PMN-PT and PMN-PT single crystals. The spatial resolution, bandwidth and IL of the transducers are evaluated with standard phantom targets and *ex-vivo* imaging is demonstrated with *ex vivo* porcine belly tissue to provide an indication of potential performance in biomedical applications including in MSCRs.

The second part of the chapter sims to establish a proof of concept for array-integrated MSCRs to address the imaging challenges of the previous generation. Unlike single-element transducers which need mechanical movement or rotation to generate a two-dimensional image, array transducers can achieve this electronically through a series of aligned elements, with electronic scanning to generate the images. To suit diverse clinical applications, this technology allows for versatile element configurations, including standard 1D [137], 1.5D [95] arrays and 2D arrays which can enable real-time volumetric steering [147].

Operationally, array transducers offer a distinct advantage through electronic beamforming. By manipulating the timing and amplitude of excitation pulses, the US beam can be steered and focused dynamically at multiple depths without the need for

moving parts [148], [149]. This electronic control allows higher frame rates and provides the flexibility to target specific regions of interest [6] [5]. Furthermore, the multi-element configuration enables the use of advanced beamforming algorithms and excitation methods to process signals and enhance image quality for high-precision diagnostics [150], [151], [152].

The array investigation here focused on a large aperture size configuration to establish a functional baseline. A 64-element linear array with a centre frequency of 15 MHz was fabricated using the Sm:PIN-PMN-PT single crystal. Subsequently, the transducer impedance magnitude / phase spectra, spatial resolution, bandwidth, IL and SNR were measured. *Ex-vivo* imaging of porcine belly tissue again demonstrated the practical biomedical viability of this array. This work provides the essential transducer performance baseline required to integrate arrays into the next generation of MSCR devices.

5.2 Sm-doped PIN-PMN-PT single crystal

Piezoelectric materials are the predominant route to develop US transducers due to their high performance in energy conversion. Over the past 25 years, relaxor PT-based single crystals have emerged as the best materials for their outstanding piezoelectric and electromechanical properties, making them suitable for high-performance ultrasonic devices where material volume avoids prohibitive cost. In particular, high-frequency US ($f > 15$ MHz), which offers improved spatial resolution, has enabled enhanced imaging performance in specialised medical fields such as dermatology, intravascular diagnosis, and US capsule endoscopy applications [62], [81], [82], [83].

Among the relaxor PT-based materials, binary lead magnesium niobate-lead titanate (PMN-PT) single crystals have often been selected for high-frequency US transducers due to their excellent electromechanical coupling, k_{33}, high dielectric constants, ε_{33}, and remarkable piezoelectric constants, d_{33} [100], [132], [153]. However, despite these superior properties, PMN-PT single crystals suffer from intrinsic limitations, such as a very low coercive field, $E_c \sim 2\ \mathrm{kV/cm}$, and a low rhombohedral - tetragonal phase transition temperature, $T_{rt} \sim 60–96\ ^\circ\mathrm{C}$ [62], [154].

These drawbacks present challenges, particularly in US transducer fabrication. To overcome them, researchers have developed ternary single crystals based on lead indium niobate-lead magnesium niobate-lead titanate (PIN-PMN-PT) showing doubled $E_c \sim 4–5$ kV/cm and higher $T_{rt} \sim 105–120$ °C compared with PMN-PT [155], [156], [157]. Whilst offering improved reliability and stability, PIN-PMN-PT also exhibits exceptional electromechanical and piezoelectric properties. As a result, PIN-PMN-PT single crystals are increasingly favoured for use in advanced US transducers, particularly in applications requiring high-frequency operation, high sensitivity and stable performance with temperature range [133], [158], [159].

To further improve the performance of US transducers, researchers are exploring the doping of rare-earth elements into existing material compositions [160], [161], [162]. This has been shown to alter the piezoelectric and electrical properties of materials significantly. Among the doping materials, Sm was demonstrated by Li et al. to achieve a record-high d_{33} of 1,500 pC/N and $\varepsilon_{33}^T/\varepsilon_0$ of > 13,000 [163]. Sm-doped ceramics were also fabricated into US transducers, showcasing high bandwidth and superior sensitivity [75], [164]. Subsequently, Sm-doping was applied to binary PMN-PT. These crystals exhibited unprecedented d_{33} of 3,400-4,100 pC/N and $\varepsilon_{33}^s/\varepsilon_0$ of ~12,000, along with property uniformity across the boule, with d_{33} variation of < 20%, better than conventional PMN-PT crystals [165]. However, the phase transition temperature decreased to 47-60 °C which is near room temperature. This thermal instability limits the performance in practical applications.

More recently, Sm:PIN-PMN-PT crystals have become available commercially, exhibiting exceptional piezoelectric properties, d_{33} = 2,189 pC/N, k_{33} = 0.94, and a high dielectric constant, $\varepsilon_{33}^T/\varepsilon_0$ = 6,392, in the <001> orientation [155]. The coercive field of Sm:PIN-PMN-PT is comparable to that of undoped PIN-PMN-PT while maintaining higher $\varepsilon_{33}^T/\varepsilon_0$ and d_{33} than PMN-PT single crystals. Meanwhile, its T_{rt} (82–99 °C) remains well above room temperature, suggesting it is compatible with practical fabrication processes described in Section 3.4.1. Specifically, to address the significant acoustic impedance mismatch between piezoelectric material, >30 MRayl, and biological tissue, ~1.5 MRayl, a composite structure is employed, with either 2-2 connectivity for arrays or 1-3 connectivity for transducers. This structural configuration reduces acoustic impedance, enabling more efficient transmission of acoustic energy into soft tissue. The design simultaneously enhances k_t, lowers tan δ,

and reduces lateral mode propagation [166], [167]. However, it requires dicing the material through its thickness and subsequent thinning, both of which challenge material stability.

5.3 Material properties

Table 5.1 summarises the material properties used in this study. These values were obtained experimentally using the characterisation methods detailed in Section 3.3.1.

Table 5.1 Properties of Sm:PIN-PMN-PT, PIN-PMN-PT, and PMN-PT single crystals.

	Sm: PIN-PMN-PT	PIN-PMN-PT	PMN-PT
Electromechanical coupling coefficient k_t	0.56	0.53	0.57
Piezoelectric constant d_{33} (pC/N)	2189	1520	1428
Relative clamped dielectric constant $\varepsilon_{33}^S/\varepsilon_0$	760	713	947
Dielectric Loss, tan δ	0.007	0.004	0.006
Density ρ (kg/m^3)	8,230	8,200	8,125
Longitudinal wave velocity v_L (m/s)	4,400	4,360	4,537
Acoustic impedance Z_a (MRayl)	36.2	35.7	36.7
Coercive field E_c (kV/cm)	4.8–6	4.5–6	~2
Phase transition Temperature T_{rt} (°C)	82–99	105–120	60–96
Curie Temperature T_c (°C) [155], [158], [159]	143–175	120–160	~130

5.4 Single-element transducers

5.4.1 Design and fabrication

The three 1-3 composite transducers were designed, simulated and fabricated following the procedures introduced in Chapter 3 and demonstrated in MSCRs in Chapter 4. To match the standard 50 Ω load of the coaxial cable and pulser/receiver, the piezoelectric materials area was specified as 2.25 mm^2, following Eq. 2.6. Table 5.2 shows the design parameters of the transducers.

A single Parylene C matching layer, Z ~2.6 MRayl, was incorporated to match the acoustic impedance difference between the 1-3 composite, Z ~16.5 MRayl, and the load medium, Z ~1.5 MRayl. Figure 5.1 shows the finalised transducers and a schematic cross-section of their structure.

Table 5.2 Acoustic parameters for single crystal/epoxy 1-3 composite transducers.

Layer	Material	Thickness (mm)	Acoustic Impedance (MRayl)
Active Layer	Single Crystals	0.070	~16.5
Matching Layer	Parylene C [121]	0.025	~2.6
Backing Layer	E-solder 3022 [85]	0.500	5.92

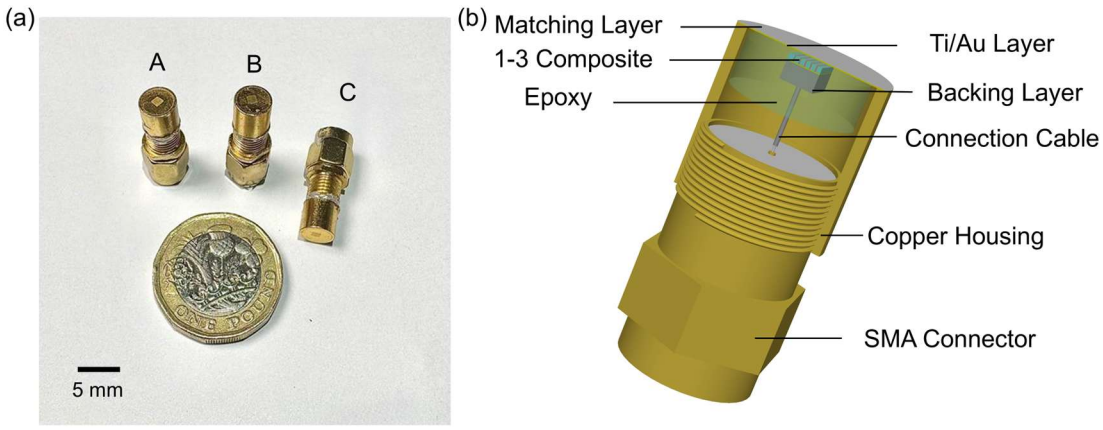

Figure 5.1 (a) Photograph of transducers with a UK £1 coin, and (b) Schematic of transducer cross-section. (A: Sm-PIN-PMN-PT transducer, B: PIN-PMN-PT transducer, C: PMN-PT transducer.)

5.4.2 Transducer performance

Transducer characterisation

The electrical impedance magnitude / phase spectra of the three transducers, each fabricated using a different single crystal composition, were measured in water using the impedance analyser. The results, along with the corresponding PiezoCAD simulation output, are shown in Figure 5.2. At the designed operating frequency of 18 MHz, the electrical impedance magnitudes of the Sm:PIN-PMN-PT, PIN-PMN-PT, and PMN-PT transducers are around 44, 50, and 45 Ω, respectively, in reasonable agreement with the impedance requirement of standard 50 Ω US imaging analogue

front end circuitry. Simulated and measured results agreed well. The thickness mode resonance frequencies, f_r, are located at 14.3 MHz, 14.7 MHz, and 14.9 MHz, respectively and the anti-resonance frequencies, f_a, are at 26.7 MHz, 22 MHz, and 24 MHz, respectively. The k_{eff} values are estimated to be 0.84, 0.74, and 0.78, respectively.

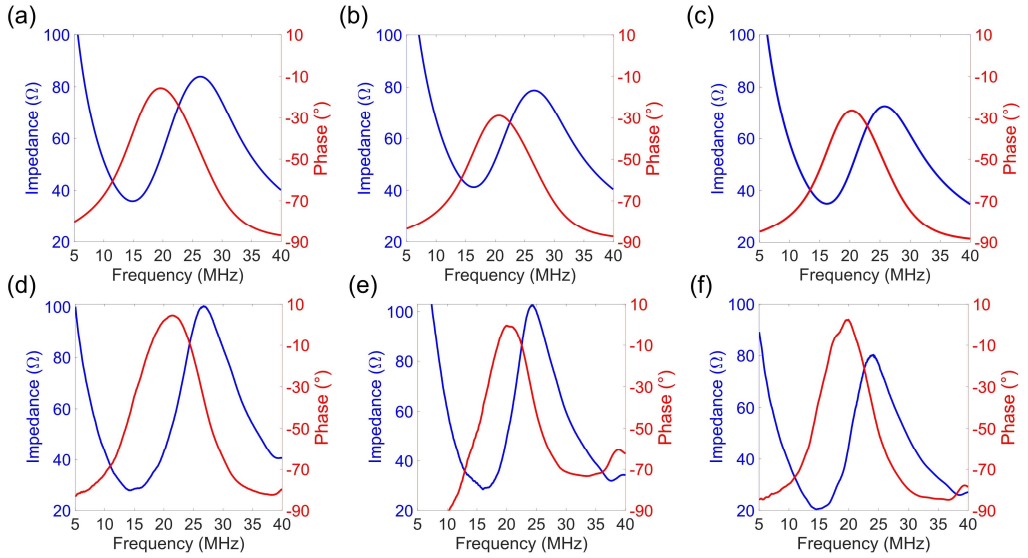

Figure 5.2 (a–c) Simulated and (d–f) measured impedance / phase spectra of Sm:PIN-PMN-PT, PIN-PMN-PT and PMN-PT 1-3 piezocomposite transducers.

The two-way IL was evaluated for each transducer over a frequency range, $5 < f < 28$ MHz. The characterisation method was introduced in Section 3.5.4. Figure 5.3 shows the measured two-way ILs. The lowest ILs of the Sm:PIN-PMN-PT, PIN-PMN-PT and PMN-PT transducers were observed to be 14.6 dB, 16.0 dB, and 16.9 dB at 18 MHz, 17 MHz, and 18 MHz, respectively. The transducers fabricated in this study, particularly with Sm:PIN-PMN-PT, exhibited better performance than other reported 1-3 composite-based devices [100], [133], [141], [142], owing to their exceptionally high piezoelectric and coupling coefficients.

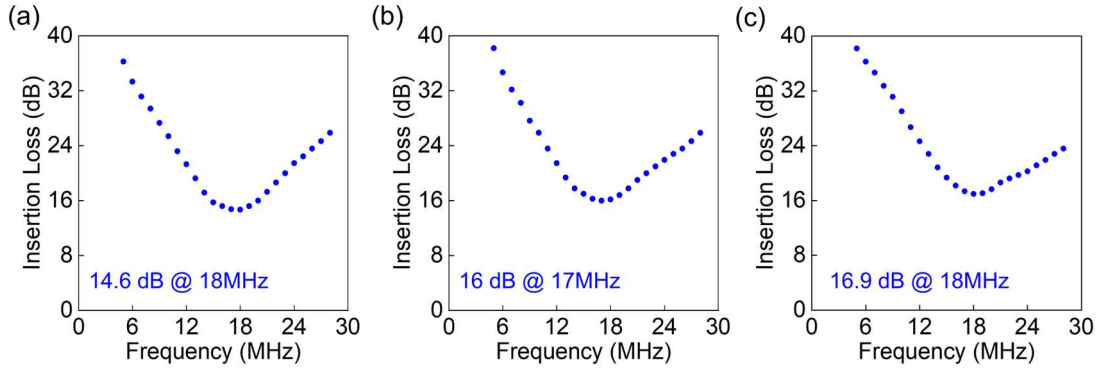

Figure 5.3 Two-way ILs of (a) Sm:PIN-PMN-PT, (b) PIN-PMN-PT, and (c) PMN-PT 1-3 composite transducers.

The pulse-echo method was used to measure f_c for each transducer and its -6 dB bandwidth, using the equations as follows [168] :

$$f_c = \frac{f_1 + f_2}{2} \quad \text{Eq. 5.1}$$

$$BW = \frac{f_2 - f_1}{f_c} \times 100\% \quad \text{Eq. 5.2}$$

where f_1 and f_2 are the two cutoff frequencies at -6 dB. The performance of the transducers was measured using the system introduced in Section 3.5.2. According to Eq.3.9, a quartz plate was positioned at 13 mm below the transducer to maximise the reflected echo energy.

The simulated and measured pulse-echo results are shown in Figure 5.4. The original, simulated f_c of the transducers was 20 MHz, whereas the measured centre frequencies of the Sm:PIN-PMN-PT, PIN-PMN-PT, and PMN-PT transducers were 15.7 MHz, 15.1 MHz, and 15.4 MHz, respectively, with corresponding -6 dB bandwidths of 73%, 67%, and 71%. The variation between the simulated and measured centre frequencies is attributed to the damping effect of the passive matching layer material.

The peak-to-peak amplitude of the echo signal for the PMN-PT transducer in Figure 5.4(e) is lower than that of the other two because the transducer experienced partial depolarisation due to the long-term high-voltage (100 V) excitation of the applied pulse during pulse-echo testing and its inherently low coercive field. A re-poling process was conducted to restore its functionality, but its performance did not fully recover to its original state.

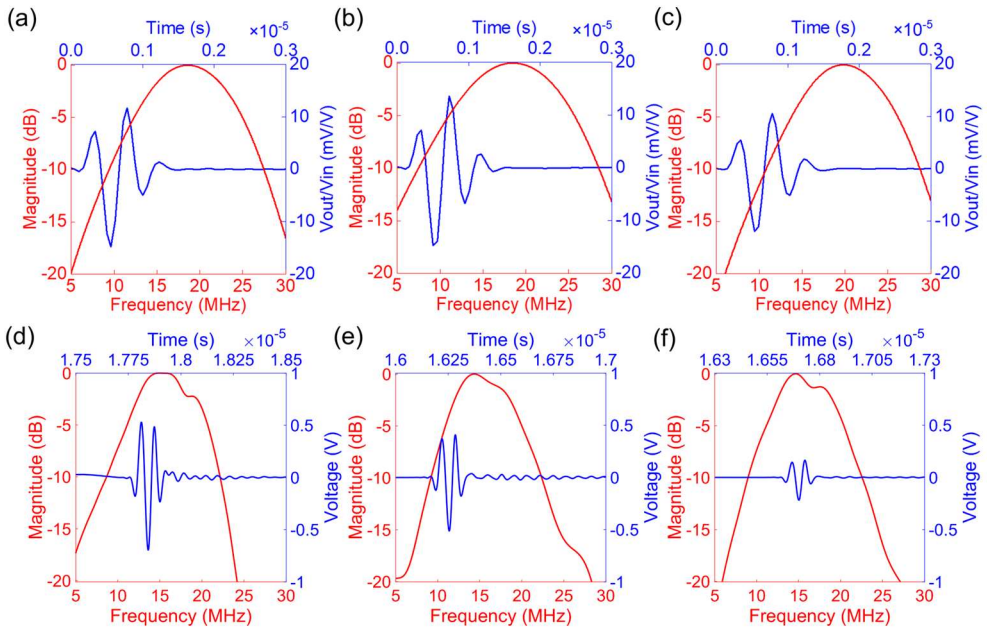

Figure 5.4 (a–c) Simulated and (d–f) measured pulse-echo responses of Sm:PIN-PMN-PT, PIN-PMN-PT, and PMN-PT 1-3 composite transducers.

Transducer imaging performance evaluation

The resolution of the transducers was assessed by scanning the wire phantom described in Section 3.5.3. Resolution values were calculated directly from the specific wire targets enclosed by red ellipses in Figure 5.5(a), (d) and (g). The theoretical lateral resolution, R_{lateral} = 530 μm, and the experimental resolutions evaluated with the wire phantom for the Sm:PIN-PMN-PT, PIN-PMN-PT and PMN-PT transducers are 545 μm, 558 μm, and 629 μm, respectively, as shown in Figures 5.5(b), (e), and (h). The relatively lower lateral resolution, in comparison to other transducers with similar operating frequencies [69], [75], [126], is related to the enlarged aperture, which was intentionally designed to improve electrical impedance matching with a 50-ohm system and an unfocused transducer surface. In general, a broad bandwidth results in a shorter pulse duration, thereby improving axial resolution [169]. The theoretical axial resolutions for Sm:PIN-PMN-PT, PIN-PMN-PT, and PMN-PT transducers are 65 μm, 74 μm, and 69 μm, respectively, and the measured values are 69 μm, 75 μm, and 71 μm from Figures 5.5(c), (f), and (i).

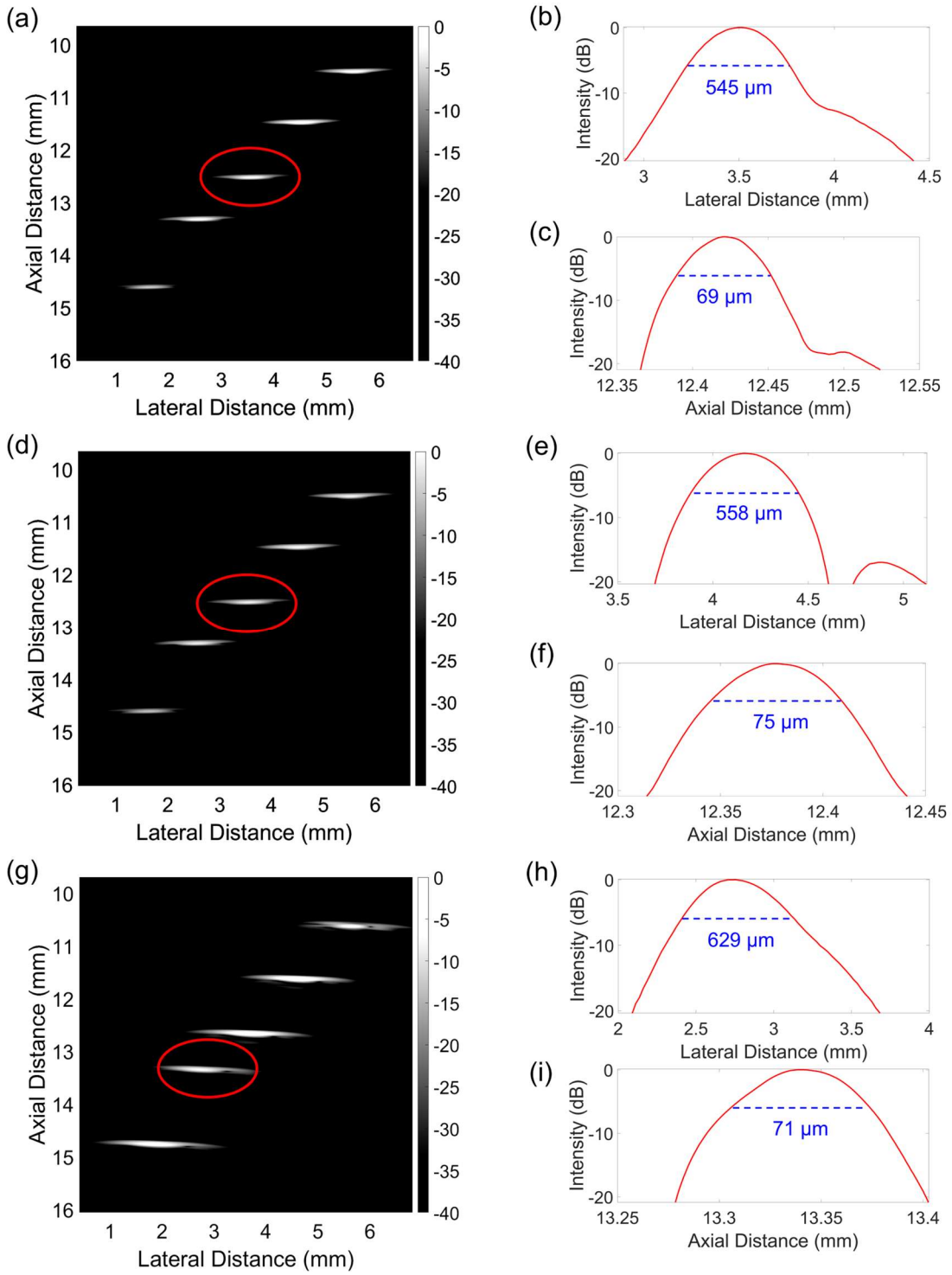

Figure 5.5 (a) The wire phantom image, (b) the measured lateral resolution, and (c) the measured axial resolution for the Sm:PIN-PMN-PT transducer. (d) The wire phantom image, (e) the measured lateral resolution, and (f) the measured axial resolution for the PIN-PMN-PT transducer. (g) The wire phantom image, (h) the measured lateral resolution, and (i) the measured axial resolution obtained for the PMN-PT transducer.

Both lateral and axial theoretical resolutions show excellent agreement with measured values, except for the lateral resolution of the PMN-PT transducer. The primary reason

for the mismatch is the depolarisation and repolarisation processes of the material during experiments, because of its lower E_c, leading to overall performance degradation of the transducer and significantly compromising the lateral resolution.

5.4.3 *Ex vivo* imaging

Following the wire phantom measurements, *ex vivo* imaging tests were conducted using a piece of porcine belly, as shown in Figure 5.6(a), to demonstrate the imaging performance of the fabricated transducers. The specimen was submerged in DI water and kept in a 3D-printed 20 mm × 20 mm × 20 mm open-top PLA box. A photograph of the specimen with the scanned area is shown in Figure 5.6(a). The scanning procedures and equipment used were identical to those employed for the wire phantom imaging.

In Figures 5.6(b–d), the boundaries of the skin layer, S1, and the lean tissue layer, L1, can be clearly differentiated for all three transducers. Little speckle is observed in the fat layer, F1, due to the attenuation and scattering from the overlying layers and the nature of fat having lower echogenicity. The Sm:PIN-PMN-PT and PIN-PMN-PT transducers exhibit higher intensities from S1, whereas the PMN-PT transducer shows lower intensity, consistent with the depolarisation noted previously.

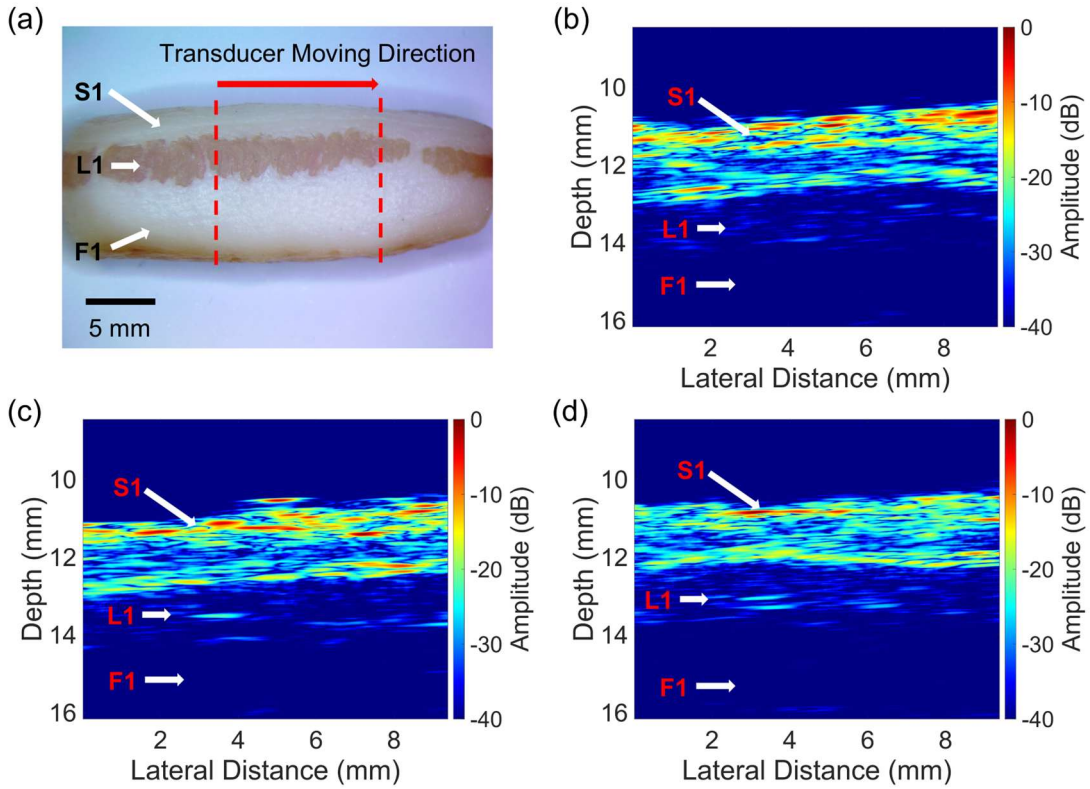

Figure 5.6 (a) Photograph of a section of *ex vivo* porcine belly and B-mode image using the (b) Sm:PIN-PMN-PT transducer, (c) the PIN-PMN-PT transducer, and (d) the PMN-PT transducer. (Dynamic range: 40 dB, S1: skin layer, L1: lean tissue layer, F1: fat layer.)

5.5 Array transducer

5.5.1 Design and fabrication

The 1D linear array transducer was designed and fabricated following the process detailed in Section 3.4.2. It has three main components: an active piezoelectric layer, double matching layers that are a mixture of 2–3 µm silver powder and Epo-tek 301, and a backing layer of 9 µm alumina powder in Epo-tek 301. The material properties of each layer are summarised in Table 5.3, and the design parameters of the array are listed in Table 5.4. Figure 5.7 provides a photo of the fabricated array and outlines its structure.

Table 5.3 Acoustic design parameters for material layers.

Layer	Material	Thickness (mm)	Acoustic Impedance (MRayl)
Active layer	Sm:PIN-PMN-PT single crystal	0.10	~31.50
1st matching layer	2–3 µm silver powder and Epo-tek 301	0.03	~6.07
2nd Matching layer	Parylene C [170]	0.03	~2.70
Backing layer	9 µm alumina powder and Epo-tek 301	5.00	~7.20

Table 5.4 Design parameters for a 1D linear array transducers.

Specifications	Values
Designed f_c	15 MHz
Element width	88 µm
Kerf width	12 µm
Pitch	100 µm
Elevation dimension	5 mm
Number of elements	64
Area	6.4 mm x 5 mm

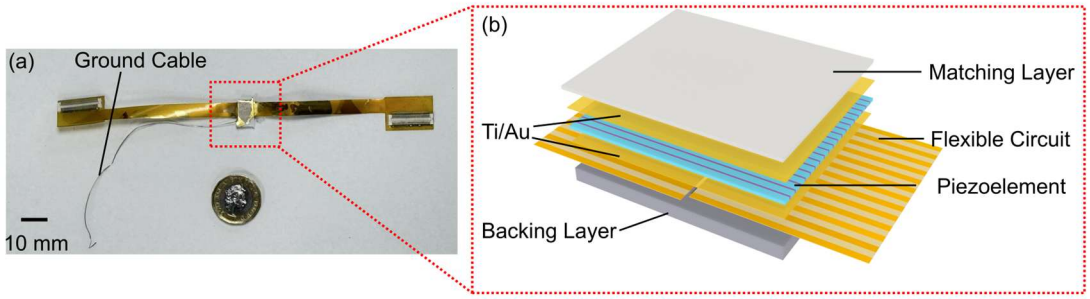

Figure 5.7 (a) Photograph of the transducer with a UK £1 coin and (b) Schematic of the transducer structure. The transducer includes electrical connections to the Verasonics Vantage 128 research US system.

5.5.2 Array performance

Impedance magnitude / phase spectra

Following Section 3.5.1, impedance measurements were first performed in DI water to verify the electrical connection of the array elements. Three elements did not exhibit proper impedance curves, likely due to incomplete bonding between the elements and the flexible circuits. Figure 5.8 shows the simulation results and the measured spectra of the 17th element, chosen as a typical element.

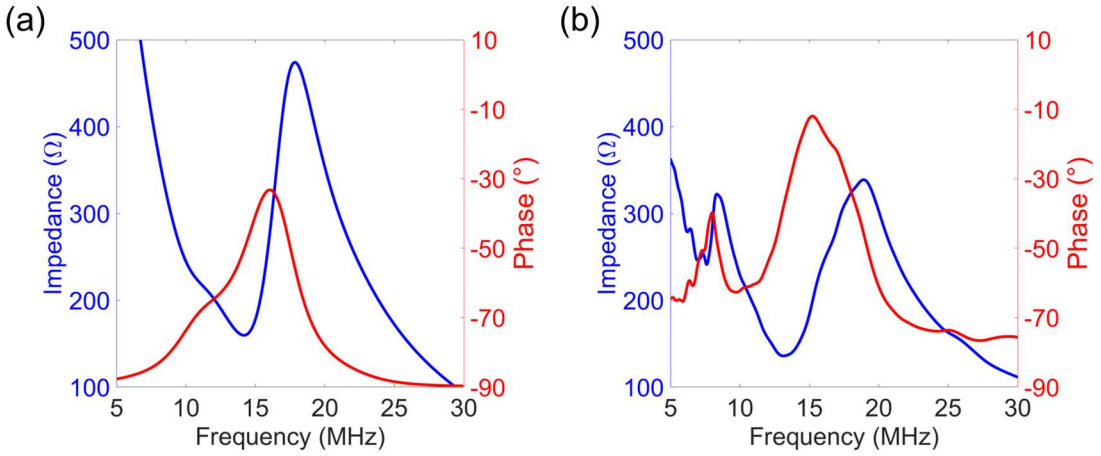

Figure 5.8 (a) Simulated and (b) measured electrical impedance magnitude / phase spectra of the 17th element.

The measured resonance and anti-resonance frequencies demonstrate agreement with the simulated results. However, the observed magnitude at the anti-resonance frequency is lower than the simulated value. This discrepancy is attributed to differences in boundary conditions and loss mechanisms. Specifically, the passive layers in the physical device dampen the vibration intensity. Furthermore, the experimental measurements inherently include mechanical losses that were not accounted for in the simulation.

Additionally, a weaker resonance is visible around 7 MHz. This arises from a lateral vibration mode of the array element. As this feature lies outside the operational bandwidth of the longitudinal mode, it does not affect the device performance. The average resonance frequency was approximately 13.2 MHz, while the anti-resonance frequency was around 17.8 MHz. k_{eff} was estimated in accordance with Equation 3.6, and the average k_{eff} was found to be 0.67. Figure 5.9 illustrates the values of impedance magnitude and phase extracted from impedance magnitude / phase spectra for all 61 functioning elements at 15 MHz. The values of the representative 17th element are

marked. Data from three unconnected elements were excluded from these plots. The 57th and 58th elements demonstrate abnormally low impedance magnitudes due to a parallel-circuit connection that occurred during the fPCB bonding procedure.

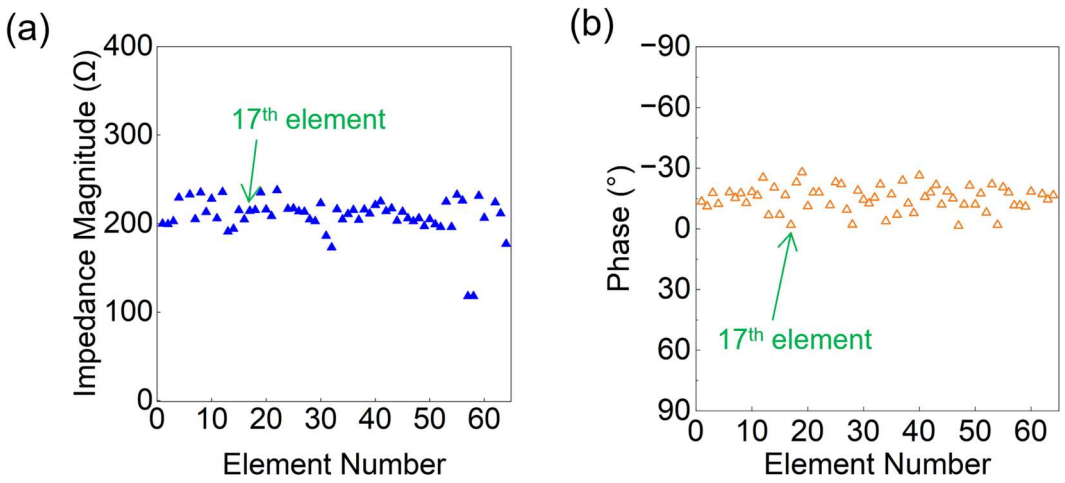

Figure 5.9 Measured electrical impedance magnitude / phase values of 61 elements.

Insertion loss and crosstalk

Two-way IL measurement was conducted on the 17th element following the protocol outlined in Section 3.5.4. A 5-cycle burst excitation with 5 V peak-to-peak voltage was applied across a frequency range of 5 to 25 MHz in steps of 1 MHz using the function generator. The resulting IL spectrum is plotted in Figure 5.10, where the minimum loss was observed to be 25.9 dB at 15 MHz.

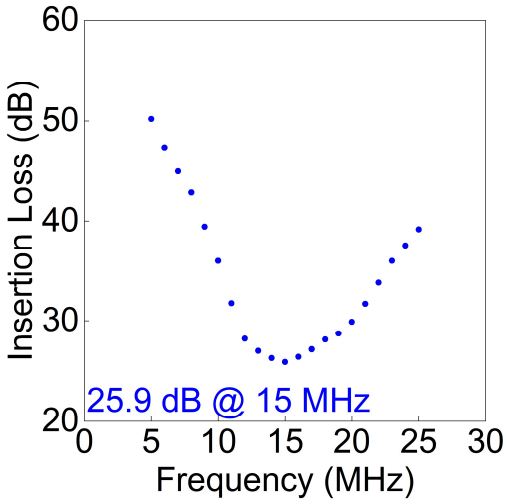

Figure 5.10 Two-way IL of Sm:PIN-PMN-PT array from the 17th element.

The array fabricated incorporating Sm:PIN-PMN-PT single crystal exhibits better performance than other reported array in Table 5.5 because of its high piezoelectric coefficients and energy conversion ability.

Table 5.5 Comparison of sensitivity of array transducers.

Transducer active material	IL (dB)
PMN-0.28PT single crystal [171]	43
KNLNTS lead-free ceramic [172]	41.8
PZT/epoxy 2–2 composite [173]	33.9
PMN-0.30PT single crystal [174]	29
Sm:PIN-PMN-PT single crystal (This work)	25.9

Crosstalk was characterised following the protocol outlined in Section 3.5.6. A 10 V_{pp} excitation signal at 15 MHz was applied to the 17th element using the function generator. The induced voltage amplitude on the adjacent element was then recorded via an oscilloscope. The measured crosstalk levels are at approximately −24 dB, an elevated value due to common ground configuration. The design of the flexible circuit can be further optimised to mitigate crosstalk by minimising the overall length of the circuit to reduce parasitic inductance (L) and C. Furthermore, introducing interstitial ground traces between the active element lines as electrical shielding may further significantly reduce signal interference between adjacent channels.

Consistency check

To evaluate the consistency of the fabricated array, the impedance analyser was used to measure C at 10 kHz for each element. Figure 5.11 presents the distributions of the C across the array elements.

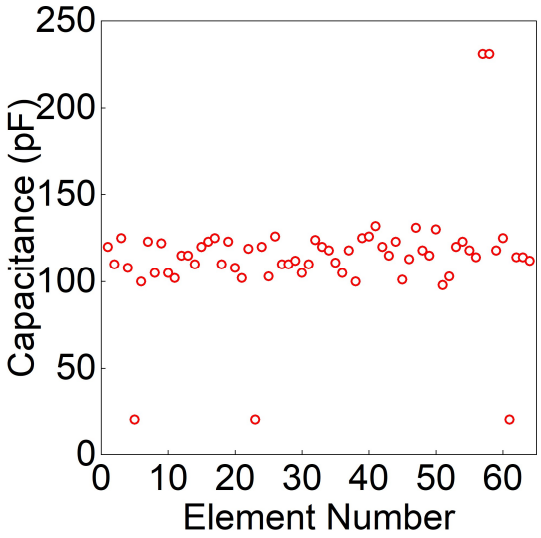

Figure 5.11 The measured capacitances of all 64 elements.

The three elements with improper impedance curves displayed very low C values, suggesting open circuits at the interconnect interface. The other 61 elements exhibited a mean capacitance of 118.82 pF and a standard deviation of 24.50 pF. The 57th and 58th elements exhibit a combined capacitance equal to the sum of the two individual elements due to a parallel electrical connection during fabrication. Consequently, five elements did not meet the criterion for independent operation, corresponding to a functional-element yield of 92.2%. The affected elements were distributed across the aperture and did not form a large continuous inactive region, thereby limiting their expected influence on beamforming.

Despite these defects, the remaining independently functional elements enabled successful reconstruction of B-scan images in the *ex vivo* experiment described in Section 5.5.3, in which the target structures remained clearly identifiable. Previous high-frequency array studies have similarly demonstrated prototype functionality through phantom or biological imaging despite the presence of open, shorted or low-sensitivity elements [175], [176], [177]. The array was therefore considered adequate for proof-of-concept imaging, although improved bonding control and edge protection will be required to increase fabrication consistency.

Pulse-echo measurement

Further acoustic characterisation was carried out using the pulse-echo method to determine the f_c and the -6 dB bandwidth, calculated according to Equations 4.1 and 4.2.

The array was immersed in DI water at room temperature and positioned perpendicular to a quartz block at a distance of 10 mm from the transducer. The functional array elements were excited by the US pulser/receiver with a pulse delivering 1.55 μJ of energy and a 48.7 Ω damping resistance. Figure 5.12 presents the simulated and measured responses in the time and frequency domains of the 17th element and the distribution of f_c and -6 dB bandwidth of all 64 elements.

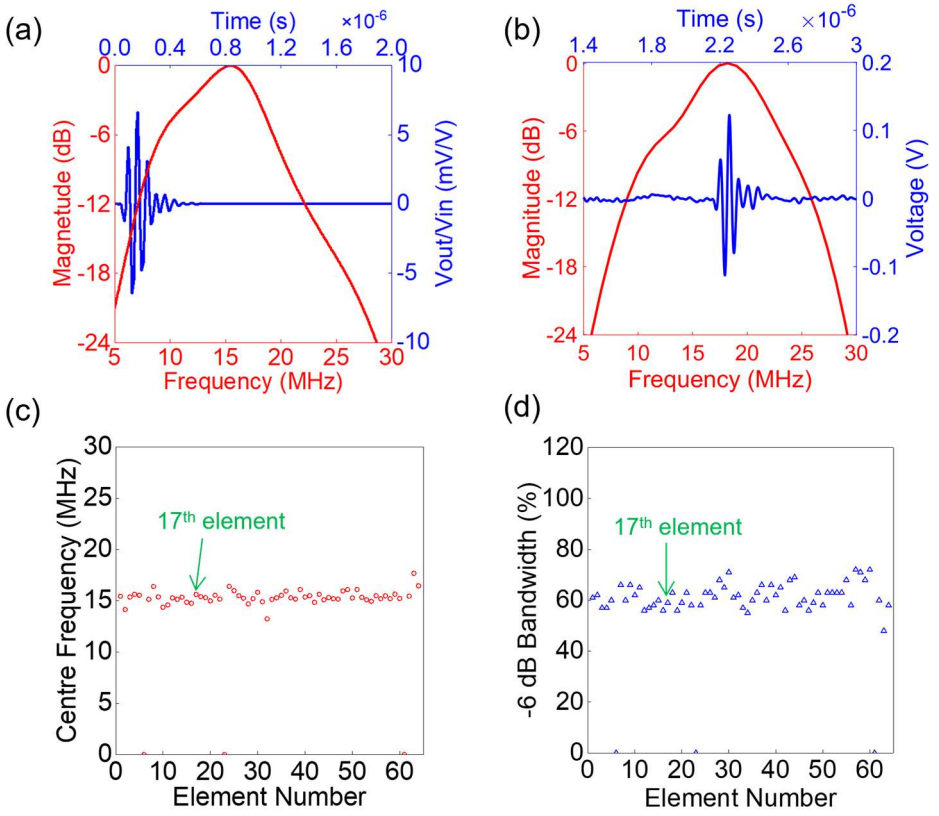

Figure 5.12 Simulated (a) and measured (b) pulse-echo response of the 17th element. Measured (c) f_c and (d) -6 dB bandwidth for all 64 elements.

For all functional elements, the average f_c was 15.4 MHz, which aligns well with the design target of 15 MHz. The average -6 dB bandwidth was measured to be 62%. This bandwidth is good for an array transducer utilising a 2-2 composite configuration. However, by transitioning to a 1-3 composite configuration and incorporating a centrifuged backing layer to increase acoustic damping, the -6 dB bandwidth could be further improved.

Spatial Resolution

The spatial resolution of the fabricated array transducer was evaluated using the wire phantom submerged in DI water described in Section 3.5.3. Figure 5.13 illustrates the experimental setup, in which the array elements were interfaced with the Verasonics

Vantage 128 research US system via a customised interposer (Shenchao, Shenzhen, China).

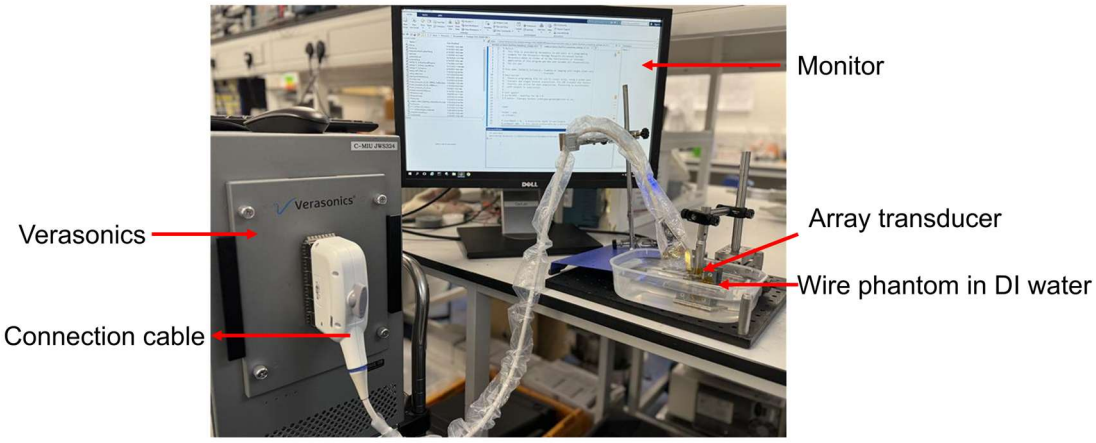

Figure 5.13 Experiment setup for measuring the phantom for resolution measurement.

During the measurement, all elements were excited with a drive voltage of 30 V, and the full aperture was utilised to receive the returning echoes for image reconstruction. A dead zone of approximately 1 mm is evident in Figure 5.14 due to pulse ring-down. The resulting image clearly resolves the positions of the four target wires with a diameter of 20 µm. However, artefacts are also visible in the surrounding regions, which can be attributed to side lobes and inter-element crosstalk.

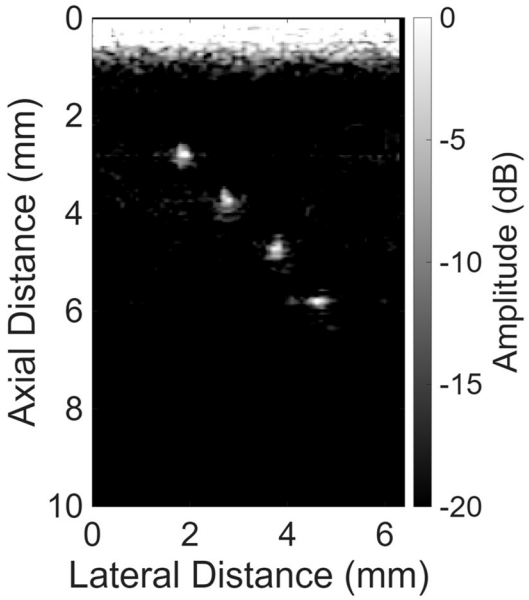

Figure 5.14 Wire phantom image from the fabricated array.

Figure 5.15 illustrates the corresponding intensity profiles of the wires. The axial and lateral resolutions were quantified using the line spread function derived from the 3rd wire target from the top. The measured values were 119 µm for axial resolution and 285 µm for lateral resolution.

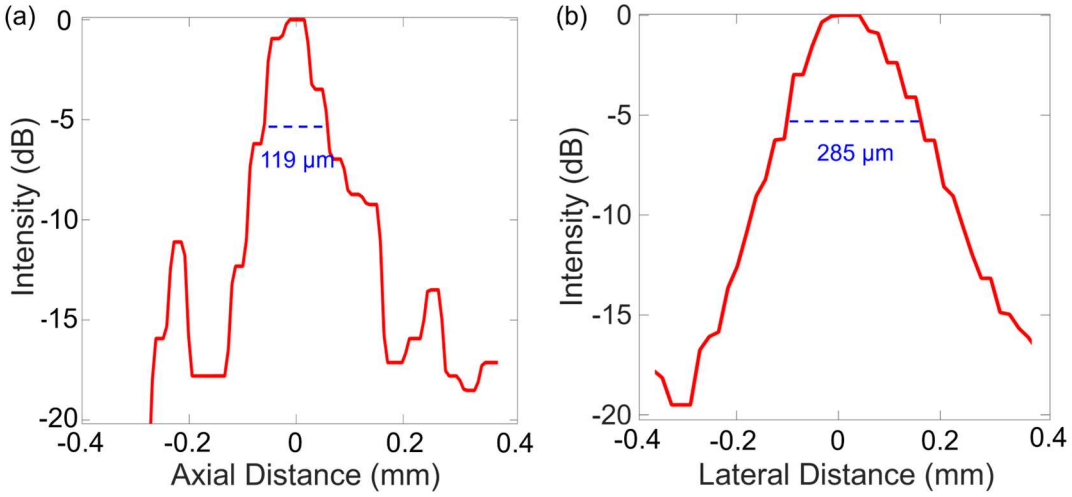

Figure 5.15 (a) The measured lateral resolution and (b) the measured axial resolution for the array.

5.5.3 *Ex vivo* imaging

Following the spatial resolution characterisation, *ex vivo* imaging was performed using a porcine belly specimen. The sample was submerged in DI water in a custom 3D-printed PLA container with dimensions of 50 mm × 50 mm × 20 mm. To evaluate image performance, a tungsten wire with a diameter of 50 µm was inserted into the tissue. For this experiment, the array was excited with a 30 V_{pp} and 20 dB gain using the Verasonics system. As illustrated in Figure 5.16, the tissue surface is visible approximately 4 mm from the array face, and the embedded tungsten wire is clearly distinguishable at a depth of ~7.5 mm. Overall, the signal intensity from the surrounding tissue decreases with depth due to the scattering and attenuation of the US energy.

Given that the SNR is related to the penetration depth, and considering that the region of interest in US imaging system typically lies within a depth range of 6 – 12 mm [88], the region of interest for the SNR calculation was selected at a depth of approximately 6 mm. The noise was established using the root mean square (RMS) values from an anechoic region, yielding a measured SNR for the wire in porcine tissue exceeding 40 dB using Equation 3.12.

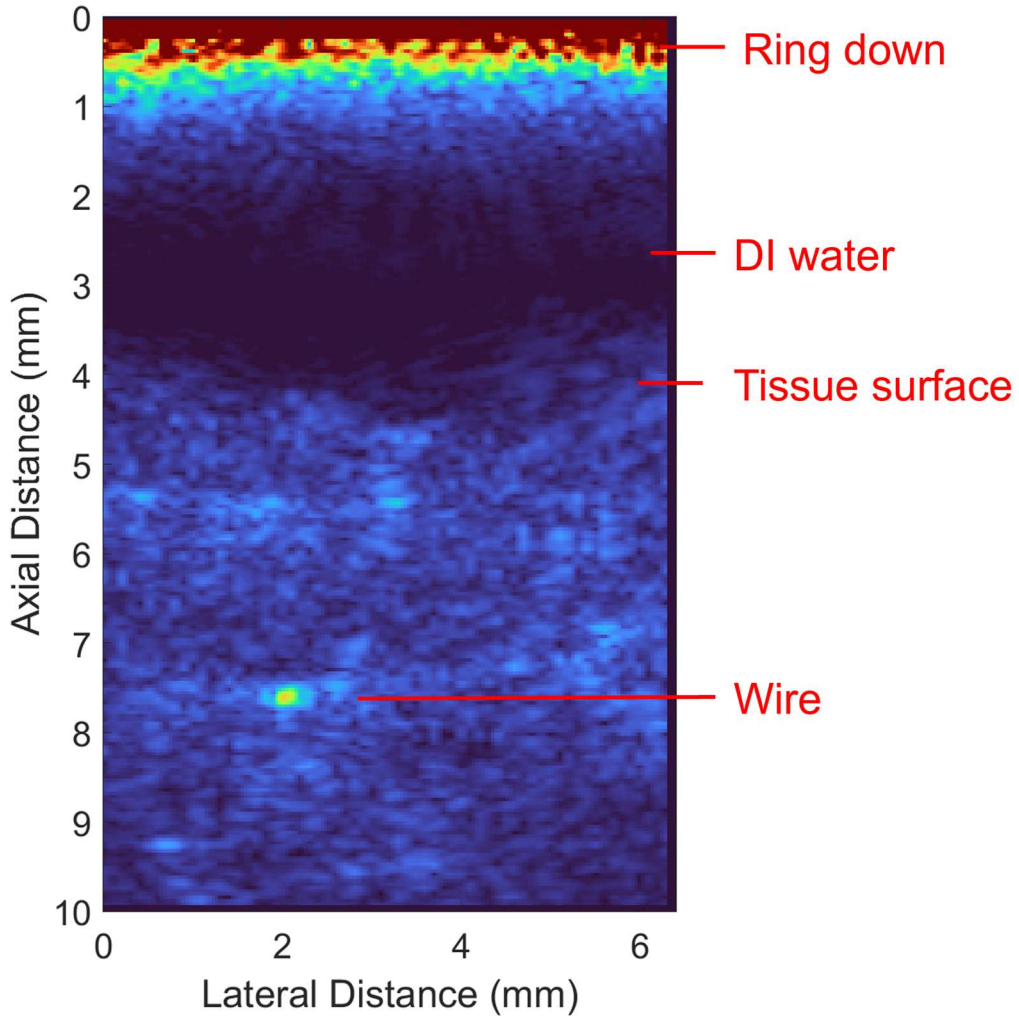

Figure 5.16 B-mode image using the fabricated Sm:PIN-PMN-PT array transducer. (40 dB dynamic range)

In practical clinical applications, the diagnostic value of the image can be further refined by adjusting gain settings, transducer alignment, and display contrast. Additionally, the application of standard image processing algorithms enables optimisation of the SNR ratio in the final visual output [3].

5.3 Conclusions

The first part of this chapter compared Sm:PIN-PMN-PT, PIN-PMN-PT and PMN-PT 1-3 piezocomposite US transducers to evaluate their imaging performance. Among these materials, Sm:PIN-PMN-PT demonstrated enhanced stability and superior performance, particularly in piezoelectric properties, electromechanical coupling, and sensitivity. This transducer also exhibited excellent bandwidth, sensitivity and imaging resolution. The performance of the PIN-PMN-PT transducer was quite similar, offering comparable but slightly inferior results. However, the PMN-PT transducer,

while exhibiting promising results initially, suffered depolarisation during long-term operation, consistent with its theoretical low E_c. Despite this limitation, it remained potential functional for imaging.

Overall, the Sm:PIN-PMN-PT transducer offered the best performance among the three transducers, achieving k_{eff} of 0.84 and a bandwidth of 73%, resulting in extremely low IL of 14.6 dB and an axial resolution of 69 μm. This makes the Sm:PIN-PMN-PT single crystal an excellent candidate for US biomedical imaging. This finding also establishes a solid foundation for future work in developing high-performance US transducers for MSCRs and a wide range of other medical diagnostic applications.

The second part of this chapter presented the development and characterisation of a 15MHz 1D linear array utilising Sm:PIN-PMN-PT single crystal. To enhance energy conversion efficiency, the device employed sub-diced elements to form a 2-2 composite configuration. Notably, this study marks the first application of Sm:PIN-PMN-PT single-crystal material in a high-frequency array. The investigation determined the material properties and array functional performance, including impedance magnitude and phase spectra, pulse-echo response, spatial resolution and *ex vivo* tissue imaging.

The device exhibited an IL of 25.9 dB and an average -6 dB bandwidth of 62%, results that confirm the performance of the Sm:PIN-PMN-PT single crystal. Furthermore, k_{eff} was 0.67 and with a measured SNR ratio exceeding 40 dB for a wire target, this array appears to be a good candidate for biomedical US applications, specifically for integration with MSCRs.

Future work will implement miniaturised arrays to comply with the dimensional constraints of the MSCR platform. The proposed array design has 10 elements of length 1 mm with a pitch maintained at 100 μm. This specific geometry restricts the total array area to the exact size of the single-element device, corresponding to a negligible mechanical payload on the MSCR. Furthermore, an embedded serial communication chip positioned within the distal tentacle will transmit the acoustic data. Preliminary simulations of the array predict an electrical impedance magnitude of 625 Ω at a centre frequency of 15 MHz. The array delivers a simulated bandwidth of 45%. These quantitative results confirm the acoustic and mechanical viability of the proposed array integration.

Chapter 6 Conclusions and future work

6.1 Conclusions

This thesis has established a novel platform for intracorporeal imaging by successfully integrating high-frequency US transducers with MSCRs. Motivated by the limitations of rigid surgical imaging tools for accessing complex anatomical regions, this research aimed to validate proof-of-concept for a steerable, soft robotic imaging platform. The work presented covers both MSCRs and high-frequency miniature US transducers. System viability was demonstrated through material characterisation, device fabrication, bench testing, and *ex vivo* and *in vivo* validation.

The primary contribution of this research lies in the development of a functional imaging payload compatible with the MSCRs. 15 MHz single-element transducers with 1-3 composite PIN-PMN-PT single crystals were designed and fabricated. The integration process confirmed that the transducer payload did not significantly compromise the MSCR's deflection capabilities, preserving its navigational agility. Through a progression of sensing modes, ranging from lateral proximity sensing to axial sweep scanning, the system demonstrated its ability to resolve structural details in silicon phantoms.

Another advancement was the execution of rotational scanning. In ideal *ex vivo* conditions, the system achieved a 120-degree scanning range with good-quality ultrasonic imaging. The subsequent *in vivo* trials in a porcine model provided the first empirical evidence of the clinical viability of the platform. However, these trials also revealed specific challenges inherent in realistic physiological environments. Notably, the high compliance of the MSCR limited its ability to rotate effectively within narrow anatomical spaces, and the imaging quality was partially constrained by the absence of a delivery mechanism for an acoustic coupling medium in more open anatomy.

This thesis also advanced the material foundation for miniature US devices by exploring the performance of a single-crystal material with Sm doping. The investigation of Sm:PIN-PMN-PT revealed somewhat superior electromechanical properties compared to those of conventional materials. The fabrication and characterisation of both single-element 1-3 composite transducers and a 1D linear array with 2-2 composite (sub-diced) elements demonstrated that the new material

yields higher sensitivity. These findings establish Sm:PIN-PMN-PT single crystal transducers and array as candidates for next-generation biomedical imaging platforms, particularly when integrated into MSCRs.

In summary, this research has established a proof of concept for an US-integrated MSCR platform. By combining the flexibility of MSCRs with the high-resolution imaging capability of piezoelectric transducers simulating the potential performance of an integrated array, this work confirms the feasibility of developing future minimally invasive interventions that require both precise navigation and real-time anatomical visualisation.

6.2 Future work

Based on the findings of this study, future research should primarily focus on optimising and advancing US transducers to improve their compatibility with the MSCR platform. This development can be categorised into three key areas: performance improvement of high-frequency single-element transducers, further steps towards an array for integration and better imaging, and co-design of MSCRs to complement the US capabilities.

Acoustic and electronic optimisation of single-element transducers

Regarding material composition, the empirical findings detailed in Chapter 5 demonstrate that the Sm:PIN-PMN-PT single crystal transducer has a larger bandwidth and acoustic sensitivity compared with the conventional PIN-PMN-PT single crystal currently utilised in MSCRs. Consequently, future transducer iterations should incorporate this Sm-doped single crystal to maximise acoustic performance.

Regarding electronic infrastructure, the current data acquisition system consists of a pulser-receiver coupled with a programmed oscilloscope. An increase in the mechanical rotation speed of the robotic arm will outpace the data-saving capabilities of the oscilloscope. To resolve this limitation, future systems will integrate miniaturised high-speed US front-end chips. Shifting to ASICs or FPGA modules enables rapid on-board signal processing alongside high pulse repetition frequencies. This electronic miniaturisation follows a well-established translational paradigm

ensuring that optimal image resolution is maintained even at elevated mechanical scanning speeds.

Advancing array configurations for MSCR integration

To further optimise the system for clinical application, future work will focus on miniaturisation and mechanical integration. The current array comprising 64 elements and occupies a surface area exceeding 6.4 mm × 5.0 mm. Subsequent designs will utilise a reduced configuration of 10 elements featuring a pitch of 100 μm or less. Additionally, the grounding scheme will be integrated directly into the flexible circuit as a single trace to save space. This compact configuration should enable versatile spatial positioning, allowing both lateral and forward-looking imaging modalities. Ultimately, the inherent electronic scanning capability of the array will eliminate the necessity for mechanical sweeping mechanisms and consequently simplify the control architecture of the robot.

Optimisation of the US-integrated MSCR system

The current study focused on the performance characterisation of the US transducers, and kinematic evaluation of the robotic arm remains insufficient. The dynamic control mapping between the MSCR rotation angle and the corresponding robotic arm actuation demands thorough investigation. Future work should utilise the EPM system to achieve precise angular control of the MSCR. A primary objective is to enable a fully automatic 360-degree rotational scan in complex anatomical environments. This advanced capability will surpass the current operational limit of 120 degrees previously achieved under idealised experimental setups.

Additionally, while this thesis focused on rotational scanning, the performance of axial scanning driven by active tip deflection requires further characterisation. The *in vivo* trial has demonstrated that the absence of an acoustic coupling medium within real tissue environments severely restricts US propagation. Therefore, a dedicated channel or tool will be made to deliver US couplant around the target site.

References

[1] Y. Wang, K.-H. Lam, and S. Cochran, 'High-sensitivity Sm:PIN-PMN-PT ultrasound transducer for biomedical imaging applications', *Appl. Phys. Lett.*, vol. 127, no. 6, p. 063704, Aug. 2025, doi: 10.1063/5.0284003.

[2] H. S. Allen, 'X-Rays and their Applications', *Nature*, vol. 127, no. 3201, pp. 356–358, Mar. 1931, doi: 10.1038/127356a0.

[3] T. L. Szabo, *Diagnostic Ultrasound Imaging: Inside Out*. Amsterdam Boston: Academic Press, 2014.

[4] R.-J. M. van Geuns *et al.*, 'Basic principles of magnetic resonance imaging', *Prog. Cardiovasc. Dis.*, vol. 42, no. 2, pp. 149–156, Sep. 1999, doi: 10.1016/S0033-0620(99)70014-9.

[5] A. Ella *et al.*, 'The development of brain magnetic resonance approaches in large animal models for preclinical research', *Anim. Front.*, vol. 9, no. 3, pp. 44–51, Jun. 2019, doi: 10.1093/af/vfz024.

[6] A. Saleh, M. Schroeter, C. Jonkmanns, H. Hartung, U. Mödder, and S. Jander, 'In vivo MRI of brain inflammation in human ischaemic stroke', *Brain*, vol. 127, no. 7, pp. 1670–1677, Jul. 2004, doi: 10.1093/brain/awh191.

[7] G. Thomalla *et al.*, 'MRI-Guided Thrombolysis for Stroke with Unknown Time of Onset', *N. Engl. J. Med.*, vol. 379, no. 7, pp. 611–622, Aug. 2018, doi: 10.1056/NEJMoa1804355.

[8] G. H. Glover, 'Overview of functional magnetic resonance imaging', *Neurosurg. Clin. N. Am.*, vol. 22, no. 2, pp. 133–139, vii, Apr. 2011, doi: 10.1016/j.nec.2010.11.001.

[9] R. G. González, G. S. Silva, J. He, S. Sadaghiani, O. Wu, and A. B. Singhal, 'Identifying Severe Stroke Patients Likely to Benefit From Thrombectomy Despite Delays of up to a Day', *Sci. Rep.*, vol. 10, no. 1, p. 4008, Mar. 2020, doi: 10.1038/s41598-020-60933-3.

[10] M. Prokop, 'General principles of MDCT', *Eur. J. Radiol.*, vol. 45 Suppl 1, pp. S4-10, Mar. 2003, doi: 10.1016/s0720-048x(02)00358-3.

[11] C. H. McCollough and P. S. Rajiah, 'Milestones in CT: Past, Present, and Future', *Radiology*, vol. 309, no. 1, p. e230803, Oct. 2023, doi: 10.1148/radiol.230803.

[12] J. Ghajar, 'Traumatic brain injury', *The Lancet*, vol. 356, no. 9233, pp. 923–929, Sep. 2000, doi: 10.1016/S0140-6736(00)02689-1.

[13] W. Zhang *et al.*, 'The study of plain CT combined with contrast-enhanced CT-based models in predicting malignancy of solitary solid pulmonary nodules', *Sci. Rep.*, vol. 14, no. 1, p. 21871, Sep. 2024, doi: 10.1038/s41598-024-72592-9.

[14] C. I. Henschke, D. F. Yankelevitz, R. Mirtcheva, G. McGuinness, D. McCauley, and O. S. Miettinen, 'CT Screening for Lung Cancer', *Am. J. Roentgenol.*, vol. 178, no. 5, pp. 1053–1057, May 2002, doi: 10.2214/ajr.178.5.1781053.

[15] J. A. Soto and S. W. Anderson, 'Multidetector CT of Blunt Abdominal Trauma', *Radiology*, vol. 265, no. 3, pp. 678–693, Dec. 2012, doi: 10.1148/radiol.12120354.

[16] J. P. Vaccaro and J. M. Brody, 'CT Cystography in the Evaluation of Major Bladder Trauma', *RadioGraphics*, vol. 20, no. 5, pp. 1373–1381, Sep. 2000, doi: 10.1148/radiographics.20.5.g00se111373.

[17] M. P. Federle, H. I. Goldberg, J. A. Kaiser, A. A. Moss, R. B. Jeffrey, and J. C. Mall, 'Evaluation of abdominal trauma by computed tomography.', *Radiology*, vol. 138, no. 3, pp. 637–644, Mar. 1981, doi: 10.1148/radiology.138.3.6450962.

[18] D. Nam, R. L. Barrack, and H. G. Potter, 'What Are the Advantages and Disadvantages of Imaging Modalities to Diagnose Wear-related Corrosion

Problems?', *Clin. Orthop. Relat. Res.*, vol. 472, no. 12, p. 3665, Dec. 2014, doi: 10.1007/s11999-014-3579-9.
[19] A. Boonruang, 'Fabrication and characterisation of microultrasound array transducers', PhD, University of Glasgow, 2021. doi: 10.5525/gla.thesis.82631.
[20] I. Velikyan, 'Prospective of ^{68}Ga-Radiopharmaceutical Development', *Theranostics*, vol. 4, no. 1, pp. 47–80, Dec. 2013, doi: 10.7150/thno.7447.
[21] S. R. Cherry, J. A. Sirenson, and M. E. Phelps, *Physics in Nuclear Medicine*. Philadelphia: Saunders, 2012.
[22] A. E. Ferretti, N. D. Mercaldo, and M. M. Rehani, 'Estimating the number of ≥100 mSv patients from CT, fluoroscopic guided interventions, and PET exams in 27 OECD countries', *Phys. Med.*, vol. 134, p. 105006, Jun. 2025, doi: 10.1016/j.ejmp.2025.105006.
[23] B. Zangheri, C. Messa, M. Picchio, L. Gianolli, C. Landoni, and F. Fazio, 'PET/CT and breast cancer', *Eur. J. Nucl. Med. Mol. Imaging*, vol. 31, no. 1, pp. S135–S142, Jun. 2004, doi: 10.1007/s00259-004-1536-7.
[24] T. Bunyaviroch and R. E. Coleman, 'PET Evaluation of Lung Cancer', *J. Nucl. Med.*, vol. 47, no. 3, pp. 451–469, Mar. 2006.
[25] I. Edler and C. H. Hertz, 'The Use of Ultrasonic Reflectoscope for the Continuous Recording of the Movements of Heart Walls.', *Clin. Physiol. Funct. Imaging*, vol. 24, no. 3, pp. 118–136, 2004, doi: 10.1111/j.1475-097X.2004.00539.x.
[26] J. J. Wild, 'The use of ultrasonic pulses for the measurement of biologic tissues and the detection of tissue density changes', *Surgery*, vol. 27, no. 2, pp. 183–188, Feb. 1950, doi: 10.5555/uri:pii:0039606050903229.
[27] A. Carovac, F. Smajlovic, and D. Junuzovic, 'Application of ultrasound in medicine', *Acta Inform. Medica AIM J. Soc. Med. Inform. Bosnia Herzeg. Cas. Drustva Za Med. Inform. BiH*, vol. 19, no. 3, pp. 168–171, Sep. 2011, doi: 10.5455/aim.2011.19.168-171.
[28] H. Huang, R. S. Wu, M. Lin, and S. Xu, 'Emerging Wearable Ultrasound Technology', *IEEE Trans. Ultrason. Ferroelectr. Freq. Control*, vol. 71, no. 7, pp. 713–729, Jul. 2024, doi: 10.1109/TUFFC.2023.3327143.
[29] J. Li, Y. Ma, T. Zhang, K. K. Shung, and B. Zhu, 'Recent Advancements in Ultrasound Transducer: From Material Strategies to Biomedical Applications', *BME Front.*, vol. 2022, p. 9764501, doi: 10.34133/2022/9764501.
[30] J. A. Jensen, 'Medical ultrasound imaging', *Prog. Biophys. Mol. Biol.*, vol. 93, no. 1, pp. 153–165, Jan. 2007, doi: 10.1016/j.pbiomolbio.2006.07.025.
[31] R. Guo, G. Lu, B. Qin, and B. Fei, 'Ultrasound Imaging Technologies for Breast Cancer Detection and Management: A Review', *Ultrasound Med. Biol.*, vol. 44, no. 1, pp. 37–70, Jan. 2018, doi: 10.1016/j.ultrasmedbio.2017.09.012.
[32] S. Yagel, S. M. Cohen, I. Shapiro, and D. V. Valsky, '3D and 4D ultrasound in fetal cardiac scanning: a new look at the fetal heart', *Ultrasound Obstet. Gynecol.*, vol. 29, no. 1, pp. 81–95, 2007, doi: 10.1002/uog.3912.
[33] T. R. Nelson and D. H. Pretorius, 'Three-dimensional ultrasound imaging', *Ultrasound Med. Biol.*, vol. 24, no. 9, pp. 1243–1270, Dec. 1998, doi: 10.1016/S0301-5629(98)00043-X.
[34] S. F. Nagueh *et al.*, 'Recommendations for the Evaluation of Left Ventricular Diastolic Function by Echocardiography: An Update from the American Society of Echocardiography and the European Association of Cardiovascular Imaging', *Eur. Heart J. - Cardiovasc. Imaging*, vol. 17, no. 12, pp. 1321–1360, Dec. 2016, doi: 10.1093/ehjci/jew082.
[35] T. Lloyd, Y.-M. Tang, M. D. Benson, and S. King, 'Diaphragmatic paralysis: the use of M mode ultrasound for diagnosis in adults', *Spinal Cord*, vol. 44, no. 8, pp. 505–508, Aug. 2006, doi: 10.1038/sj.sc.3101889.

[36] B. Saugel, T. W. L. Scheeren, and J.-L. Teboul, 'Ultrasound-guided central venous catheter placement: a structured review and recommendations for clinical practice', *Crit. Care*, vol. 21, no. 1, p. 225, Aug. 2017, doi: 10.1186/s13054-017-1814-y.
[37] R. McPhillips, 'Fabrication of Ultrasound Transducers and Arrays Integrated within Needles for Imaging Guidance and Diagnosis', University of Dundee, 2017.
[38] J. Hong *et al.*, 'A Dual-Mode Imaging Catheter for Intravascular Ultrasound Application', *IEEE Trans. Med. Imaging*, vol. 38, no. 3, pp. 657–663, Mar. 2019, doi: 10.1109/TMI.2018.2869942.
[39] T. Shiina *et al.*, 'WFUMB guidelines and recommendations for clinical use of ultrasound elastography: Part 1: basic principles and terminology', *Ultrasound Med. Biol.*, vol. 41, no. 5, pp. 1126–1147, May 2015, doi: 10.1016/j.ultrasmedbio.2015.03.009.
[40] R. M. S. Sigrist, J. Liau, A. E. Kaffas, M. C. Chammas, and J. K. Willmann, 'Ultrasound Elastography: Review of Techniques and Clinical Applications', *Theranostics*, vol. 7, no. 5, pp. 1303–1329, 2017, doi: 10.7150/thno.18650.
[41] D. A. Termure *et al.*, 'Shear Wave Elastography for Distinguishing Cervical Lymph Node Malignancy: A Prospective, Observational Study', *Biomedicines*, vol. 13, no. 8, p. 2001, Aug. 2025, doi: 10.3390/biomedicines13082001.
[42] D. Huang *et al.*, 'Optical Coherence Tomography', *Science*, vol. 254, no. 5035, pp. 1178–1181, Nov. 1991, doi: 10.1126/science.1957169.
[43] J. G. Fujimoto and J. M. Schmitt, 'Principles of OCT', in *Optical Coherence Tomography in Cardiovascular Research*, CRC Press, 2007.
[44] J. Yin *et al.*, 'Integrated intravascular optical coherence tomography ultrasound imaging system', *J. Biomed. Opt.*, vol. 15, no. 1, p. 010512, Jan. 2010, doi: 10.1117/1.3308642.
[45] M. Kawasaki *et al.*, 'Diagnostic Accuracy of Optical Coherence Tomography and Integrated Backscatter Intravascular Ultrasound Images for Tissue Characterization of Human Coronary Plaques', *JACC*, vol. 48, no. 1, pp. 81–88, Jul. 2006, doi: 10.1016/j.jacc.2006.02.062.
[46] J. Kim *et al.*, 'Enhanced dual-mode imaging: Superior photoacoustic and ultrasound endoscopy in live pigs using a transparent ultrasound transducer', *Sci. Adv.*, vol. 10, no. 47, p. eadq9960, Nov. 2024, doi: 10.1126/sciadv.adq9960.
[47] S. Cho *et al.*, 'An ultrasensitive and broadband transparent ultrasound transducer for ultrasound and photoacoustic imaging in-vivo', *Nat. Commun.*, vol. 15, no. 1, p. 1444, Feb. 2024, doi: 10.1038/s41467-024-45273-4.
[48] L. V. Wang and S. Hu, 'Photoacoustic Tomography: In Vivo Imaging from Organelles to Organs', *Science*, vol. 335, no. 6075, pp. 1458–1462, Mar. 2012, doi: 10.1126/science.1216210.
[49] E. B. Dew, A. Kashani Ilkhechi, M. Maadi, N. J. M. Haven, and R. J. Zemp, 'Outperforming piezoelectric ultrasonics with high-reliability single-membrane CMUT array elements', *Microsyst. Nanoeng.*, vol. 8, no. 1, p. 59, Jun. 2022, doi: 10.1038/s41378-022-00392-0.
[50] J. Wang, Z. Zheng, J. Chan, and J. T. W. Yeow, 'Capacitive micromachined ultrasound transducers for intravascular ultrasound imaging', *Microsyst. Nanoeng.*, vol. 6, no. 1, p. 73, Aug. 2020, doi: 10.1038/s41378-020-0181-z.
[51] S. Wu *et al.*, 'Aluminum Nitride Piezoelectric Micromachined Ultrasound Transducer Arrays for Non-Invasive Monitoring of Radial Artery Stiffness', *Micromachines*, vol. 14, no. 3, Feb. 2023, doi: 10.3390/mi14030539.
[52] A. Logan and J. T. W. Yeow, 'Fabricating capacitive micromachined ultrasonic transducers with a novel silicon-nitride-Based wafer bonding process', *IEEE*

Trans. Ultrason. Ferroelectr. Freq. Control, vol. 56, no. 5, pp. 1074–1084, May 2009, doi: 10.1109/TUFFC.2009.1141.

[53] J. Chan, Z. Zheng, K. Bell, M. Le, P. H. Reza, and J. T. W. Yeow, 'Photoacoustic Imaging with Capacitive Micromachined Ultrasound Transducers: Principles and Developments', *Sensors*, vol. 19, no. 16, p. 3617, Jan. 2019, doi: 10.3390/s19163617.

[54] B. T. Khuri-Yakub and Ö. Oralkan, 'Capacitive micromachined ultrasonic transducers for medical imaging and therapy', *J. Micromechanics Microengineering*, vol. 21, no. 5, p. 054004, Apr. 2011, doi: 10.1088/0960-1317/21/5/054004.

[55] G. S. Kino, *Acoustic waves: devices, imaging, and analog signal processing*. in Prentice Hall signal processing series. Prentice-Hall, 1987. Accessed: Jan. 13, 2026. [Online]. Available: https://cir.nii.ac.jp/crid/1971430859792932129

[56] L. E. Kinsler, A. R. Frey, A. B. Coppens, and J. V. Sanders, *Fundamentals of Acoustics*. New York: Wiley, 2000.

[57] J. Zhou, J. Bai, and Y. Liu, 'Fabrication and Modeling of Matching System for Air-Coupled Transducer', *Micromachines*, vol. 13, no. 5, p. 781, May 2022, doi: 10.3390/mi13050781.

[58] S. T. Lau *et al.*, 'Multiple matching scheme for broadband 0.72Pb(Mg1⁄3Nb2⁄3)O3−0.28PbTiO3 single crystal phased-array transducer', *J. Appl. Phys.*, vol. 105, no. 9, p. 094908, May 2009, doi: 10.1063/1.3065476.

[59] T. R. Meeker, 'Publication and proposed revision of ANSI/IEEE standard 176-1987 ANSI/IEEE Standard on piezoelectricity', *IEEE Trans. Ultrason. Ferroelectr. Freq. Control*, vol. 43, no. 5, pp. 717–772, 1996.

[60] Z. Zhang *et al.*, 'High-Performance Ultrasound Needle Transducer Based on Modified PMN-PT Ceramic With Ultrahigh Clamped Dielectric Permittivity', *IEEE Trans. Ultrason. Ferroelectr. Freq. Control*, vol. 65, no. 2, pp. 223–230, Feb. 2018, doi: 10.1109/TUFFC.2017.2778738.

[61] J. W. Hunt, M. Arditi, and F. S. Foster, 'Ultrasound transducers for pulse-echo medical imaging', *IEEE Trans. Biomed. Eng.*, vol. 30, no. 8, pp. 453–481, Aug. 1983, doi: 10.1109/tbme.1983.325150.

[62] Q. Zhou, K. H. Lam, H. Zheng, W. Qiu, and K. K. Shung, 'Piezoelectric single crystal ultrasonic transducers for biomedical applications', *Prog. Mater. Sci.*, vol. 66, pp. 87–111, Oct. 2014, doi: 10.1016/j.pmatsci.2014.06.001.

[63] G. H. Haertling, 'Ferroelectric Ceramics: History and Technology', *J. Am. Ceram. Soc.*, vol. 82, no. 4, pp. 797–818, 1999, doi: 10.1111/j.1151-2916.1999.tb01840.x.

[64] S.-E. Park and T. R. Shrout, 'Ultrahigh strain and piezoelectric behavior in relaxor based ferroelectric single crystals', *J. Appl. Phys.*, vol. 82, no. 4, pp. 1804–1811, Aug. 1997, doi: 10.1063/1.365983.

[65] W. Zhang *et al.*, 'Determination of the Mechanical Properties of PIN–PMN–PT Bulk Single Crystals by Nanoindentation', *Crystals*, vol. 10, no. 1, Art. no. 1, Jan. 2020, doi: 10.3390/cryst10010028.

[66] F. S. Foster, K. A. Harasiewicz, and M. D. Sherar, 'A history of medical and biological imaging with polyvinylidene fluoride (PVDF) transducers', *IEEE Trans. Ultrason. Ferroelectr. Freq. Control*, vol. 47, no. 6, pp. 1363–1371, 2000, doi: 10.1109/58.883525.

[67] P. C. Beard, A. M. Hurrell, and T. N. Mills, 'Characterization of a polymer film optical fiber hydrophone for use in the range 1 to 20 MHz: A comparison with PVDF needle and membrane hydrophones', *IEEE Trans. Ultrason. Ferroelectr. Freq. Control*, vol. 47, no. 1, pp. 256–264, Jan. 2000, doi: 10.1109/58.818769.

[68] V. Wilkens and W. Molkenstruck, 'Broadband PVDF Membrane Hydrophone for Comparisons of Hydrophone Calibration Methods up to 140 MHz', *IEEE Trans.*

Ultrason. Ferroelectr. Freq. Control, vol. 54, no. 9, pp. 1784–1791, Sep. 2007, doi: 10.1109/TUFFC.2007.462.
[69] G. Pittiglio *et al.*, 'Personalized magnetic tentacles for targeted photothermal cancer therapy in peripheral lungs', *Commun. Eng.*, vol. 2, no. 1, pp. 1–13, Jul. 2023, doi: 10.1038/s44172-023-00098-9.
[70] E. M. Sabolsky, A. R. James, S. Kwon, S. Trolier-McKinstry, and G. L. Messing, 'Piezoelectric properties of ⟨001⟩ textured Pb(Mg1/3Nb2/3)O3–PbTiO3 ceramics', *Appl. Phys. Lett.*, vol. 78, no. 17, pp. 2551–2553, Apr. 2001, doi: 10.1063/1.1367291.
[71] W. A. Smith and B. A. Auld, 'Modeling 1-3 composite piezoelectrics: thickness-mode oscillations', *IEEE Trans. Ultrason. Ferroelectr. Freq. Control*, vol. 38, no. 1, pp. 40–47, Jan. 1991, doi: 10.1109/58.67833.
[72] X. Li, L. Wang, C. Zhong, and Y. Zhang, 'The effect of piezoelectric ceramic volume fraction on the thickness vibration characteristics of 1-3 piezocomposites', *Ferroelectrics*, vol. 531, no. 1, pp. 84–91, Jul. 2018, doi: 10.1080/00150193.2018.1497420.
[73] P. Sun *et al.*, 'High Frequency PMN-PT 1-3 Composite Transducer for Ultrasonic Imaging Application', *Ferroelectrics*, vol. 408, no. 1, pp. 120–128, Nov. 2010, doi: 10.1080/00150193.2010.485546.
[74] Z.-Y. Shen, J.-F. Li, R. Chen, Q. Zhou, and K. K. Shung, 'Microscale 1–3-Type (Na,K)NbO3-Based Pb-Free Piezocomposites for High-Frequency Ultrasonic Transducer Applications', *J. Am. Ceram. Soc. Am. Ceram. Soc.*, vol. 94, no. 5, pp. 1346–1349, May 2011, doi: 10.1111/j.1551-2916.2011.04508.x.
[75] J.-M. Zhang, G.-C. Bao, W. Gao, R.-Q. Lin, F. Yang, and K.-H. Lam, 'Miniature Ultrasound Transducer Incorporating Sm-PMN-PT 1-3 Composite', *J. Compos. Sci.*, vol. 8, no. 3, p. 80, Feb. 2024, doi: 10.3390/jcs8030080.
[76] G. Hayward and J. A. Hossack, 'Unidimensional modeling of 1-3 composite transducers', *J. Acoust. Soc. Am.*, vol. 88, no. 2, pp. 599–608, Aug. 1990, doi: 10.1121/1.399763.
[77] A. Abrar, D. Zhang, B. Su, T. W. Button, K. J. Kirk, and S. Cochran, '1–3 connectivity piezoelectric ceramic–polymer composite transducers made with viscous polymer processing for high frequency ultrasound', *Ultrasonics*, vol. 42, no. 1, pp. 479–484, Apr. 2004, doi: 10.1016/j.ultras.2004.02.008.
[78] W. Wang, S. Wang, Y. Zhang, X. Zhao, and H. Luo, 'Beam-Mode Piezoelectric Properties of TernaryPb(In1/2Nb1/2)O3-Pb(Mg1/3Nb2/3)O3-PbTiO3 Single Crystalsfor Medical Linear Array Applications', *J. Electron. Mater.*, vol. 40, no. 11, pp. 2228–2233, Nov. 2011, doi: 10.1007/s11664-011-1724-8.
[79] Q. Yue *et al.*, 'Design and fabrication of relaxor-ferroelectric single crystal PIN–PMN–PT/epoxy 2–2 composite based array transducer', *Sens. Actuators Phys.*, vol. 234, pp. 34–42, Oct. 2015, doi: 10.1016/j.sna.2015.08.017.
[80] W. Wang *et al.*, 'Ternary piezoelectric single-crystal PIMNT based 2-2 composite for ultrasonic transducer applications', *Sens. Actuators Phys.*, vol. 196, pp. 70–77, Jul. 2013, doi: 10.1016/j.sna.2013.03.014.
[81] Y. Qiu *et al.*, 'Ultrasound Capsule Endoscopy With a Mechanically Scanning Micro-ultrasound: A Porcine Study', *Ultrasound Med. Biol.*, vol. 46, no. 3, pp. 796–804, Mar. 2020, doi: 10.1016/j.ultrasmedbio.2019.12.003.
[82] C. J. Pavlin and F. S. Foster, 'Ultrasound biomicroscopy. High-frequency ultrasound imaging of the eye at microscopic resolution', *Radiol. Clin. North Am.*, vol. 36, no. 6, pp. 1047–1058, Nov. 1998, doi: 10.1016/s0033-8389(05)70230-x.
[83] N. G. Pandian, A. Weintraub, A. Kreis, S. L. Schwartz, M. A. Konstam, and D. N. Salem, 'Intracardiac, intravascular, two-dimensional, high-frequency ultrasound imaging of pulmonary artery and its branches in humans and animals',

Circulation, vol. 81, no. 6, pp. 2007–2012, Jun. 1990, doi: 10.1161/01.cir.81.6.2007.
[84] F. S. Foster, C. J. Pavlin, K. A. Harasiewicz, D. A. Christopher, and D. H. Turnbull, 'Advances in ultrasound biomicroscopy', *Ultrasound Med. Biol.*, vol. 26, no. 1, pp. 1–27, Jan. 2000, doi: 10.1016/S0301-5629(99)00096-4.
[85] Haifeng Wang, T. Ritter, Wenwu Cao, and K. K. Shung, 'High frequency properties of passive materials for ultrasonic transducers', *IEEE Trans. Ultrason. Ferroelectr. Freq. Control*, vol. 48, no. 1, pp. 78–84, Jan. 2001, doi: 10.1109/58.895911.
[86] G. S. Mintz *et al.*, 'American College of Cardiology Clinical Expert Consensus Document on Standards for Acquisition, Measurement and Reporting of Intravascular Ultrasound Studies (IVUS). A report of the American College of Cardiology Task Force on Clinical Expert Consensus Documents', *J. Am. Coll. Cardiol.*, vol. 37, no. 5, pp. 1478–1492, Apr. 2001, doi: 10.1016/s0735-1097(01)01175-5.
[87] M. Araki *et al.*, 'Optical coherence tomography in coronary atherosclerosis assessment and intervention', *Nat. Rev. Cardiol.*, vol. 19, no. 10, pp. 684–703, Oct. 2022, doi: 10.1038/s41569-022-00687-9.
[88] C. Peng, H. Wu, S. Kim, X. Dai, and X. Jiang, 'Recent Advances in Transducers for Intravascular Ultrasound (IVUS) Imaging', *Sensors*, vol. 21, no. 10, p. 3540, Jan. 2021, doi: 10.3390/s21103540.
[89] J. Li *et al.*, 'Ultrafast optical-ultrasonic system and miniaturized catheter for imaging and characterizing atherosclerotic plaques in vivo', *Sci. Rep.*, vol. 5, no. 1, p. 18406, Dec. 2015, doi: 10.1038/srep18406.
[90] X. Liu, Y. Li, H. Qin, and C. Peng, 'High-Frequency 64-Element Ring-Annular Array Transducer: Development and Preclinical Validation for Intravascular Ultrasound Imaging', *Biosensors*, vol. 15, no. 3, p. 169, Mar. 2025, doi: 10.3390/bios15030169.
[91] C. V. Bourantas *et al.*, 'Hybrid intravascular imaging: recent advances, technical considerations, and current applications in the study of plaque pathophysiology', *Eur. Heart J.*, vol. 38, no. 6, pp. 400–412, Feb. 2017, doi: 10.1093/eurheartj/ehw097.
[92] H. Pan *et al.*, 'Ultrathin endoscope equipped with ultrasonic miniprobe for upper GI US in a porcine model', *Gastrointest. Endosc.*, vol. 99, no. 1, pp. 108-115.e1, Jan. 2024, doi: 10.1016/j.gie.2023.09.009.
[93] Q. Tan *et al.*, 'Ultrafast Endoscopic Ultrasonography With Circular Array', *IEEE Trans. Med. Imaging*, vol. 39, no. 6, pp. 2110–2120, Jun. 2020, doi: 10.1109/TMI.2019.2963290.
[94] N. Wang *et al.*, 'High-Frequency Endoscopic Ultrasound Imaging With Phase-Corrected-and-Sum and Coherence Factor Weighting', *IEEE Trans. Ultrason. Ferroelectr. Freq. Control*, vol. 69, no. 6, pp. 1881–1888, Jun. 2022, doi: 10.1109/TUFFC.2022.3142250.
[95] Q. Zhang *et al.*, '1.5-Dimensional Circular Array Transducer for In Vivo Endoscopic Ultrasonography', *IEEE Trans. Biomed. Eng.*, vol. 68, no. 10, pp. 2930–2939, Oct. 2021, doi: 10.1109/TBME.2021.3056140.
[96] H. Matsubayashi *et al.*, 'Endoscopic ultrasonography guided-fine needle aspiration for the diagnosis of solid pancreaticobiliary lesions: Clinical aspects to improve the diagnosis', *World J. Gastroenterol.*, vol. 22, no. 2, pp. 628–640, Jan. 2016, doi: 10.3748/wjg.v22.i2.628.
[97] H. K. Chiang *et al.*, 'Eyes in the Needle: Novel Epidural Needle with Embedded High-frequency Ultrasound Transducer—Epidural Access in Porcine Model',

Anesthesiology, vol. 114, no. 6, p. 1320, Jun. 2011, doi: 10.1097/ALN.0b013e31821b5746.
[98] H. K. Zhang *et al.*, 'Toward dynamic lumbar puncture guidance using needle-based single-element ultrasound imaging', *J. Med. Imaging*, vol. 5, no. 2, p. 021224, Apr. 2018, doi: 10.1117/1.JMI.5.2.021224.
[99] Q. Zhou *et al.*, 'Design and fabrication of PZN-7%PT single crystal high frequency angled needle ultrasound transducers', *IEEE Trans. Ultrason. Ferroelectr. Freq. Control*, vol. 55, no. 6, pp. 1394–1399, 2008, doi: 10.1109/TUFFC.2008.804.
[100] B. C. Kreager *et al.*, 'High-Performance PMN-PT Single-Crystal-Based 1-3 Composite Transducer Integrated with a Biopsy Needle', *Biosensors*, vol. 14, no. 2, p. 74, Jan. 2024, doi: 10.3390/bios14020074.
[101] X. Wang *et al.*, 'Stepped 2D array needle transducer for 4D ultrasound imaging-guided spinal puncture', *The Innovation*, vol. 7, no. 1, p. 101075, Jan. 2026, doi: 10.1016/j.xinn.2025.101075.
[102] X. Wang *et al.*, 'Development of a Mechanical Scanning Device With High-Frequency Ultrasound Transducer for Ultrasonic Capsule Endoscopy', *IEEE Trans. Med. Imaging*, vol. 36, no. 9, pp. 1922–1929, Sep. 2017, doi: 10.1109/TMI.2017.2699973.
[103] X.-O. Qiu *et al.*, 'New US capsule endoscopy for superficial and submucosal imaging of the esophagus: the first-in-human study', *Gastrointest. Endosc.*, vol. 98, no. 4, pp. 642–652, Oct. 2023, doi: 10.1016/j.gie.2023.06.015.
[104] Y.-Z. Chen *et al.*, 'Novel ultrasound capsule endoscopy for gastrointestinal scanning: An in vivo animal study', *Endosc. Ultrasound*, vol. 13, no. 4, pp. 253–258, 2024, doi: 10.1097/eus.0000000000000078.
[105] H. S. Lay, B. F. Cox, V. Seetohul, C. E. M. Démoré, and S. Cochran, 'Design and Simulation of a Ring-Shaped Linear Array for Microultrasound Capsule Endoscopy', *IEEE Trans. Ultrason. Ferroelectr. Freq. Control*, vol. 65, no. 4, pp. 589–599, Apr. 2018, doi: 10.1109/TUFFC.2018.2794220.
[106] N. J. Greenidge *et al.*, 'Harnessing the oloid shape in magnetically driven robots to enable high-resolution ultrasound imaging', *Sci. Robot.*, vol. 10, no. 100, p. eadq4198, Mar. 2025, doi: 10.1126/scirobotics.adq4198.
[107] P. E. Dupont *et al.*, 'A decade retrospective of medical robotics research from 2010 to 2020', *Sci. Robot.*, vol. 6, no. 60, p. eabi8017, Nov. 2021, doi: 10.1126/scirobotics.abi8017.
[108] J. Guo, S. Guo, and Y. Yu, 'Design and characteristics evaluation of a novel teleoperated robotic catheterization system with force feedback for vascular interventional surgery', *Biomed. Microdevices*, vol. 18, no. 5, p. 76, Oct. 2016, doi: 10.1007/s10544-016-0100-0.
[109] C. C. Nguyen *et al.*, 'Development of a soft robotic catheter for vascular intervention surgery', *Sens. Actuators Phys.*, vol. 357, p. 114380, Aug. 2023, doi: 10.1016/j.sna.2023.114380.
[110] C. C. Nguyen *et al.*, 'A Handheld Hydraulic Soft Robotic Device With Bidirectional Bending End-Effector for Minimally Invasive Surgery', *IEEE Trans. Med. Robot. Bionics*, vol. 5, no. 3, pp. 590–601, Aug. 2023, doi: 10.1109/TMRB.2023.3291014.
[111]T. Gopesh *et al.*, 'Soft robotic steerable microcatheter for the endovascular treatment of cerebral disorders', *Sci. Robot.*, vol. 6, no. 57, p. eabf0601, Aug. 2021, doi: 10.1126/scirobotics.abf0601.
[112] L. Mao *et al.*, 'Magnetic steering continuum robot for transluminal procedures with programmable shape and functionalities', *Nat. Commun.*, vol. 15, no. 1, p. 3759, May 2024, doi: 10.1038/s41467-024-48058-x.

[113] G. Pittiglio *et al.*, 'Patient-Specific Magnetic Catheters for Atraumatic Autonomous Endoscopy', *Soft Robot.*, vol. 9, no. 6, pp. 1120–1133, Dec. 2022, doi: 10.1089/soro.2021.0090.
[114] Y. Cao *et al.*, 'Magnetic Continuum Robot with Intraoperative Magnetic Moment Programming', *Soft Robot.*, vol. 10, no. 6, pp. 1209–1223, Dec. 2023, doi: 10.1089/soro.2022.0202.
[115] Y. Piskarev *et al.*, 'A Variable Stiffness Magnetic Catheter Made of a Conductive Phase-Change Polymer for Minimally Invasive Surgery', *Adv. Funct. Mater.*, vol. 32, no. 20, p. 2107662, 2022, doi: 10.1002/adfm.202107662.
[116] C. Fischer, Q. Boehler, and B. J. Nelson, 'Using Magnetic Fields to Navigate and Simultaneously Localize Catheters in Endoluminal Environments', *IEEE Robot. Autom. Lett.*, vol. 7, no. 3, pp. 7217–7223, Jul. 2022, doi: 10.1109/LRA.2022.3181420.
[117] P. Lloyd *et al.*, 'A Magnetically-Actuated Coiling Soft Robot With Variable Stiffness', *IEEE Robot. Autom. Lett.*, vol. 8, no. 6, pp. 3262–3269, Jun. 2023, doi: 10.1109/LRA.2023.3264770.
[118] G. Pittiglio *et al.*, 'Closed Loop Static Control of Multi-Magnet Soft Continuum Robots', *IEEE Robot. Autom. Lett.*, vol. 8, no. 7, pp. 3980–3987, Jul. 2023, doi: 10.1109/LRA.2023.3274431.
[119] R. Krimholtz, D. A. Leedom, and G. L. Matthaei, 'New equivalent circuits for elementary piezoelectric transducers', *Electron. Lett.*, vol. 6, no. 13, pp. 398–399, Jun. 1970, doi: 10.1049/el:19700280.
[120] A. Trogé, R. L. O'Leary, G. Hayward, R. A. Pethrick, and A. J. Mullholland, 'Properties of photocured epoxy resin materials for application in piezoelectric ultrasonic transducer matching layers', *J. Acoust. Soc. Am.*, vol. 128, no. 5, pp. 2704–2714, Nov. 2010, doi: 10.1121/1.3483734.
[121] J. M. Cannata, T. A. Ritter, W.-H. Chen, R. H. Silverman, and K. K. Shung, 'Design of efficient, broadband single-element (20-80 MHz) ultrasonic transducers for medical imaging applications', *IEEE Trans. Ultrason. Ferroelectr. Freq. Control*, vol. 50, no. 11, pp. 1548–1557, Nov. 2003, doi: 10.1109/TUFFC.2003.1251138.
[122] C.-M. Wong *et al.*, 'Tunable high acoustic impedance alumina epoxy composite matching for high frequency ultrasound transducer', *Ultrasonics*, vol. 116, p. 106506, Sep. 2021, doi: 10.1016/j.ultras.2021.106506.
[123] A. C. Moldovan, 'Development of a 1D phased ultrasonic array for intravascular sonoporation', University of Strathclyde, 2020. doi: 10.48730/2a6m-5e81.
[124] M. Todeschini, A. Bastos da Silva Fanta, F. Jensen, J. B. Wagner, and A. Han, 'Influence of Ti and Cr Adhesion Layers on Ultrathin Au Films', *ACS Appl. Mater. Interfaces*, vol. 9, no. 42, pp. 37374–37385, Oct. 2017, doi: 10.1021/acsami.7b10136.
[125] Q. Ke, W. H. Liew, H. Tao, J. Wu, and K. Yao, 'KNNS-BNZH Lead-Free 1–3 Piezoelectric Composite for Ultrasonic and Photoacoustic Imaging', *IEEE Trans. Ultrason. Ferroelectr. Freq. Control*, vol. 66, no. 8, pp. 1395–1401, Aug. 2019, doi: 10.1109/TUFFC.2019.2914464.
[126] L. Jiang *et al.*, 'Fabrication of a (K,Na)NbO3-based lead-free 1-3 piezocomposite for high-sensitivity ultrasonic transducers application', *J. Appl. Phys.*, vol. 125, no. 21, p. 214501, Jun. 2019, doi: 10.1063/1.5088171.
[127] S. Zhang and F. Li, 'High performance ferroelectric relaxor-PbTiO3 single crystals: Status and perspective', *J. Appl. Phys.*, vol. 111, no. 3, p. 031301, Feb. 2012, doi: 10.1063/1.3679521.

[128] X. Jian *et al.*, ‘Development of Self-Focusing Piezoelectric Composite Ultrasound Transducer Using Laser Engraving Technology’, *IEEE Trans. Ultrason. Ferroelectr. Freq. Control*, vol. 66, no. 12, pp. 1866–1873, Dec. 2019, doi: 10.1109/TUFFC.2019.2935215.
[129] Q. Zhang *et al.*, ‘Miniature Transducer Using PNN-PZT-Based Ceramic for Intravascular Ultrasound’, *IEEE Trans. Ultrason. Ferroelectr. Freq. Control*, vol. 66, no. 6, pp. 1102–1109, Jun. 2019, doi: 10.1109/TUFFC.2019.2906652.
[130] J. Wang *et al.*, ‘Fabrication and properties of the thickness mode ultrasonic transducer based on 0.15Pb(Mg1/3Nb2/3)O3-0.38PbHfO3-0.47PbTiO3 piezoelectric ceramics’, *Ceram. Int.*, vol. 46, no. 8, Part B, pp. 11913–11920, Jun. 2020, doi: 10.1016/j.ceramint.2020.01.228.
[131] M. Golda-Cepa, K. Engvall, M. Hakkarainen, and A. Kotarba, ‘Recent progress on parylene C polymer for biomedical applications: A review’, *Prog. Org. Coat.*, vol. 140, p. 105493, Mar. 2020, doi: 10.1016/j.porgcoat.2019.105493.
[132] C.-M. Wong, Y. Chen, H. Luo, J. Dai, K.-H. Lam, and H. L. Chan, ‘Development of a 20-MHz wide-bandwidth PMN-PT single crystal phased-array ultrasound transducer’, *Ultrasonics*, vol. 73, pp. 181–186, Jan. 2017, doi: 10.1016/j.ultras.2016.09.012.
[133] X. Li, T. Ma, J. Tian, P. Han, Q. Zhou, and K. K. Shung, ‘Micromachined PIN-PMN-PT crystal composite transducer for high-frequency intravascular ultrasound (IVUS) imaging’, *IEEE Trans. Ultrason. Ferroelectr. Freq. Control*, vol. 61, no. 7, pp. 1171–1178, Jul. 2014, doi: 10.1109/TUFFC.2014.3016.
[134] Z. Wang, B. P. Yalagala, H. Heidari, and A. Feeney, ‘Highly Sensitive Parylene C-Based Flexible Pressure Sensors for Wearable Systems’, *Small Sci.*, vol. 5, no. 7, p. 2500081, 2025, doi: 10.1002/smsc.202500081.
[135] J. A. Brown, F. S. Foster, A. Needles, E. Cherin, and G. R. Lockwood, ‘Fabrication and Performance of a 40-MHz Linear Array Based on a 1-3 Composite with Geometric Elevation Focusing’, *IEEE Trans. Ultrason. Ferroelectr. Freq. Control*, vol. 54, no. 9, pp. 1888–1894, Sep. 2007, doi: 10.1109/TUFFC.2007.473.
[136] J. A. Brown, C. E. M. Demore, and G. R. Lockwood, ‘Design and fabrication of annular arrays for high-frequency ultrasound’, *IEEE Trans. Ultrason. Ferroelectr. Freq. Control*, vol. 51, no. 8, pp. 1010–1017, Aug. 2004, doi: 10.1109/TUFFC.2004.1324405.
[137] T. A. Ritter, T. R. Shrout, R. Tutwiler, and K. K. Shung, ‘A 30-MHz piezo-composite ultrasound array for medical imaging applications’, *IEEE Trans. Ultrason. Ferroelectr. Freq. Control*, vol. 49, no. 2, pp. 217–230, Feb. 2002, doi: 10.1109/58.985706.
[138] J. Janjic, M. Shabanimotlagh, G. Van Soest, A. F. W. Van Der Steen, N. De Jong, and M. D. Verweij, ‘Improving the Performance of a 1-D Ultrasound Transducer Array by Subdicing’, *IEEE Trans. Ultrason. Ferroelectr. Freq. Control*, vol. 63, no. 8, pp. 1161–1171, Aug. 2016, doi: 10.1109/TUFFC.2016.2561935.
[139] C. Qiu *et al.*, ‘Transparent ultrasonic transducers based on relaxor ferroelectric crystals for advanced photoacoustic imaging’, *Nat. Commun.*, vol. 15, no. 1, p. 10580, Dec. 2024, doi: 10.1038/s41467-024-55032-0.
[140] B. Calmé *et al.*, ‘Hybrid Tendon-Actuated and Soft Magnetic Robotic Platform for Pancreatic Applications’, *IEEE Robot. Autom. Lett.*, vol. 10, no. 2, pp. 1784–1791, Feb. 2025, doi: 10.1109/LRA.2024.3524889.
[141] D. Y. Wang, K. Li, and H. L. W. Chan, ‘High frequency 1-3 composite transducer fabricated using sol–gel derived lead-free BNBT fibers’, *Sens.*

Actuators Phys., vol. 114, no. 1, pp. 1–6, Aug. 2004, doi: 10.1016/j.sna.2004.02.024.
[142] T. Zheng *et al.*, 'High-performance potassium sodium niobate piezoceramics for ultrasonic transducer', *Nano Energy*, vol. 70, p. 104559, Apr. 2020, doi: 10.1016/j.nanoen.2020.104559.
[143] V. Francescon, N. Murasovs, P. Lloyd, O. Onaizah, D. S. Chathuranga, and P. Valdastri, 'Closed-Loop Shape-Forming Control of a Magnetic Soft Continuum Robot', *IEEE Robot. Autom. Lett.*, vol. 10, no. 6, pp. 6071–6078, Jun. 2025, doi: 10.1109/LRA.2025.3565124.
[144] S. Zhou *et al.*, 'Transcranial volumetric imaging using a conformal ultrasound patch', *Nature*, vol. 629, no. 8013, pp. 810–818, May 2024, doi: 10.1038/s41586-024-07381-5.
[145] B. Liu *et al.*, 'A Novel Dual-Element Catheter for Improving Non-Uniform Rotational Distortion in Intravascular Ultrasound', *IEEE Trans. Biomed. Eng.*, vol. 70, no. 6, pp. 1768–1774, Jun. 2023, doi: 10.1109/TBME.2022.3226955.
[146] N. P. du Sert *et al.*, 'Reporting animal research: Explanation and elaboration for the ARRIVE guidelines 2.0', *PLOS Biol.*, vol. 18, no. 7, p. e3000411, Jul. 2020, doi: 10.1371/journal.pbio.3000411.
[147] Z. Zhang *et al.*, 'New Sm-PMN-PT Ceramic-Based 2-D Array for Low-Intensity Ultrasound Therapy Application', *IEEE Trans. Ultrason. Ferroelectr. Freq. Control*, vol. 67, no. 10, pp. 2085–2094, Oct. 2020, doi: 10.1109/TUFFC.2020.2979471.
[148] K. K. Shung, 'High Frequency Ultrasonic Imaging', *J. Med. Ultrasound*, vol. 17, no. 1, pp. 25–30, Jan. 2009, doi: 10.1016/S0929-6441(09)60012-6.
[149] Q. Zhang *et al.*, 'Transformable Ultrasonic Array Transducer for Multiscale Imaging and Beamforming', *IEEE Trans. Ind. Electron.*, vol. 69, no. 3, pp. 3078–3087, Mar. 2022, doi: 10.1109/TIE.2021.3065592.
[150] A. C. Luchies and B. C. Byram, 'Deep Neural Networks for Ultrasound Beamforming', *IEEE Trans. Med. Imaging*, vol. 37, no. 9, pp. 2010–2021, Sep. 2018, doi: 10.1109/TMI.2018.2809641.
[151] E. Germano *et al.*, 'Application of Golay-based total focusing method using a high-frequency, lead-free, flexible ultrasonic array for inspection of thick non-planar industrial components', *NDT E Int.*, vol. 150, p. 103282, Mar. 2025, doi: 10.1016/j.ndteint.2024.103282.
[152] X. Huang, M. A. Lediju Bell, and K. Ding, 'Deep Learning for Ultrasound Beamforming in Flexible Array Transducer', *IEEE Trans. Med. Imaging*, vol. 40, no. 11, pp. 3178–3189, Nov. 2021, doi: 10.1109/TMI.2021.3087450.
[153] Q. Zhou *et al.*, 'PMN-PT single crystal, high-frequency ultrasonic needle transducers for pulsed-wave Doppler application', *IEEE Trans. Ultrason. Ferroelectr. Freq. Control*, vol. 54, no. 3, pp. 668–675, Mar. 2007, doi: 10.1109/tuffc.2007.290.
[154] Y. Chen *et al.*, 'High-frequency PIN–PMN–PT single crystal ultrasonic transducer for imaging applications', *Appl. Phys. A*, vol. 108, no. 4, pp. 987–991, Sep. 2012, doi: 10.1007/s00339-012-7009-0.
[155] J. Luo, H. Marshall, S. Dynan, Y. Sakano, and K. Kitahata, 'Development of Large-Diameter and High-Performance Sm Doped PIN-PMN-PT Crystals for Medical Ultrasound Imaging Transducers', in *2023 IEEE International Ultrasonics Symposium (IUS)*, Montreal, QC, Canada: IEEE, Sep. 2023, pp. 1–4. doi: 10.1109/IUS51837.2023.10306692.
[156] S. Zhang, J. Luo, W. Hackenberger, and T. R. Shrout, 'Characterization of Pb(In1/2Nb1/2)O3–Pb(Mg1/3Nb2/3)O3–PbTiO3 ferroelectric crystal with

enhanced phase transition temperatures', *J. Appl. Phys.*, vol. 104, no. 6, p. 064106, Sep. 2008, doi: 10.1063/1.2978333.
[157] C.-W. Chen *et al.*, 'Depolarization field in relaxor-based ferroelectric single crystals under one-cycle bipolar pulse drive', *Chin. Phys. B*, vol. 28, no. 12, p. 127702, Nov. 2019, doi: 10.1088/1674-1056/ab4e85.
[158] P. Sun *et al.*, 'Design and fabrication of PIN-PMN-PT single-crystal high-frequency ultrasound transducers', *IEEE Trans. Ultrason. Ferroelectr. Freq. Control*, vol. 56, no. 12, pp. 2760–2763, Dec. 2009, doi: 10.1109/TUFFC.2009.1367.
[159] S. Zhang *et al.*, 'Recent developments on high Curie temperature PIN–PMN–PT ferroelectric crystals', *J. Cryst. Growth*, vol. 318, no. 1, pp. 846–850, Mar. 2011, doi: 10.1016/j.jcrysgro.2010.11.043.
[160] Y.-X. Li, X. Yao, X.-S. Wang, and Y.-B. Hao, 'Studies of dielectric properties of rare earth (Dy, Tb, Eu) doped barium titanate sintered in pure nitrogen', *Ceram. Int.*, vol. 38, pp. S29–S32, Jan. 2012, doi: 10.1016/j.ceramint.2011.04.042.
[161] Z. Xi, A. Han, P. Fang, W. Long, X. Li, and Q. Bu, 'Structural and electrical properties of Ho3+-modified Pb(Zn1/3Nb2/3)O3–9PbTiO3 single crystals', *J. Mater. Sci. Mater. Electron.*, vol. 27, no. 5, pp. 4223–4229, May 2016, doi: 10.1007/s10854-016-4286-y.
[162] Y. Chen, D. Zhang, Z. Peng, M. Yuan, and X. Ji, 'Review of Research on the Rare-Earth Doped Piezoelectric Materials', *Front. Mater.*, vol. 8, Jul. 2021, doi: 10.3389/fmats.2021.679167.
[163] F. Li *et al.*, 'Ultrahigh piezoelectricity in ferroelectric ceramics by design', *Nat. Mater.*, vol. 17, no. 4, pp. 349–354, Apr. 2018, doi: 10.1038/s41563-018-0034-4.
[164] Y. Yang, K. Zhu, E. Sun, P. Liu, R. Zhang, and W. Cao, 'Ultrabroad-bandwidth ultrasonic transducer based on Sm-doped PMN-PT ceramic/epoxy 1–3 composite', *Sens. Actuators Phys.*, vol. 346, p. 113873, Oct. 2022, doi: 10.1016/j.sna.2022.113873.
[165] F. Li *et al.*, 'Giant piezoelectricity of Sm-doped Pb(Mg1/3Nb2/3)O3-PbTiO3 single crystals', *Science*, vol. 364, no. 6437, pp. 264–268, Apr. 2019, doi: 10.1126/science.aaw2781.
[166] T. R. Gururaja, W. A. Schulze, L. E. Cross, R. E. Newnham, B. A. Auld, and Y. J. Wang, 'Piezoelectric Composite Materials for Ultrasonic Transducer Applications. Part I: Resonant Modes of Vibration of PZT Rod-Polymer Composites', *IEEE Trans. Sonics Ultrason.*, vol. 32, no. 4, pp. 481–498, Jul. 1985, doi: 10.1109/T-SU.1985.31623.
[167] Z. Li, W. Shao, X. Zhu, J. Lv, Z. Han, and Y. Cui, 'Parylene coating for 13 MHz 1-3 composite transducer performance enhancement', *Appl. Acoust.*, vol. 174, p. 107696, Mar. 2021, doi: 10.1016/j.apacoust.2020.107696.
[168] J. Zhang *et al.*, 'Broadband transparent ultrasound transducer with polymethyl methacrylate as matching layer for *in vivo* photoacoustic microscopy', *Photoacoustics*, vol. 33, p. 100548, Oct. 2023, doi: 10.1016/j.pacs.2023.100548.
[169] S. Zhang, F. Li, X. Jiang, J. Kim, J. Luo, and X. Geng, 'Advantages and challenges of relaxor-PbTiO3 ferroelectric crystals for electroacoustic transducers – A review', *Prog. Mater. Sci.*, vol. 68, pp. 1–66, Mar. 2015, doi: 10.1016/j.pmatsci.2014.10.002.
[170] V. T. Rathod, 'A Review of Acoustic Impedance Matching Techniques for Piezoelectric Sensors and Transducers', *Sensors*, vol. 20, no. 14, Jul. 2020, doi: 10.3390/s20144051.
[171] C. M. Wong *et al.*, '20-MHz phased array ultrasound transducer for *in vivo* ultrasound imaging of small animals', *Ultrasonics*, vol. 126, p. 106821, Dec. 2022, doi: 10.1016/j.ultras.2022.106821.

[172] Z. Zhang *et al.*, ‘Development of a KNN Ceramic-Based Lead-Free Linear Array Ultrasonic Transducer’, *IEEE Trans. Ultrason. Ferroelectr. Freq. Control*, vol. 65, no. 11, pp. 2113–2120, Nov. 2018, doi: 10.1109/TUFFC.2018.2868413.
[173] J. H. Cha and J. H. Chang, ‘Development of 15MHz 2-2 piezo-composite ultrasound linear array transducers for ophthalmic imaging’, *Sens. Actuators Phys.*, vol. 217, pp. 39–48, Sep. 2014, doi: 10.1016/j.sna.2014.06.024.
[174] C.-M. Wong, Y. Chen, H. Luo, J. Dai, K.-H. Lam, and H. L. Chan, ‘Development of a 20-MHz wide-bandwidth PMN-PT single crystal phased-array ultrasound transducer’, *Ultrasonics*, vol. 73, pp. 181–186, Jan. 2017, doi: 10.1016/j.ultras.2016.09.012.
[175] C.-F. Roa *et al.*, ‘Development of a Small-Footprint 50 MHz Linear Array: Fabrication and Micro-Ultrasound Imaging Demonstration’, *Sensors*, vol. 24, no. 6, p. 1847, Mar. 2024, doi: 10.3390/s24061847.
[176] N. E. Cabrera-Munoz *et al.*, ‘Fabrication and Characterization of a Miniaturized 15-MHz Side-Looking Phased-Array Transducer Catheter’, *IEEE Trans. Ultrason. Ferroelectr. Freq. Control*, vol. 66, no. 6, pp. 1079–1092, Jun. 2019, doi: 10.1109/TUFFC.2019.2906134.
[177] H. H. Kim *et al.*, ‘Characterization and evaluation of high frequency convex array transducers’, in *2010 IEEE International Ultrasonics Symposium*, Oct. 2010, pp. 650–653. doi: 10.1109/ULTSYM.2010.5935912.